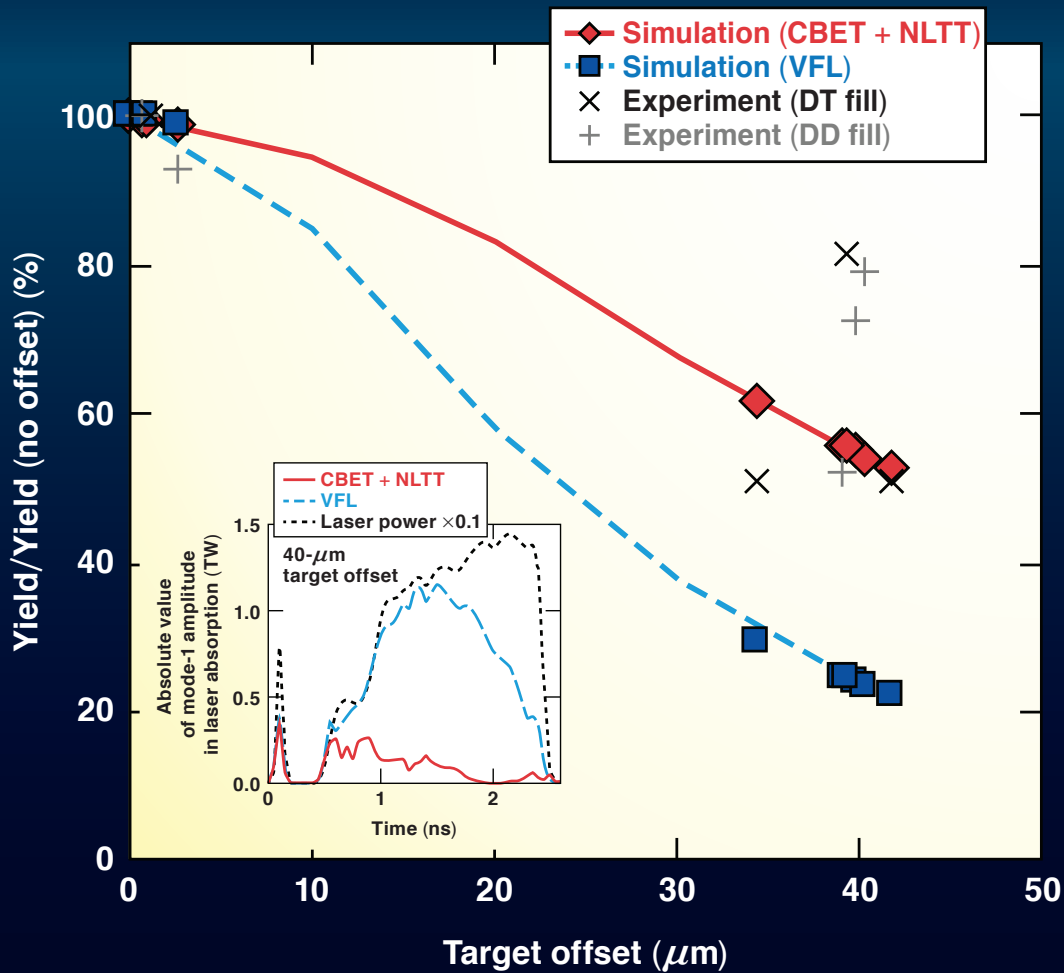


# LLE Review

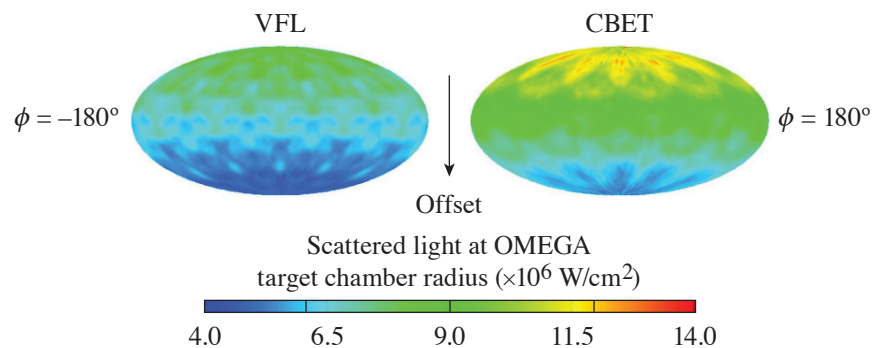
## Quarterly Report



## About the Cover:

Shown on the cover are two plots suggesting cross-beam energy transfer (CBET) as one explanation for why the observed target performance has historically experienced relatively low sensitivity to target offset, in contrast to simulation models. While CBET has been well known to cause significant laser-energy losses to directly driven inertial confinement implosions, fewer studies had been performed that include the effects of CBET on the symmetry of direct-drive inertial confinement fusion implosions. This is because of the computational expense in including CBET physics in multidimensional simulations. Its effects are often substituted for the simpler, flux-limited Spitzer–Härm thermal-transport method, where the flux limiter is variable in time [i.e., variable flux limit (VFL)] and chosen to match the observables of more-detailed 1-D simulations, which include the nonlocal thermal transport (NLTT) and CBET physics. This new work by Kenneth Anderson (see p. 127) demonstrates that by including CBET in simulations with offset, implosion asymmetry caused by target offset is actually mitigated compared to the aforementioned substitutive models. The inset depicts the predicted power deposited by the laser in the  $\ell = 1$  mode when a target is offset. For most of the laser main drive, CBET losses dramatically reduce the  $\ell = 1$  mode compared to the commonly used VFL model. The main image then expands this result to multiple simulations across a wide variety of target offsets. We can see that the simulated yield trends show less degradation at high offset when CBET is included than when using the VFL model. These results are useful in highlighting the importance of the 3-D laser ray-trace model including CBET when modeling target offset to accurately capture this asymmetry mitigation and to give better agreement with experimental observables.

The figure on the right shows the enhanced scattered light predicted with CBET when target offset is present. More specifically, it shows more CBET occurring on the face of the target closer to target chamber center, where laser intensity is highest compared to the side facing away. In other words, this shows CBET counteracting the effects of offset-induced laser-illumination asymmetry.



This report was prepared as an account of work conducted by the Laboratory for Laser Energetics and sponsored by New York State Energy Research and Development Authority, the University of Rochester, the U.S. Department of Energy, and other agencies. Neither the above-named sponsors nor any of their employees makes any warranty, expressed or implied, or assumes any legal liability or responsibility for the accuracy, completeness, or usefulness of any information, apparatus, product, or process disclosed, or represents that its use would not infringe privately owned rights. Reference herein to any specific commercial product, process, or service by trade name, mark, manufacturer, or otherwise, does not necessarily constitute or imply its endorsement, recommendation, or favoring

by the United States Government or any agency thereof or any other sponsor. Results reported in the LLE Review should not be taken as necessarily final results as they represent active research. The views and opinions of authors expressed herein do not necessarily state or reflect those of any of the above sponsoring entities.

The work described in this volume includes current research at the Laboratory for Laser Energetics, which is supported by New York State Energy Research and Development Authority, the University of Rochester, the U.S. Department of Energy Office of Inertial Confinement Fusion under Cooperative Agreement No. DE-NA0003856, and other agencies.

Printed in the United States of America

Available from

National Technical Information Services  
U.S. Department of Commerce  
5285 Port Royal Road  
Springfield, VA 22161  
[www.ntis.gov](http://www.ntis.gov)

For questions or comments, contact Duc Cao, Editor, Laboratory for Laser Energetics, 250 East River Road, Rochester, NY 14623-1299, (585) 275-3352.

[www.lle.rochester.edu](http://www.lle.rochester.edu)

# LLE Review



## Quarterly Report

### Contents

<b>IN BRIEF</b> .....	iii
<b>INERTIAL CONFINEMENT FUSION</b>	
The Effect of Cross-Beam Energy Transfer on Target Offset Asymmetry in Directly Driven Inertial Confinement Fusion Implosions.....	127
Wavelength-Detuning Cross-Beam Energy Transfer Mitigation Scheme for Polar Direct Drive on SG-III .....	130
Direct-Drive Double-Shell Implosion: A Platform for Burning-Plasma Physics Studies.....	134
Density Measurements of the Inner Shell Release.....	138
The Role of Baroclinicity in the Kinetic Energy Budget.....	142
<b>PLASMA AND ULTRAFAST PHYSICS</b>	
Investigation of Picosecond Thermodynamics in a Laser-Produced Plasma Using Thomson Scattering .....	145
Measurement and Control of Ionization Waves of Arbitrary Velocity in the Quasi-Far Field.....	149
Photon Acceleration in a Flying Focus .....	153
Evolution of the Electron Distribution Function in the Presence of Inverse Bremsstrahlung Heating and Collisional Ionization .....	156
<b>HIGH-ENERGY-DENSITY PHYSICS</b>	
Crystalline Phase Transitions and Vibrational Spectra of Silicon up to Multi-TPa Pressures .....	159

**DIAGNOSTIC SCIENCE AND DETECTORS**

Inferred UV Fluence Focal-Spot Profiles from Soft X-Ray Pinhole Camera  
Measurements on OMEGA ..... 161

**MATERIALS SCIENCE**

Magnetically and Optically Tunable Terahertz Radiation from Ta/NiFe/Pt Spintronic  
Nanolayers Generated by Femtosecond Laser Pulses..... 164

**LASER TECHNOLOGY AND DEVELOPMENT**

Investigation of Mechanisms of Laser-Induced Secondary Contamination  
from Metal Particles Attached on the Input Surface of Optical Components..... 168

**NATIONAL LASER USERS' FACILITY AND EXTERNAL USERS' PROGRAM**

The 11th Omega Laser Facility Users Group Workshop ..... 172

**EDUCATION AND OUTREACH**

The Optics Suitcase: An Educational Outreach Tool for Inspiring Careers in Light ..... 175

**TARGET ENGINEERING AND RESEARCH**

Measurement for Palladium Hydride and Palladium Deuteride Isotherms  
Between 130 K and 393 K ..... 177

A Thin-Alumina Film as a Tritium Adsorption Inhibitor for Stainless-Steel 316 ..... 181

**LASER FACILITY REPORT**

FY19 Q3 Laser Facility Report ..... 184

**PUBLICATIONS AND CONFERENCE PRESENTATIONS**

## In Brief

This volume of LLE Review 159, covering the period April–June 2019, is sectioned among research areas at LLE and external users of the Omega Laser Facility. Articles appearing in this volume are the principal summarized results of long-form research articles. Readers seeking a more-detailed account of research activities are invited to seek out the primary materials appearing in print, detailed in the publications and presentations section at the end of this volume.

Highlights of research presented in this volume include the following:

- K. S. Anderson *et al.* present simulation data that suggest cross-beam energy transfer (CBET) as mitigating the deleterious effects of offset (p. 127). These simulations are shown to compare better against target experiments with offset when CBET is included.
- J. A. Marozas and E. M. Campbell present a design to field polar-direct-drive (PDD) experiments on the SG-III facility that include wavelength detuning for CBET mitigation (p. 130). Although some laser modifications are necessary at the facility, SG-III presents a viable alternative to the National Ignition Facility (NIF) to field PDD experiments and further progress in direct-drive inertial confinement fusion (ICF).
- S. X. Hu *et al.* present justification and simulation results for direct-drive double-shell implosions in order to better approach ignition (p. 134). In the NIF design presented, fusion energy yields of 0.3 to 1.0 MJ can be obtained according to high-mode *DRACO* simulations.
- D. Haberberger *et al.* detail measurements showing early material release on the backside of a CH shell at conditions relevant to ICF (p. 138). It is hypothesized that this phenomenon could be the cause for degraded performance in current ICF experiments.
- A. Lees and H. Aluie demonstrate how to include baroclinity into the energy budget through the use of scale decomposition (p. 142). Mechanisms for “baropycnal work” are also reproduced in direct numerical simulation results for compressible turbulence.
- A. S. Davies *et al.* present Thomson-scattering data showing electron density and temperature evolution in a laser-produced plasma over 50 ps (p. 145). The results suggest evolution was slower compared to calculations and propose limitations to transfer efficiencies in the linear regime for Raman plasma amplification.
- P. Franke *et al.* detail efforts to create and control ionization fronts using flying focus (p. 149). A theory was developed that reproduced the observed data.
- A. J. Howard *et al.* show theory and simulation results for photon frequency upshifting caused by ionization fronts created with a flying focus (p. 153). Analytic models predict this scheme could be a novel tabletop source of spatially coherent x rays.
- A. L. Milder *et al.* present Thomson-scattering data showing the picosecond evolution of a non-Maxwellian electron distribution for a  $2.4 \times 10^{14}$  W/cm<sup>2</sup> laser-produced plasma (p. 156). Calculations from the Vlasov–Fokker–Planck code K2 showed that ionization physics was necessary to reproduce the observed data.
- R. Paul, S. X. Hu, and V. V. Karasiev present a first-principles construction of a high pressure–temperature (up to 4 TPa and 26,000 K) phase diagram of Si that revealed new stable phases (p. 159). The methodology centered on Mermin’s extension of Kohn–Sham density functional theory and *ab initio* lattice dynamics of perfect crystals.

- W. Theobald *et al.* present a comparison between UV equivalent-target-plane (UVETP) measurements and x-ray target-plane (XTP) measurements for a variety of OMEGA beams (p. 161). Data show that beam-to-beam variation for the UVETP was within acceptable rms variation, while the XTP showed some beams to lie slightly outside the acceptable range.
- R. Adam *et al.* demonstrate the creation and control of electromagnetic transients through the use of Ta/NiFe/Pt spintronic nanolayers (p. 164). Data suggest the transients' amplitudes depend linearly on the average laser power illuminating the nanolayers, with blue lasers giving 3× the amplitude compared to an infrared laser for the same power.
- S. G. Demos *et al.* present laser-damage measurements from illuminating dispersed stainless-steel and titanium particles onto optical surfaces (p. 168). Results showcase three contamination mechanisms following the interaction of the laser pulse with the particles.
- M. Koepke *et al.* present summary information of the 11th Omega Laser Facility Users Group Workshop (p. 172). Also presented are user Findings and Recommendations to the Omega Laser Facility.
- J. DeGroot Nelson, T. Z. Kosc, and P. C. Nelson detail the contents of the optics suitcase for educational outreach (p. 175). Reusable and giveaway items are included and meant to quickly capture attention of students and encourage them to share with peers what they have learned.
- M. Sharpe, W. T. Shmayda, and K. Glance present measurements of a pressure–composition–temperature (PCT) phase diagram for palladium hydride and palladium deuteride at low temperatures (p. 177). The measured isotherms show an increasing formation of palladium hydride as the temperature is decreased to a maximum of 0.75 hydrogen-to-metal ratio.
- C. Fagan *et al.* present comparisons of hydrogen absorption for different samples of stainless-steel 316 with Al<sub>2</sub>O<sub>3</sub> coatings (p. 181). Results show that hydrogen absorption was more affected by a reduction of 300-nm to 5-nm surface roughness than by the presence of an Al<sub>2</sub>O<sub>3</sub> coating.
- J. Puth, M. Labuzeta, and D. Canning summarize operations of the Omega Laser Facility during the third quarter of FY19 (p. 184).

Duc Cao  
Editor

# The Effect of Cross-Beam Energy Transfer on Target Offset Asymmetry in Directly Driven Inertial Confinement Fusion Implosions

K. S. Anderson,<sup>1</sup> C. J. Forrest,<sup>1</sup> O. M. Mannion,<sup>1</sup> F. J. Marshall,<sup>1</sup> R. C. Shah,<sup>1</sup> D. T. Michel,<sup>1,2</sup> J. A. Marozas,<sup>1</sup> P. B. Radha,<sup>1</sup> D. H. Edgell,<sup>1</sup> R. Epstein,<sup>1</sup> V. N. Goncharov,<sup>1</sup> J. P. Knauer,<sup>1</sup> and M. Gatu Johnson<sup>3</sup>

<sup>1</sup>Laboratory for Laser Energetics, University of Rochester

<sup>2</sup>Applied and Theoretical Optics Department, ONERA, Palaiseau, France

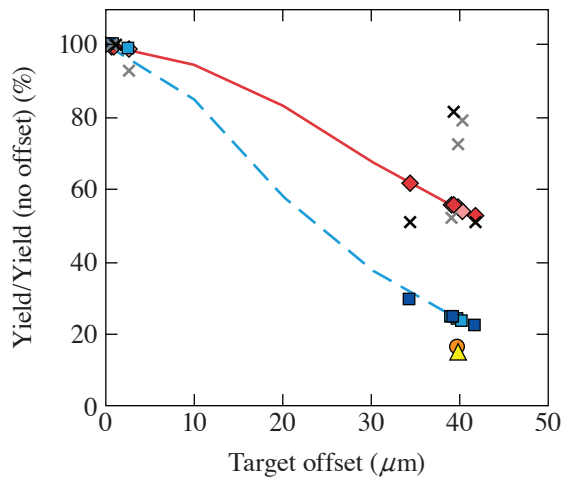
<sup>3</sup>Plasma Science and Fusion Center, Massachusetts Institute of Technology

It is well known that at typical inertial confinement fusion (ICF) laser intensities, cross-beam energy transfer (CBET)<sup>1</sup> can cause significant laser energy losses to directly driven inertial confinement implosions. When CBET occurs, incoming laser light from one beam interacts with refracted, outgoing light from other beams, stealing some energy from the incoming light and scattering that energy away from the target along the path of the outgoing light rays. The result is a decrease in the ablation pressure, implosion velocity, and compression of the capsule, leading to lower fusion yield. One-dimensional simulations of direct-drive implosions at LLE have for years included CBET physics to better model implosions. However, because of the computational expense of including CBET physics in multidimensional simulations, these have often used a simpler, flux-limited Spitzer–Härm thermal transport method, where the flux limiter is variable in time and chosen to match the observables of more-detailed 1-D simulations, which include the nonlocal thermal transport (NLTT) and CBET physics. Because of this, few studies have been performed that include the effects of CBET on the symmetry of direct-drive ICF implosions.

One major source of laser nonuniformity is target mispositioning or offset. When the target is mispositioned with respect to the center of convergence of the laser beams, a perturbation with a dominant  $\ell = 1$  mode is present in the illumination pattern on target, with the “hot side” (the side with higher illumination) being opposite the direction of the offset. Previous simulations without CBET have indicated that this  $\ell = 1$  offset perturbation persists in time at high amplitude, resulting in highly degraded yields and distorted hot spots, even when target offsets are small, of the order of  $10\ \mu\text{m}$  or about 2% of the radius of a typical capsule imploded on the 60-beam OMEGA Laser System. In contrast, fusion yields from cryogenic implosions on OMEGA show relatively low sensitivity to target offsets of this magnitude. This discrepancy between simulation and experiment has not been previously understood.

To study the effect of target offset in a more-controlled environment, experiments with room-temperature capsules were performed on OMEGA with prescribed offsets. These room-temperature experiments are simpler to field on OMEGA and require no cryogenic target handling or shroud, allowing more precise control of target positioning. Furthermore, these capsules have no cryogenic fuel layer, which typically represents a large and variable source of implosion nonuniformity and further complicates analysis. Results from these experiments were compared with 2-D *DRACO* simulations including the effects of CBET<sup>2</sup> plus a modified<sup>3</sup> Schurtz–Nicolai–Busquet nonlocal thermal transport model (CBET–NLTT) as well as no-CBET *DRACO* simulations using a variable flux limiter (VFL). These comparisons illustrate the effect of CBET on the  $\ell = 1$  laser drive uniformity, hot-spot x-ray core symmetry, and fusion yields. Note: the hydrodynamics and transport in *DRACO* are 2-D, but the laser ray-trace package is fully 3-D; this is sufficient to model target offset with CBET.

The normalized fusion yields from both the experiment and simulations are plotted in Fig. 1. The curves in Fig. 1 plot yields for *DRACO* simulations with varying offsets for a single shot (88575) with the CBET–NLTT model (solid red curve) and the VFL model (dashed blue curve). The simulations with the as-measured target offsets are shown with the red diamonds (CBET–NLTT)



TC14804JR

Figure 1

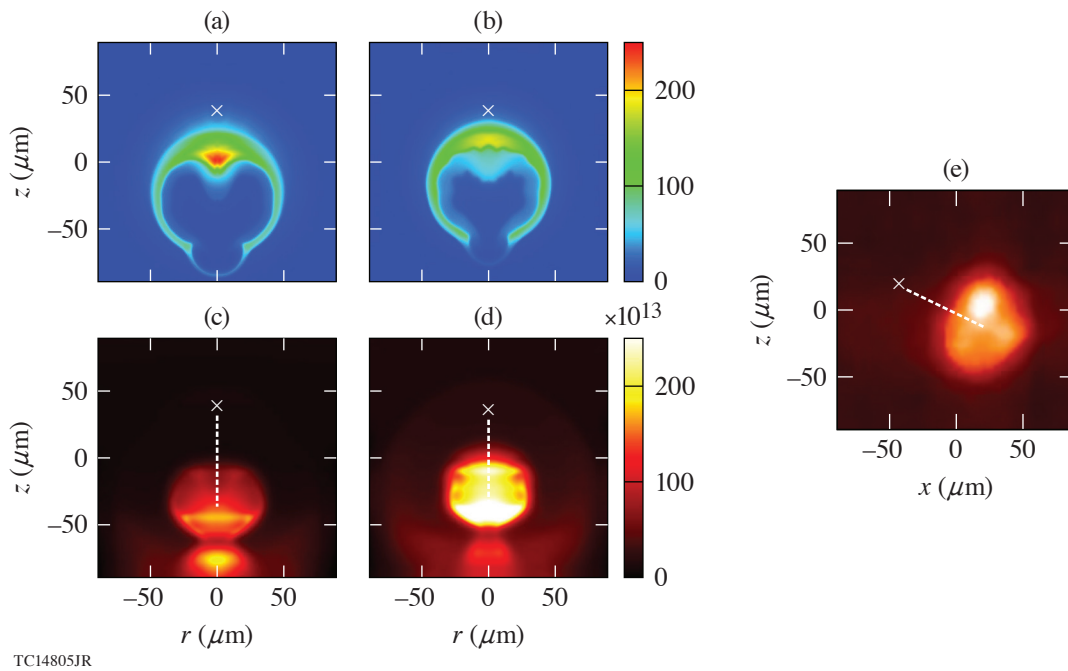
Normalized neutron yields for *DRACO* simulations (CBET–NLTT: red diamonds; VFL: blue squares) and experiment (×'s). D<sub>2</sub> shots are shown in the lighter shades. Normalized yield trend lines are shown for shot 88575 varying the target offset in simulations (CBET–NLTT: solid red curve; VFL: dashed blue curve). For comparison, two simulations with a power-imbalance-induced  $\ell = 1$  asymmetry equivalent to that of a 40- $\mu\text{m}$  target offset at  $t = 0$  were modeled (CBET–NLTT: orange circle; VFL: yellow triangle).

and blue squares (VFL). Experimental data are shown with the ×'s. Normalized yields are shown for both the D<sub>2</sub> shots (lighter shades) and DT shots (darker shades). The simulation data show that the fusion yields are less sensitive to target offset when the CBET–NLTT model is used versus the VFL model, and that this difference occurs even for small target offsets. The variation in experimental yields in the offset shots is assumed to result from directional interactions with the target-mounting stalk and other systematic and/or random variations between shots, which are not modeled in the simulations.

For the D<sub>2</sub> shots, four x-ray framing cameras were deployed to collect time-resolved images of the coronal x-ray emission during the acceleration phase of the implosion from four different views. These images were then used to infer the centroid of the capsule as a function of time using the methodology of Ref. 4. Simulated time-resolved images were generated by post-processing *DRACO* data with *Spect3D*.<sup>5</sup> The results from both experiment and simulation show that the center of the capsule experiences a linear spatial drift away from its initial position that is approximately linear when plotted versus the distance traveled by the shell. When the capsule radius had shrunk to  $\approx 150 \mu\text{m}$ , the distance traveled by the capsule center from the  $t = 0$  position in the offset shots was measured experimentally to be between 9.2 to 10.0  $\mu\text{m}$  along the offset direction with a 1.1- to 1.5- $\mu\text{m}$  movement orthogonal to the offset direction (the measurement uncertainty was  $\pm 1.0 \mu\text{m}$ ). The orthogonal movement is attributed to non-uniformity sources other than target offset. Reasonable agreement with experiment is seen in simulations with the CBET–NLTT model, which indicates the center drift along the offset direction is 12.0  $\mu\text{m}$ . By contrast, the VFL model predicts 16.6- $\mu\text{m}$  center drift, well outside the error bars.

On all shots, time-integrated x-ray images of the hot-spot core emission were obtained from the gated monochromatic x-ray imager (GMXI). The centroid of the core x-ray image was then calculated with respect to that of the target chamber center (TCC) reference shot for each series (D<sub>2</sub> and DT) to quantify the distance of the core in each offset shot relative to the reference target, following the methodology of Ref. 6. Time-integrated simulated images of the core x-ray emission were also generated from *DRACO* using *Spect3D* to compare with the GMXI images. The data are shown in Fig. 2. Figures 2(a) and 2(c) are the density contour of the target at peak compression and the time-integrated x-ray image from the VFL *DRACO* and *Spect3D* of shot 88581, respectively, whereas Figs. 2(b) and 2(d) are the same, respectively, for the CBET–NLTT model. Figure 2(e) is the experimental image. In each image, the position of TCC is shown with an ×. The same analysis was done for the TCC reference shot 88578. Analysis shows that the distances between the centroid of x-ray emission of shots 88581 and 88578 are  $61 \pm 2 \mu\text{m}$  for the experiment and 63  $\mu\text{m}$  and 71  $\mu\text{m}$  for the simulated CBET–NLTT and VFL, respectively. Only the CBET–NLTT result fits within the experimental error bars.

This mitigation of offset-induced nonuniformity by CBET effects can be understood geometrically. The shift of the target away from the center of beam convergence means that more laser light refracts past the target to interact with the incoming beams on the hot side, relative to those on the cold side. This stimulates more CBET losses on the hot side than on the cold side, effectively reducing the  $\ell = 1$  illumination nonuniformity. This effect is also observed in simulations and experiments of polar-drive experi-



TC14805JR

Figure 2

Density plot ( $\text{g}/\text{cm}^3$ ) at stagnation from *DRACO* simulations of shot 88581 with (a) VFL and (b) CBET–NLTT. Simulated time-integrated x-ray images generated by *Spect3D* from these simulations are shown in (c) VFL and (d) CBET–NLTT. (e) The experimental image from GMX1c. In all images, the location of TCC is shown by the  $\times$  and the distance between TCC and centroid of emission indicated by the dashed white line.

ments<sup>2</sup> that show CBET is higher at the equator where beams are pointed away from the target center to improve illumination uniformity, and in experiments where the beam-to-target ratio is reduced<sup>7</sup> to mitigate CBET. *DRACO*'s in-line scattered-light diagnostics support this conclusion, showing enhanced CBET-scattered light from the hot side of the target. To illustrate that this is a geometric effect arising from target offset, both CBET–NLTT and VFL *DRACO* simulations were performed, inducing an  $\ell = 1$  using a prescribed laser power imbalance with the same initial mode amplitude as with the target offset of  $40 \mu\text{m}$ . The resulting normalized yields, shown in Fig. 1 by the orange circle (CBET–NLTT) and yellow triangle (VFL), are very close to each other and similar to the yield of the VFL offset simulation, indicating no mitigation of the power-imbalance–induced  $\ell = 1$  by CBET.

In conclusion, CBET in direct-drive inertial confinement mitigates the implosion asymmetry caused by target offset. Simulations modeling target offset require a 3-D laser ray-trace model including CBET to accurately capture this asymmetry mitigation and to give better agreement with experimental observables.

This material is based upon work supported by the Department of Energy National Nuclear Security Administration under Award Number DE-NA0003856, the University of Rochester, and the New York State Energy Research and Development Authority.

1. I. V. Igumenshchev *et al.*, *Phys. Plasmas* **17**, 122708 (2010).
2. J. A. Marozas *et al.*, *Phys. Rev. Lett.* **120**, 085001 (2018).
3. D. Cao, G. Moses, and J. Delettrez, *Phys. Plasmas* **22**, 082308 (2015).
4. D. T. Michel *et al.*, *Phys. Rev. Lett.* **120**, 125001 (2018).
5. J. J. MacFarlane *et al.*, *High Energy Density Phys.* **3**, 181 (2007).
6. W. Grimble, F. J. Marshall, and E. Lambrides, *Phys. Plasmas* **25**, 072702 (2018).
7. D. H. Froula *et al.*, *Phys. Rev. Lett.* **108**, 125003 (2012).

# Wavelength-Detuning Cross-Beam Energy Transfer Mitigation Scheme for Polar Direct Drive on SG-III

J. A. Marozas and E. M. Campbell

Laboratory for Laser Energetics, University of Rochester

## Introduction

In direct-drive inertial confinement fusion (ICF), laser beams irradiate a plastic-coated shell of frozen deuterium–tritium (DT) and ablatively drive an implosion. The ultimate goal of ICF is ignition and energy gain; the minimum shell kinetic energy required for ignition (defined as when the energy from DT fusion reactions exceeds the laser energy incident on the target) is given by  $E_{\min} \sim \alpha^{1.88} P_{\text{abl}}^{-0.77} v_{\text{imp}}^{-5.89}$  (Ref. 1), where the three parameters of the implosion— $\alpha$ ,  $v_{\text{imp}}$ , and  $P_{\text{abl}}$  [adiabat (the ratio of the fuel pressure to the Fermi-degenerate pressure at peak implosion velocity), implosion velocity, and ablation pressure, respectively]—are determined primarily by the deposition of the laser energy into the coronal plasma of the target and heat conduction to the ablation surface. Cross-beam energy transfer (CBET)<sup>2</sup> has been identified in direct-drive experiments on the OMEGA<sup>3</sup> and National Ignition Facility (NIF)<sup>4</sup> lasers to reduce absorption, ablation pressure, and implosion velocity. The presence of CBET on the SG-III facility<sup>5</sup> is anticipated to cause similar issues by reducing target absorption and the resulting reduction in ablation pressure and implosion velocity.

CBET laser–plasma interaction results from two-beam energy exchange via stimulated Brillouin scattering,<sup>2</sup> which reduces absorbed light and consequently reduces ablation pressure and implosion velocity. The dominant CBET loss mechanism in direct drive occurs when rays counter-propagate (backscatter mode), increasing scattered light, as illustrated in Fig 1. For the ignition-relevant overlapped beam intensities of  $\sim 8 \times 10^{14} \text{ W/cm}^2$  for NIF experiments, CBET is calculated to reduce laser absorption by 22%, the average implosion speed

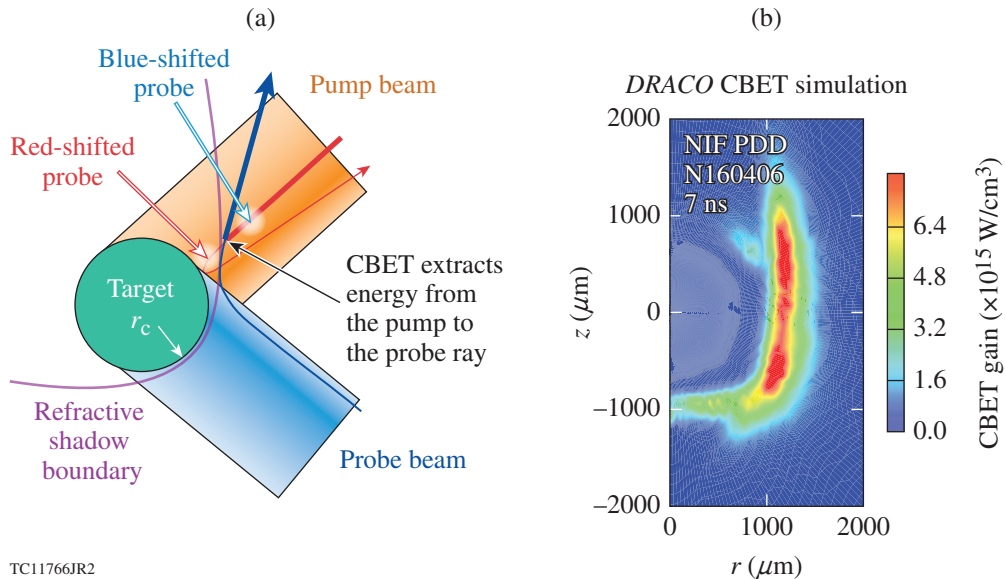
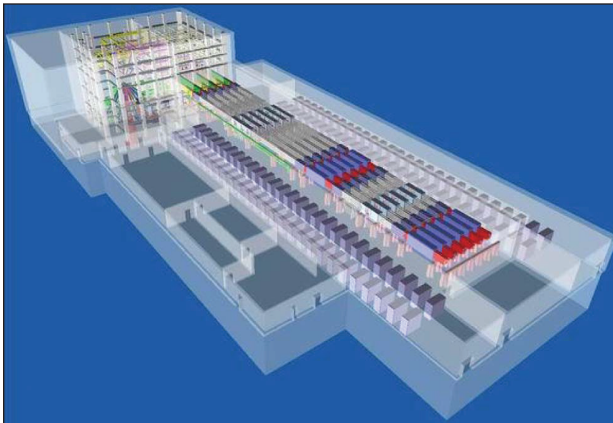


Figure 1 (a) The effect of cross-beam energy transfer (CBET) (backscatter mode) in polar direct drive (PDD) predominantly affects the equatorial region where rays interact. (b) The CBET effect dominates the equatorial region, as shown where successful CBET mitigation benefits the same region.

by  $\sim 9\%$ , and the average ablation pressure by 35% (Ref. 6). These drive-related results are consistent with other ongoing OMEGA-<sup>7</sup> and NIF-scale<sup>8</sup> experiments. Reducing the target mass compensates for CBET losses, but the thinner shells become compromised as a result of hydrodynamic instability growth.<sup>9</sup> As shown by the above equation for  $E_{\min}$ , efficient laser–energy coupling and hydrodynamic stability are essential aspects of direct-drive ICF, making CBET mitigation vital. Mitigation strategies of the deleterious CBET effects invoke combinations of spatial, temporal, and wavelength domains. Wavelength detuning works by altering the resonance condition between interacting beams.<sup>2</sup> Wavelength detuning was first examined for indirect drive<sup>10</sup> and subsequently for direct drive, but it was prematurely dismissed as a viable option.<sup>11</sup> Wavelength detuning was shown to mitigate CBET on the NIF in direct-drive experiments and to increase the drive relative to a no-detuning case;<sup>6</sup> DRACO simulations predict similar expectations on the SG-III facility.

### Laser Facility and CBET Mitigation

The SG-III facility (see Fig. 2) has a similar indirect-drive configuration as the NIF, albeit with a single beam in each port as compared to NIF’s quad architecture.<sup>6,12</sup> The SG-III facility provides a potential collaboration between LLE and SG-III. The indirect-drive beam geometry distributes the beam ports toward the poles of the target interaction chamber, forming cones of beams with a common polar angle.<sup>13</sup> This configuration must be altered to perform direct-drive experiments with a reasonably uniform drive. Repointing higher-intensity beams from lower latitudes toward the equator partially compensates for the indirect-drive port geometry and higher incident angles when illuminating direct-drive targets. In this modified configuration, referred to as polar direct drive (PDD),<sup>14,15</sup> CBET predictably dominates in the equatorial region,<sup>6,12</sup> where most of the cross-beam interactions occur, as shown in Fig. 1(b). As a result, PDD implosions tend to become oblate because CBET reduces the laser drive preferentially in the equatorial region. With this motivation, a basic wavelength-detuning strategy exploits the PDD configuration, where each hemisphere has a different wavelength or color. However, the nominal symmetric wavelength mapping on the NIF developed for indirect-drive targets precludes achieving hemispheric wavelength detuning using typical PDD repointing configurations.<sup>15</sup> A beam repointing method, called cone swapping,<sup>12</sup> was utilized on the NIF; it permits a partial hemispheric wavelength difference about the equator. The SG-III facility is assumed here to provide a more flexible color-to-beam mapping than available on the NIF. Cone swapping could still be applied to the SG-III facility if required but would produce nonoptimal results. For the purposes of this summary, the SG-III facility is assumed to provide three separate initial colors or wavelength shifts  $\Delta\lambda_0 = \{\lambda_1, \lambda_2, \lambda_3\}$  detuned from a central wavelength  $\lambda_0 \sim 351$  nm. The colors would be used to establish a bi- or tricolor distribution about the northern and southern hemispheres and yield the primary CBET mitigation strategy in any ICF direct-drive laser system.



TC14723JR

Figure 2

The SG-III facility has a similar indirect-drive configuration as the NIF, albeit with single beams in each port as compared to NIF’s quad architecture. The SG-III facility provides a potential collaboration between LLE and SG-III.

The far-field spot envelope [induced from distributed phase plates (DPP’s)<sup>16</sup> and small-divergence smoothing] determines the overlapped nonuniformity on any direct-drive ICF laser system. For the PDD configuration, care is taken to design the spot shapes to account for necessary repointing of the beams toward the equator. An ideal PDD spot shape minimizes any energy that would otherwise be projected over the target horizon when repointed, while maintaining the best underlying beam profile using a method referred to as spot-masking apodization (SMA); this provides a substantial energy savings of  $\sim 15\%$  to  $20\%$  (Ref. 17). In addition to the consideration of over-the-horizon energy loss, SMA can be employed as a CBET mitigation method by reducing the outer perimeter of the spot shape to a value that slightly underfills the full target diameter without severely effecting overlap

nonuniformity like smaller spots.<sup>12</sup> Current SG-III spot shapes could be used in the interim (similar to experiments on the NIF<sup>6</sup>) before optimized DPP's are designed and manufactured.

**Simulations Predictions**

The initial proposed target designs for SG-III are an energy-scaled version of the first wavelength-detuning experiments performed on the NIF.<sup>6</sup> The warm plastic (CH) target is 640 μm in radius and has a 55-μm-thick CH shell filled with 20 atm of D<sub>2</sub> fuel at room temperature (see Fig. 3). A 100-kJ energy reference pulse provides the drive for the PDD target. This average pulse is a composite of different scaled energies for each ring of beams, where the different energies provide a nearly uniform drive that compensates for angular hydroefficiencies: the intensity on target near the equatorial region is larger than that near the polar region. The nonuniform delivered on-target intensity compensates for higher refraction suffered by equatorial rays as well as the lower hydrodynamic efficiency in that region. The pulse shape shown here would drive the target slowly (~300 μm/ns) to avoid large hydrodynamic instability growth seeded by laser imprint. Initial experiments would focus on the CBET mitigation properties and not initially on the fusion performance.

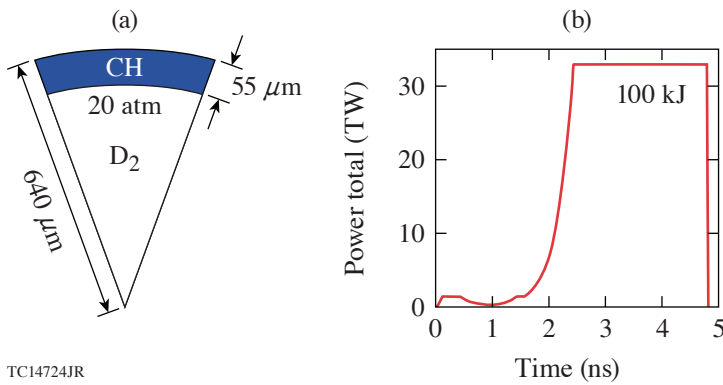


Figure 3  
 (a) The SG-III warm plastic (CH) target is 640 μm in radius and has a 55-μm-thick CH shell filled with 20 atm of D<sub>2</sub> fuel at room temperature. (b) The 100-kJ pulse provides a modest drive that could be enhanced after initial experiments.

TC14724JR

The PDD repointing configuration suggested for the SG-III facility closely resembles what was recently shot on the NIF, where four rings of beams are distributed about the target surface (see Fig. 4). The PDD repointing configuration provides reasonable control of shock and shell uniformity during the implosion for the SG-III facility. The exact locations of the repointed spots can vary slightly for different target designs to optimize nonuniformity.

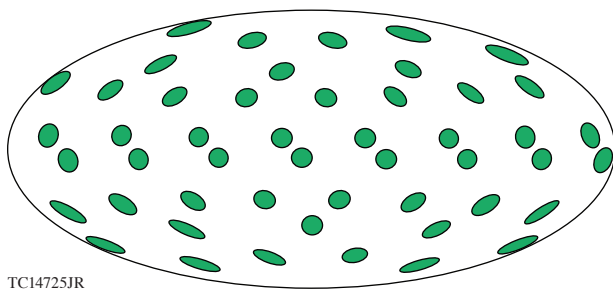


Figure 4  
 The suggested PDD repointing configuration provides reasonable control of shock and shell uniformity during the implosion for the SG-III facility, where four rings of beams are distributed about the target surface. Each green spot represents a beam port that has been repointed onto the initial target surface. The Hammer projection mapping is used.

TC14725JR

Preliminary DRACO<sup>12</sup> simulations for the proposed PDD CBET mitigation experiments for the SG-III facility indicate promising results (see Fig. 5). These simulations show that reasonable uniformity can be achieved, assuming nonideal spot shapes that conform to those currently employed on the NIF. Simulations performed in the NIF's configuration using optimal DPP's have shown significant improvement in uniformity, which has boosted neutron yields by 2× to 3× in exploding-pusher configurations when compared to nonideal spot shapes.

**Conclusion**

The SG-III facility could provide a valuable platform to explore CBET mitigation in the PDD configuration in the 200-kJ energy range. CBET mitigation experiments would require some laser modifications to measure the mitigation efficacy such as

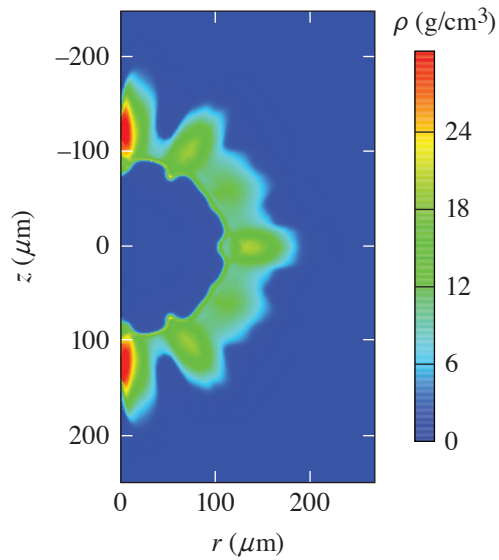


Figure 5  
Initial *DRACO*<sup>12</sup> simulation results for PDD  
CBET mitigation experiments for the SG-III  
facility indicate promising results.

TC14726JR

multiple tunable laser wavelengths, customized DPP's, and direct-drive target filling and manipulators. Higher shot repetition is expected, together with the ability to test a wide range of wavelength separation. The data that SG-III could provide would be valuable for future progress in direct-drive ICF.

This material is based upon work supported by the Department of Energy National Nuclear Security Administration under Award Number DE-NA0003856, the University of Rochester, and the New York State Energy Research and Development Authority.

1. M. C. Herrmann, M. Tabak, and J. D. Lindl, *Nucl. Fusion* **41**, 99 (2001).
2. C. J. Randall, J. R. Albritton, and J. J. Thomson, *Phys. Fluids* **24**, 1474 (1981).
3. T. R. Boehly *et al.*, *Opt. Commun.* **133**, 495 (1997).
4. E. M. Campbell and W. J. Hogan, *Plasma Phys. Control. Fusion* **41**, B39 (1999).
5. W. Zheng *et al.*, *High Power Laser Sci. Eng.* **4**, e21 (2016).
6. J. A. Marozas *et al.*, *Phys. Rev. Lett.* **120**, 085001 (2018).
7. P. B. Radha *et al.*, *J. Phys.: Conf. Ser.* **688**, 012006 (2016).
8. M. Hohenberger *et al.*, *Phys. Plasmas* **22**, 056308 (2015).
9. V. N. Goncharov *et al.*, *Phys. Plasmas* **21**, 056315 (2014).
10. P. Michel *et al.*, *Phys. Plasmas* **17**, 056305 (2010).
11. I. V. Igumenshchev *et al.*, *Phys. Plasmas* **19**, 056314 (2012).
12. J. A. Marozas *et al.*, *Phys. Plasmas* **25**, 056314 (2018).
13. M. L. Spaeth *et al.*, *Fusion Sci. Technol.* **69**, 25 (2016).
14. S. Skupsky *et al.*, *Phys. Plasmas* **11**, 2763 (2004).
15. J. A. Marozas *et al.*, *Phys. Plasmas* **13**, 056311 (2006).
16. J. A. Marozas, *J. Opt. Soc. Am. A* **24**, 74 (2007).
17. J. A. Marozas *et al.*, *J. Phys.: Conf. Ser.* **717**, 012107 (2016).

# Direct-Drive Double-Shell Implosion: A Platform for Burning-Plasma Physics Studies

S. X. Hu,<sup>1</sup> R. Epstein,<sup>1</sup> W. Theobald,<sup>1</sup> H. Xu,<sup>2</sup> H. Huang,<sup>2</sup> V. N. Goncharov,<sup>1</sup> S. P. Regan,<sup>1</sup> P. W. McKenty,<sup>1</sup> R. Betti,<sup>1</sup>  
E. M. Campbell,<sup>1</sup> and D. S. Montgomery<sup>3</sup>

<sup>1</sup>Laboratory for Laser Energetics, University of Rochester

<sup>2</sup>General Atomics

<sup>3</sup>Los Alamos National Laboratory

Laser-driven inertial confinement fusion<sup>1</sup> (ICF) has been actively pursued in the laboratory for decades. The current efforts have focused mainly on the so-called “hot-spot” ignition scheme, in which a single shell containing a solid-DT (deuterium–tritium) fuel layer covered by ablator materials is driven to implode by high-energy laser beams in either an *indirect* or *direct* way. In indirect-drive ICF, the high-energy laser beams irradiate inside a hohlraum and convert the laser energy into thermal x-ray emissions that ablatively drive the capsule (placed inside the hohlraum) to implode;<sup>2,3</sup> while for the other scheme, the laser beams *directly* irradiate the ICF target.<sup>4,5</sup> For hot-spot ignition in both schemes, the single shell acts not only as the “piston” but also provides the major DT fuel for the final hot-spot formation. For the piston to have enough energy and still be compressible at stagnation, one needs to drive the single shell for a long distance (for enough acceleration) and to maintain it at a relatively low entropy state (low adiabat). Roughly speaking, for such single-shell hot-spot ignition to work at laser energies in the MJ range, the imploding DT-containing shell must have a velocity of  $V_{\text{imp}} > 350$  km/s and a high convergence ratio of  $\text{CR} > 30$  ( $\text{CR} = R_0/R_{\text{hs}}$ , with  $R_0$  being the initial shell radius and  $R_{\text{hs}}$  the final hot-spot radius). These requirements impose formidable challenges for the central-spot–ignition scheme to reach the so-called *burning-plasma stage*,<sup>6</sup> in which the self-heating of plasmas by the DT-fusion–produced  $\alpha$  particles exceeds the radiative and conduction loss.

To reach the burning-plasma stage, the single-shell hot-spot ignition in both direct-drive and indirect-drive schemes must overcome daunting challenges, especially for the current low-margin designs due to the limited laser energy. First of all, the large CR, low adiabat, and high implosion velocity demand stringent requirements on target and driver perturbations. For example, 3-D simulations of indirect-drive ICF implosions<sup>7,8</sup> show that the driver asymmetry and target engineering features such as fill tube and interface mixing can gradually “eat” away the design margin for burning plasma to happen. The situation is also similar for direct-drive, high-convergence ICF implosions, in which the perturbations from target imperfection and long-/short-wavelength laser nonuniformities can also significantly degrade the target performance,<sup>9–12</sup> due to the fact that these high-convergence, low-adiabat single-shell implosions are highly susceptible to violent Rayleigh–Taylor (RT) instability growth.<sup>13–17</sup> In addition, the DT layer being part or the whole of the piston requires tremendous effort to maintain its low entropy. Precisely timing several shocks<sup>18–20</sup> is necessary to set the shell in a designed low adiabat. Still, excessive radiation and/or superthermal electrons produced by laser–plasma instabilities, such as two-plasmon decay<sup>21</sup> and stimulated Raman scattering,<sup>22</sup> could possibly preheat the in-flight, low-temperature DT shell and render it less compressible at stagnation. All of these challenges are currently faced by the laser-drive ICF community.

Different from the above-mentioned central-spot ignition, alternative laser-fusion schemes seek to separate the hot-spot formation from the shell (piston) acceleration. Over the past two decades, some efforts in the laser-fusion community have been put into studies of these alternative schemes, including fast ignition,<sup>23</sup> shock ignition,<sup>24,25</sup> double-shell implosions,<sup>26–31</sup> and a triple-shell *Revolver* design,<sup>32</sup> just to name a few. Although these schemes have their own challenges, the separation of hot-spot formation from accelerating the piston generally relaxes the stringent requirements for the single-shell, hot-spot–ignition scheme.

Taking a double-shell implosion as an example, the outer shell (piston) can be set at a much higher adiabat so that RT instability and radiation/fast-electron preheat do not significantly affect the shell integrity as it accelerates, while an inner shell composed of high-density metal layer(s) and filled with DT gas or liquid can be volumetrically shocked/compressed and heated by an  $\sim$ Gbar pressure reservoir that is created through the spherical stagnation (impact) of the outer shell upon the inner one. Given the electron-rich nature of a high-density inner shell, only a significantly low convergence ratio ( $CR \leq 10$ ) is needed to reach a pressure of  $\sim 400$  Gbar required for DT plasma burning.<sup>31</sup> The double-shell scheme generally trades some of the physics challenges of high-convergence ( $CR \geq 30$ ) single-shell implosions for the complexity of double-shell target fabrication and diagnoses.

For the past two decades, the study of double-shell implosions in both experiments and simulations has focused mainly on the indirect-drive scheme.<sup>26–31</sup> With a drive laser at the National Ignition Facility<sup>33</sup> (at an  $\sim$ MJ energy level), recent 1-D simulations showed that a maximum energy of only  $\sim 10$  to 15 kJ can be coupled to the kinetic motion of the inner shell,<sup>31</sup> even with a high-density inner-shell material like Au. The limited margin for an energetic inner shell is caused by the lower hydroefficiency in the indirect-drive scheme, in which a much thicker and massive outer shell is needed for x-ray drive. Motivated by the higher overall hydroefficiency of direct drive,<sup>5,10</sup> we have performed a thorough investigation on whether or not a direct-drive double-shell (D<sup>3</sup>S) platform has its own merit to create a burning plasma in the laboratory at MJ laser energy. We found that even with the currently reduced hydrocoupling caused by cross-beam energy-transfer (CBET),<sup>34–37</sup> direct-drive double-shell implosions can give at least twice the kinetic energy ( $\sim 30$  kJ) as the indirect-drive case; such a more-energetic inner shell could provide more margin to reach the DT-plasma burning stage. In addition, we propose to use the newly invented technology of magnetron sputtering<sup>38</sup> to make a density-gradient inner shell of a tungsten/beryllium mixture. By varying the tungsten-to-beryllium concentration ratio, one may be able to construct an inner shell with density dropping from  $\rho_0 \sim 19$  g/cm<sup>3</sup> (97% W + 3% Be) to  $\rho_0 \sim 2.2$  g/cm<sup>3</sup> (1% W + 99% Be) along both inward and outward directions. The idea of using gradient-density layers, proposed earlier for single-shell ICF,<sup>16</sup> can help to mitigate the classical RT problem during the outer-shell collision.<sup>39</sup> It not only reduces the Atwood number but also increases the density scale length at the collisional surface. It can be thought of as multiple “tamper” layers used for indirect-drive double-shell designs<sup>28,29,31</sup> but with a gradual density variation.

In the radiation-hydrodynamic studies of direct-drive double-shell implosions presented here, we have used both the 1-D code *LILAC*<sup>40</sup> and the 2-D code *DRACO*<sup>41</sup> developed at LLE. State-of-the-art physics models, including the nonlocal thermal-transport model,<sup>42,43</sup> the 3-D ray tracing with CBET model,<sup>34–37</sup> accurate material properties such as first-principles equation of state,<sup>44–47</sup> first-principles opacity tables,<sup>48,49</sup> and the average-ion model<sup>50</sup> for the opacity and emissivity of the W/Be mixture, have been employed in our radiation-hydrodynamic simulations. In our D<sup>3</sup>S designs, a 70- $\mu$ m-thick beryllium outer shell is driven symmetrically by a high-adiabat ( $\alpha \geq 10$ ), 1.9-MJ laser pulse to a peak velocity of  $\sim 240$  km/s. Upon spherical impact, the outer shell transfers  $\sim 30$  to 40 kJ of kinetic energy to the inner shell filled with DT gas or liquid, giving neutron-yield energies of  $\sim 6$  MJ in 1-D simulations. Two-dimensional, high-mode *DRACO* simulations indicated that such high-adiabat D<sup>3</sup>S implosions are not susceptible to laser imprint, but the long-wavelength perturbations from the laser port configuration along with CBET can be detrimental to the target performance. Nevertheless, neutron yields of  $\sim 0.3$ - to 1.0-MJ energies can still be obtained from our high-mode *DRACO* simulations. One example is shown in Fig. 1, where the robust  $\alpha$ -particle bootstrap is readily reached, which could provide a viable platform for burning-plasma physics studies. Once CBET mitigation and/or more laser energy becomes available, we anticipate that breakeven or moderate energy gain might be feasible with the proposed D<sup>3</sup>S scheme.

This material is based upon work supported by the Department of Energy National Nuclear Security Administration under Award Number DE-NA0003856, the University of Rochester, and the New York State Energy Research and Development Authority.

1. J. Nuckolls *et al.*, *Nature* **239**, 139 (1972).
2. J. D. Lindl, *Phys. Plasmas* **2**, 3933 (1995).
3. M. J. Edwards *et al.*, *Phys. Plasmas* **18**, 051003 (2011).
4. D. D. Meyerhofer *et al.*, *Nucl. Fusion* **51**, 053010 (2011).
5. R. S. Craxton *et al.*, *Phys. Plasmas* **22**, 110501 (2015).

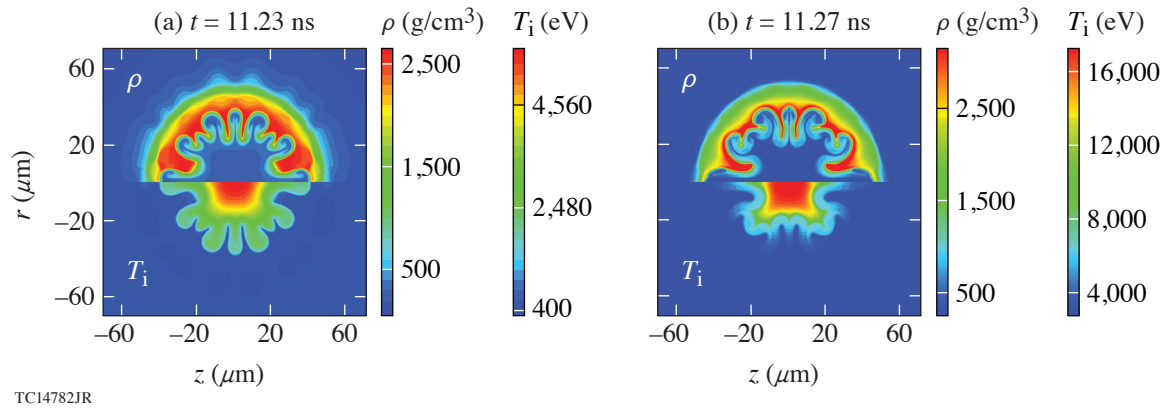


Figure 1

The density ( $\rho$ ) and ion temperature ( $T_i$ ) contour plots on the  $r, z$  plane during the inner-shell stagnation: (a) at the beginning of bootstrap heating ( $t = 11.23$  ns) and (b) at the peak neutron production ( $t = 11.27$  ns) when the burning-plasma stage is reached.

6. R. Betti and O. A. Hurricane, *Nat. Phys.* **12**, 435 (2016).
7. D. S. Clark *et al.*, *Phys. Plasma* **25**, 032703 (2018).
8. D. S. Clark *et al.*, *Nucl. Fusion* **59**, 032008 (2018).
9. I. V. Igumenshchev *et al.*, *Phys. Plasmas* **20**, 082703 (2013).
10. V. N. Goncharov *et al.*, *Phys. Plasmas* **21**, 056315 (2014).
11. S. X. Hu *et al.*, *Phys. Plasmas* **23**, 102701 (2016).
12. D. T. Michel *et al.*, *Phys. Rev. E* **95**, 051202(R) (2017).
13. S. E. Bodner, *Phys. Rev. Lett.* **33**, 761 (1974).
14. H. Takabe *et al.*, *Phys. Fluids* **28**, 3676 (1985).
15. R. Betti *et al.*, *Phys. Plasmas* **5**, 1446 (1998).
16. N. Metzler, A. L. Velikovich, and J. H. Gardner, *Phys. Plasmas* **6**, 3283 (1999).
17. V. A. Smalyuk *et al.*, *Phys. Rev. Lett.* **103**, 105001 (2009).
18. T. R. Boehly *et al.*, *Phys. Plasmas* **16**, 056302 (2009).
19. T. R. Boehly *et al.*, *Phys. Plasmas* **18**, 092706 (2011); *Phys. Rev. Lett.* **106**, 195005 (2011).
20. H. F. Robey *et al.*, *Phys. Plasmas* **19**, 042706 (2012).
21. D. T. Michel *et al.*, *Phys. Rev. Lett.* **109**, 155007 (2012).
22. M. J. Rosenberg *et al.*, *Phys. Rev. Lett.* **120**, 055001 (2018).
23. M. Tabak *et al.*, *Phys. Plasmas* **1**, 1626 (1994).
24. R. Betti *et al.*, *Phys. Rev. Lett.* **98**, 155001 (2007).
25. W. Theobald *et al.*, *Phys. Plasmas* **19**, 102706 (2012).
26. W. S. Varnum *et al.*, *Phys. Rev. Lett.* **84**, 5153 (2000).
27. P. Amendt *et al.*, *Phys. Plasmas* **9**, 2221 (2002).

28. J. Milovich *et al.*, Phys. Plasmas **11**, 1552 (2004).
29. P. A. Amendt *et al.*, Phys. Rev. Lett. **94**, 065004 (2005).
30. H. F. Robey *et al.*, Phys. Rev. Lett. **103**, 145003 (2009).
31. D. S. Montgomery *et al.*, Phys. Plasmas **25**, 092706 (2018).
32. K. Molvig *et al.*, Phys. Rev. Lett. **116**, 255003 (2016).
33. E. M. Campbell and W. J. Hogan, Plasma Phys. Control. Fusion **41**, B39 (1999).
34. C. J. Randall, J. J. Thomson, and K. G. Estabrook, Phys. Rev. Lett. **43**, 924 (1979).
35. I. V. Igumenshchev *et al.*, Phys. Plasmas **17**, 122708 (2010).
36. D. H. Froula *et al.*, Phys. Plasmas **20**, 082704 (2013).
37. J. A. Marozas *et al.*, Phys. Plasmas **25**, 056314 (2018).
38. H. Xu *et al.*, Fusion Sci. Technol. **73**, 354 (2018).
39. J. D. Lindl *et al.*, Phys. Plasmas **11**, 339 (2004).
40. J. Delettrez *et al.*, Phys. Rev. A **36**, 3926 (1987).
41. P. B. Radha *et al.*, Phys. Plasmas **12**, 056307 (2005).
42. G. P. Schurtz, Ph. D. Nicolai, and M. Busquet, Phys. Plasmas **7**, 4238 (2000).
43. D. Cao, G. Moses, and J. Delettrez, Phys. Plasmas **22**, 082308 (2015).
44. S. X. Hu *et al.*, Phys. Rev. Lett. **104**, 235003 (2010).
45. S. X. Hu *et al.*, Phys. Rev. B **84**, 224109 (2011).
46. S. X. Hu *et al.*, Phys. Rev. E **92**, 043104 (2015).
47. Y. H. Ding and S. X. Hu, Phys. Plasmas **24**, 062702 (2017).
48. S. X. Hu *et al.*, Phys. Rev. E **90**, 033111 (2014).
49. S. X. Hu *et al.*, Phys. Rev. B **96**, 144203 (2017).
50. R. Epstein *et al.*, Bull. Am. Phys. Soc. **43**, 1666 (1998).

## Density Measurements of the Inner Shell Release

D. Haberberger, A. Shvydky, J. P. Knauer, S. X. Hu, S. T. Ivancic, J. Carroll-Nellenback, D. Cao, V. V. Karasiev,  
A. V. Maximov, V. N. Goncharov, and D. H. Froula

Laboratory for Laser Energetics, University of Rochester

The material release on the back side of a CH shell was probed at conditions relevant to inertial confinement fusion (ICF). The release was found to expand further with a longer scale length than that predicted by radiation-hydrodynamic simulations. The simulations show that a relaxation of the back side of the shell consistent with measurements explains the experimentally observed reduction in ICF implosion performance—specifically reduced areal density at peak compression.

While great progress has been made over recent years in ICF experiments,<sup>1</sup> achieving ignition conditions remains a grand challenge. In both direct- and indirect-drive approaches to fusion, a cold layer of deuterium–tritium (DT) fuel is compressed by material ablation to form a high-areal-density confinement around an igniting central hot spot. In both approaches, several shocks are launched through an outer solid-density fuel and into a central vapor region. Once the shock breaks through the inner surface into the central region, the fuel spherically converges to form a high-areal-density confinement. By limiting the amount of material and maintaining a low temperature inside the vapor region, the implosion can reach maximum convergence and the hot-spot temperature necessary for ignition.

One of the reasons for the underperformance in the recent experiments is attributed to a reduced areal density of the fuel; 20% deficiency has been reported for most of the implosions at the National Ignition Facility.<sup>2</sup> Several mechanisms could contribute to the reduction in shell convergence and therefore in areal density, including mixing of the ablator material into the fuel or mixing of the fuel into the central hot spot. In addition, inaccurate modeling of the material properties of fuel interacting with multiple strong shocks could lead to an underprediction of the mass expanding from the inner surface of the main shell by material release. Such a release is created as the first shock breaks out of the main fuel into the vapor region of the target. As subsequent shocks with increasing strengths are launched into the shell at the beginning of the implosion, they travel through the rarefaction formed by the earlier shocks. The rate of material release is determined by several factors, including sound speed, ion viscosity, and thermal conduction.

Experimental signatures of the driven shell dynamics are commonly used to test hydrodynamic simulations. In implosion experiments, x-ray backlighting or self-emission measurements are used to track the shell trajectory,<sup>3</sup> but they give no information about the low-density material release behind the shell since the low-density material does not attenuate the high-energy x-ray photons. Optical probing with a velocity interferometer system for any reflector (VISAR) has been used to track a shock moving through a transparent material or to measure when the shock breaks out into vacuum.<sup>4</sup> Although these measurements are very useful for studying the equation of state (EOS) in simulation codes, no information is gained about the profile of material release when the shock breaks through the shell because at this point the optical beam is absorbed near the critical plasma density of the rarefaction wave because of its reflection geometry.

In this research, the first direct measurements of the low-density plasma released from the back side of a laser-driven shell is presented. The low-density plasma (at  $10^{20} \text{ cm}^{-3}$ ) was measured to travel  $\sim 190 \mu\text{m}$  in front of the driven shell with a scale length that increased to a maximum to  $63 \mu\text{m}$  over 3 ns (Fig. 1). These observations are in contrast to hydrodynamic simulations that

show the plasma traveling  $\sim 80 \mu\text{m}$  away from the shell with a steep density gradient that increased to  $15 \mu\text{m}$  (Fig. 2). Further investigation uncovered the sensitivity of the inner shell expansion to the initial (before the shock breakout) CH density profile. By initiating the back side of the shell with a  $10\text{-}\mu\text{m}$  density gradient, release profiles matching those observed in the experiment were obtained. The more-rapid expansion results from enhanced heating of the lower-density material by the shock as it breaks out, causing a higher sound speed, and consequently, a faster post-shock expansion. This early relaxation of the CH shell boundary is consistent with estimations of preheat from x rays emanating from the hot coronal plasma. Implementing an expanded profile on the back side of the DT ice layer in direct-drive ICF implosion simulations shows a reduced convergence leading to an 18% lower areal density and a 17% smaller ion temperature.

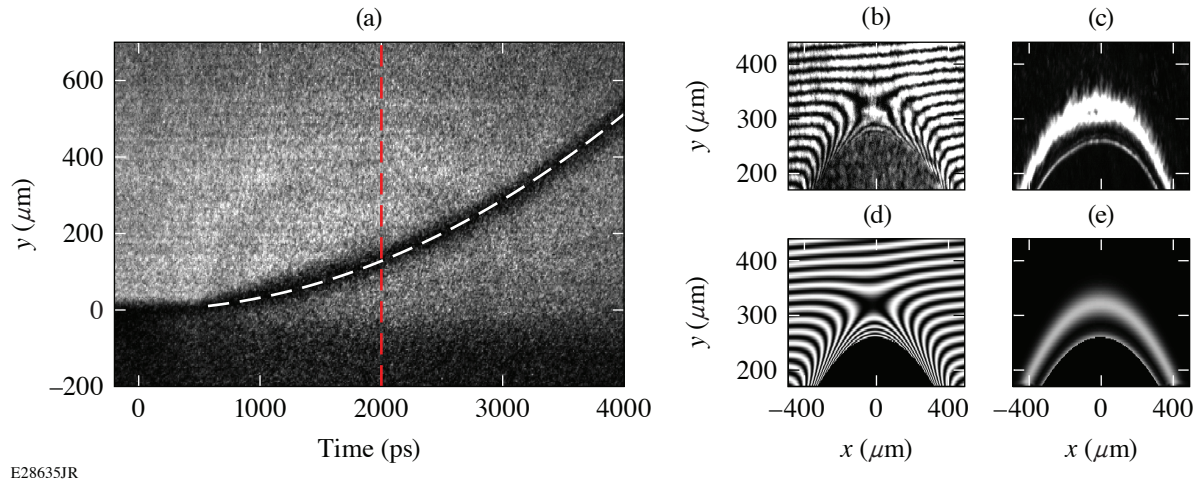


Figure 1

(a) The PJXI diagnostic measured the shell trajectory by tracking absorption of the Al He x rays traveling through the interaction region. The origins of the spatial and temporal axes represent the initial location of the center of the CH shell (spatial) at the beginning of the drive laser pulse (2% of rise, temporal). The  $4\omega$  probe diagnostic measures the density of the released plasma on the back side of the driven shell through (b) interferometry and (d) AFR at 2 ns after the drive. The synthesized response of the (c) interferometry and (e) AFR diagnostics that best match the corresponding measurements at 2 ns. The origin of the y axis corresponds to the position of shock ( $\sim 120 \mu\text{m}$ ) as measured by the radiography (dashed red line).

Figure 1(a) shows a radiograph where the shock is observed breaking out of the back side at  $t = 580 \pm 40$  ps. After this time, the shell trajectory was observed to accelerate at a near-constant acceleration of  $\sim 32 \mu\text{m}/\text{ns}^2$  (dashed white line) across  $\sim 540 \mu\text{m}$  over 4 ns. For this experimental setup, the 1.5-keV x rays provide an optimal peak absorption of  $\sim 70\%$ . The x-ray streak-camera diagnostic had a measured spatial resolution of  $20 \mu\text{m}$ , which was sufficient to track the position of the shell, although not small enough to resolve the expected shell thickness of 5 to  $7 \mu\text{m}$ .

To measure the density profile in the rarefaction wave, an 8-ps-FWHM-duration,  $4\omega$  (263-nm) probe beam was used to generate interferometry<sup>5</sup> [Fig. 1(b)] and angular filter refractometry<sup>6</sup> [AFR, Fig. 1(c)] data. The two diagnostics were used in conjunction to gain confidence in the measured plasma density profiles. The interaction was probed at four times with respect to the beginning of the drive beams (2% of rise): 1 ns, 2 ns (Fig. 1), 3 ns, and 4 ns. For the probe timing of 2 ns, the shell moved  $\sim 120 \mu\text{m}$  at the center of the laser spot [Fig. 1(a)]. Figure 1(b) shows the phase change accrued from propagating through the released plasma. A measurable phase change at the center of the shell is evident for distances greater than  $\sim 290 \mu\text{m}$ ; for positions less than this, the light was refracted outside of the collection optics. Refraction of the probe light from its propagation through this plasma resulted in the observation of two bands [Fig. 1(c)] of constant refraction angle corresponding to  $0.75^\circ$  (outer) and  $3^\circ$  (inner). The images were analyzed by simulating a synthetic interferogram and AFR image using an analytic function for the plasma density and iterating until the images converged to the measurements. A single exponentially decaying profile, with a transverse Gaussian function, was found to be adequate to reproduce the measurements. Other analytic profiles were tested and delivered very similar plasma profiles. The matched synthetic interferogram and AFR image for the 2-ns data are shown in Figs. 1(d) and 1(e), respectively, and correspond to a plasma density profile of  $n_e(x, y, z) = n_0 \exp[-y = L_y] \exp\left\{-\frac{(x^2 + z^2)}{[L_{\text{FWHM}}/2 \ln(2)]}\right\}$ , where  $n_0 = 3.6 \times$

$10^{21} \text{ cm}^{-3}$ ,  $L_y = 38 \text{ }\mu\text{m}$ , and  $L_{\text{FWHM}} = 340 \text{ }\mu\text{m}$ . Note, this profile is accurate only in the low-density region measured by the  $4\omega$  probe and is expected to strongly diverge from the actual plasma profile closer to the driven shell.

Figure 2 shows that the low-density plasma has expanded significantly farther than *LILAC*<sup>7</sup> radiation-hydrodynamic simulations predict. At the earliest measured time (1 ns), the low-density plasma is  $40 \text{ }\mu\text{m}$  in front of the predictions, while the position of the shell is in good agreement. Between 1 ns and 4 ns, the low-density (at  $10^{20} \text{ cm}^{-3}$ ) plasma is measured to have an average velocity of  $\sim 205 \text{ }\mu\text{m/ns}$ , while its scale length expanded from  $10 \text{ }\mu\text{m}$  to  $63 \text{ }\mu\text{m}$ . The average simulated expansion speed of  $145 \text{ }\mu\text{m/ns}$  at  $10^{20} \text{ cm}^{-3}$  was slower than the measurements, and the scale lengths increased from  $2 \text{ }\mu\text{m}$  to  $15 \text{ }\mu\text{m}$ , which are shorter than measured across the entire time span. This discrepancy was largely insensitive to the thermal transport and the EOS models used in the simulations. It was found in simulations that the position of the low-density plasma, as well as its scale length, significantly depends on the mass-density profile at the back surface of the CH shell right before the shock breaks out. The simulation results shown in Fig. 2 used an infinitely sharp boundary on the back side of the CH, as is typical in hydrodynamic simulations. These simulations significantly underestimate the plasma expansion at all times. When the back side of the CH target was relaxed over  $10 \text{ }\mu\text{m}$  (linear increase from zero to solid density prior to the shock breakout), the simulated trajectories are in excellent agreement with the measurements. The increased heating (from 20 eV to  $\sim 100 \text{ eV}$ ) that occurs from the shock propagating through the relaxed back side of the shell, results in a faster expansion and larger scale length than when the standard sharp interface is used. Note the trajectory of the shell was unchanged by this relaxation.

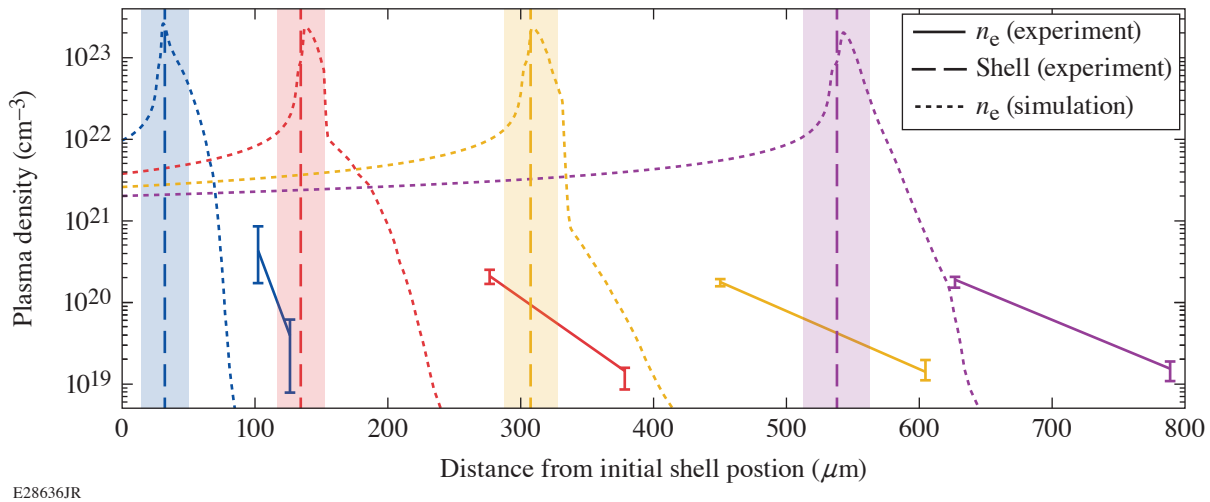


Figure 2

The measured (solid curves) and simulated (dotted curves) plasma density profiles at 1 ns (blue), 2 ns (red), 3 ns (yellow), and 4 ns (purple) are plotted. The vertical dashed lines are the peak shell position as measured by the PJXI diagnostic (with error bars shown by the shaded regions).

In summary, optical probing using interferometry and angular filter refractometry was used to study the material release from the shock breakout at conditions relevant to ICF implosions. It was observed that the position and scale length in the measured density range ( $10^{19}$  to  $10^{20} \text{ cm}^{-3}$ ) of the rarefaction wave strongly depends on the density profile at the back surface of the CH before the shock passes. To match the experimental data, simulations required a relaxation that results in a neutral-density gradient on the inner surface of the CH shell before the shock pass. This lower-density material is strongly heated by the passing shock, which causes it to expand more rapidly and have a longer scale length at later times. Radiation preheat by coronal x rays can cause such a relaxation of the back surface of the CH and formation of the density gradient. Simulations of direct-drive cryogenic implosions that enhanced the inner surface release consistent with these measurements show a significant reduction in target performance, including an 18% reduction in areal density, a 17% reduction in ion temperature, and more than a factor of 2 reduction in the neutron yield.

This material is based upon work supported by the Department of Energy National Nuclear Security Administration under Award Number DE-NA0003856, the University of Rochester, and the New York State Energy Research and Development Authority

1. S. Le Pape *et al.*, Phys. Rev. Lett. **120**, 245003 (2018).
2. D. S. Clark *et al.*, Nucl. Fusion **59**, 032008 (2018).
3. D. T. Michel *et al.*, Rev. Sci. Instrum. **83**, 10E530 (2012).
4. M. A. Barrios *et al.*, Phys. Plasmas **17**, 056307 (2010).
5. A. Howard *et al.*, Rev. Sci. Instrum. **89**, 10B107 (2018).
6. D. Haberberger *et al.*, Phys. Plasmas **21**, 056304 (2014).
7. J. Delettrez, Can. J. Phys. **64**, 932 (1986).

# The Role of Baroclinicity in the Kinetic Energy Budget

A. Lees and H. Aluie

Laboratory for Laser Energetics and Department of Mechanical Engineering, University of Rochester

The role of baroclinicity, which arises from the misalignment of pressure and density gradients, is well known in the vorticity equation, yet its role in the kinetic energy budget has never been obvious. We have shown that baroclinicity appears naturally in the kinetic energy budget after carrying out the appropriate scale decomposition. Strain generation by pressure and density gradients, both barotropic and baroclinic, also results from our analysis. These two processes underlie the recently identified mechanism of “baropycnal work,”<sup>1–3</sup> which can transfer energy across scales in variable density flows. We also provide numerical evidence from high-resolution (i.e.,  $1024 \times 1024 \times 1024$ ) direct numerical simulations (DNS’s) of compressible turbulence (Fig. 1).

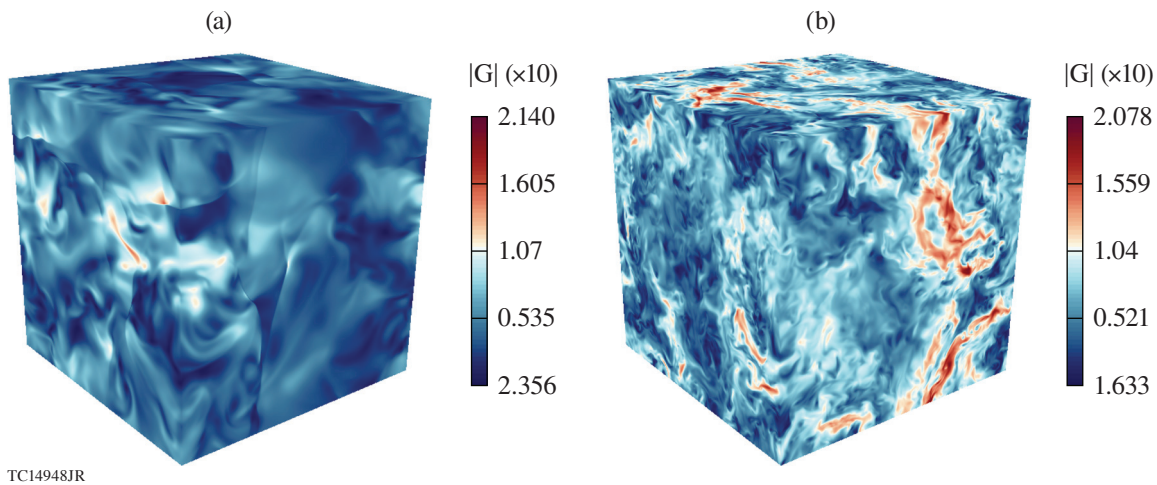


Figure 1  
DNS of turbulent flows at varying levels of compressibility using our DiNuSUR code.

To analyze the dynamics of different scales in a compressible flow, we use the coarse-graining approach. It has proven to be a natural and versatile framework for understanding and modeling scale interactions (e.g., Refs. 1–6) and is closely related to well-established physics techniques, including macroscopic electromagnetism,<sup>7,8</sup> where coarse graining of microscopic charge and current densities coupled with gradient expansions yield the macroscopic polarization  $\mathbf{P}$  and magnetization  $\mathbf{M}$  as well as higher-order multipole contributions. It is also closely related to the renormalization group (RG), especially “real-space RG,”<sup>9,10</sup> where a coarse-grained field is like a “block spin” and coarse-grained equations are analogous to “effective Hamiltonian/action” for the block spins with running coupling constants that depend on the scale parameter  $\ell$ . Our approach is also intimately related to large eddy simulation (LES) in turbulence modeling.<sup>4,11</sup> Equations governing the dynamics of different scales can be derived relatively easily, allowing for a direct analysis of processes at those scales both analytically and using data from simulations or experiments.

For any field  $a(x)$ , a coarse-grained or (low-pass) filtered field, which contains modes at scales  $> \ell$ , is defined in  $n$  dimensions as

$$\bar{\mathbf{a}}_\ell(x) = \int d^n \mathbf{r} G_\ell(\mathbf{r}) \mathbf{a}(\mathbf{x} + \mathbf{r}), \quad (1)$$

where  $G(r)$  is a normalized convolution kernel and  $G_\ell(r) = \ell^{-n} G(r/\ell)$  is a dilated version of the kernel having its main support over a region of diameter  $\ell$ . The scale decomposition above is essentially a partitioning of scales in the system into large ( $> \ell$ ), captured by  $\bar{a}_\ell$ , and small ( $< \ell$ ), captured by the residual  $\tilde{a}_\ell = a - \bar{a}_\ell$ .

The budget for the large-scale kinetic energy can be easily derived<sup>3</sup> from the compressible momentum equation:

$$\partial_t \bar{\rho}_\ell \frac{|\tilde{\mathbf{u}}_\ell|^2}{2} + \nabla \cdot \mathbf{J}_\ell = -\Pi_\ell - \Lambda_\ell + \bar{P}_\ell \nabla \cdot \tilde{\mathbf{u}}_\ell - D_\ell + \epsilon_\ell^{\text{inj}}, \quad (2)$$

where  $J_\ell(x)$  is space transport of large-scale kinetic energy,  $\bar{P}_\ell \nabla \cdot \tilde{\mathbf{u}}_\ell$  is large-scale pressure dilatation,  $D_\ell(x)$  is viscous dissipation acting on scales  $> \ell$ , and  $\epsilon_\ell^{\text{inj}}(x)$  is the energy injected due to external stirring. The  $\Pi_\ell(x)$  and  $\Lambda_\ell(x)$  terms account for the transfer of energy across scale  $\ell$ .

Using the property of scale locality,<sup>1</sup> we have derived a model of  $\Lambda$  that shows how it transfers energy by two processes: barotropic and baroclinic generation of strain  $\mathbf{S}$  from gradients of pressure and density  $\rho$ :

$$(\text{const}) \ell^2 \rho^{-1} \left\{ \left[ \nabla_\rho (\nabla P)^T \right] : \mathbf{S} \right\} \quad (3)$$

and baroclinic generation of vorticity  $\omega$ :

$$(\text{const}) \ell^2 \rho^{-1} (\nabla_\rho \times \nabla P) \cdot \omega. \quad (4)$$

While the role of pressure and density gradients in generating vorticity is well recognized, their role in strain generation has been less emphasized in the literature.

To our knowledge, this is the first direct demonstration of how baroclinicity enters the kinetic energy budget, which arises naturally from our scale decomposition and the identification of  $\Lambda$  as a scale-transfer mechanism (Fig. 2). Baroclinicity is often

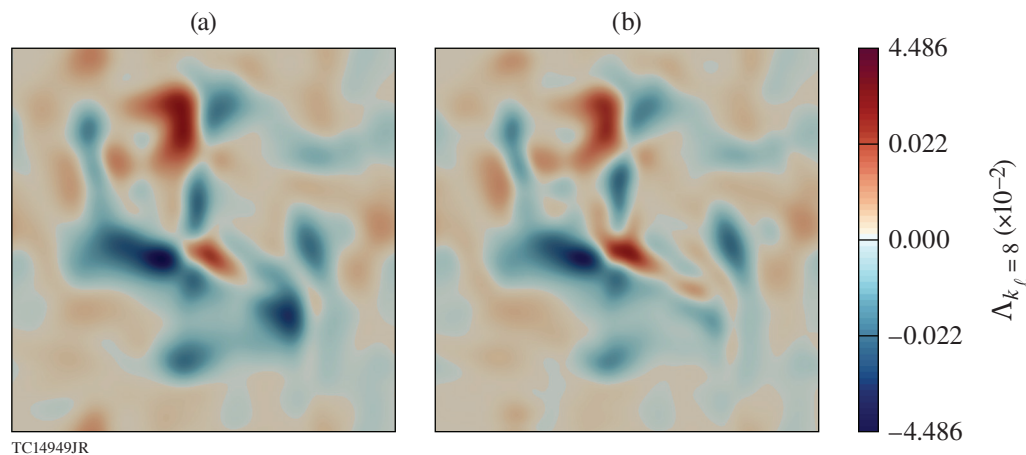


Figure 2  
Visualization of a slice from our 3-D flow of the true  $\Lambda$  and its model that we derived, showing excellent pointwise agreement.

analyzed within the vorticity budget but its role in the energetics has never been obvious. The need for a scale decomposition in order for  $\Lambda$  and, as a result, baroclinic energy transfer to appear in the kinetic energy budget is similar to the scale transfer term  $\Pi$ , which appears in the budget only after decomposing scales due to energy conservation. In the same vein, the appearance of baroclinicity in the vorticity equation can be interpreted as being a consequence of an effective scale decomposition performed by the curl operator  $\nabla \times$ , which is a high-pass filter.

This material is based upon work supported by the Department of Energy National Nuclear Security Administration under Award Number DE-NA0003856, the University of Rochester, and the New York State Energy Research and Development Authority. This research was funded by DOE FES grant number DE-SC0014318. H. Aluie was also supported by NASA grant 80NSSC18K0772 and DOE grant DE-SC0019329. Computing time was provided by the National Energy Research Scientific Computing Center (NERSC) under Contract No. DE-AC02-05CH11231.

1. H. Aluie, *Phys. Rev. Lett.* **106**, 174502 (2011).
2. H. Aluie, S. Li, and H. Li, *Astrophys. J.* **751**, L29 (2012).
3. H. Aluie, *Physica D* **247**, 54 (2013).
4. C. Meneveau and J. Katz, *Ann. Rev. Fluid Mech.* **32**, 1 (2000).
5. G. L. Eyink, *Physica D* **207**, 91 (2005).
6. M. Germano, *J. Fluid Mech.* **238**, 325 (1992).
7. G. Russakoff, *Am. J. Phys.* **38**, 1188 (1970).
8. F. N. H. Robinson, *Macroscopic Electromagnetism*, 1st ed., International Series of Monographs in Natural Philosophy (Pergamon Press, Oxford, 1973).
9. K. G. Wilson, *Rev. Mod. Phys.* **47**, 773 (1975).
10. H. Burkhardt and J. M. J. van Leeuwen, eds. *Real-Space Renormalization*, Topics in Current Physics (Springer-Verlag, Berlin, 1982).
11. A. Leonard, *Adv. Geophys.* **18 (Part A)**, 237 (1975).

# Investigation of Picosecond Thermodynamics in a Laser-Produced Plasma Using Thomson Scattering

A. S. Davies, D. Haberberger, K. Katz, S. Bucht, J. P. Palastro, R. K. Follett, and D. H. Froula

Laboratory for Laser Energetics, University of Rochester

The rapid evolution of electron density and temperature in a laser-produced plasma was measured using collective Thomson scattering. Picosecond time resolution, enabled by a pulse-front-tilt-compensated spectrometer, revealed a transition in the plasma-wave dynamics from an initially cold evolving state to a quasi-stationary equilibrium state. The equilibrium temperature was found to match the generalized heat equation's predicted scaling  $T_e \propto n_e^{2/5}$  and  $T_e \propto I^{1/5}$ . The plasma evolution was compared to Raman gain bandwidth calculations and showed a time-dependent resonance detuning that would limit the transfer efficiency of a Raman plasma amplifier in the linear regime.

Endeavors to engineer plasmas for a number of applications rely critically on plasma conditions. Optimizing plasma devices, including laser amplifiers,<sup>1–5</sup> laser compressors,<sup>6</sup> wave plates,<sup>7,8</sup> polarizers,<sup>9,10</sup> Q plates,<sup>11</sup> particle accelerators,<sup>12,13</sup> photon accelerators,<sup>14</sup> high-order frequency conversion,<sup>15,16</sup> and photon–electron light sources,<sup>17,18</sup> require an accurate knowledge of plasma density and temperature dynamics. Engineering plasmas to create a laser amplifier and compressor is of particular interest because a plasma-based device can avoid the optical damage thresholds that currently limit the maximum intensity of chirped-pulse–amplification systems.<sup>19</sup>

A Raman plasma amplifier seeks to amplify and compress an ultrashort pulse by transferring energy from a long (tens of picoseconds), energetic pump pulse to a short (tens of femtoseconds), intense seed pulse. Raman amplification is a three-wave interaction, in which two counter-propagating laser pulses of different frequencies form a beat wave that drives an electron plasma wave through the ponderomotive force. The plasma wave facilitates the energy transfer from the higher- to the lower-frequency beam.<sup>1</sup> Pulse compression and efficient energy transfer require the pump pulse amplitude to be depleted within the seed pulse duration, known as the  $\pi$ -pulse or nonlinear regime.<sup>6</sup> Depleting the pump pulse amplitude within the duration of the seed requires a rapidly growing and large-amplitude plasma wave that typically forms when the Langmuir frequency is resonant with the beat frequency produced by the pump and seed beams. In the linear regime, the frequency, growth rate, and maximum amplitude of an electron plasma wave are dependent on the instantaneous electron temperature and density. Accurate prediction of the linear growth of the electron plasma wave in a Raman amplifier has been impeded by the lack of measured plasma conditions over this regime.

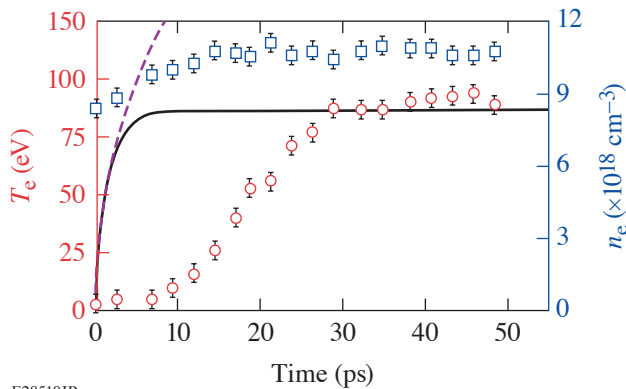
In a laser-produced plasma, the electromagnetic fields generate dynamic plasma conditions that evolve rapidly over the initial 50 ps. This evolution is comparable to pump durations (10 to 20 ps) that have typically been used in plasma devices. Therefore, the plasma conditions vary over the course of these experiments. During the transit of a high-intensity pump pulse through a gas, the photoionized electrons are liberated with minimal kinetic energy, resulting in an initially cold plasma. The energy supplied to the electrons by the electromagnetic field, through inverse bremsstrahlung, causes the temperature to rise rapidly until the collisionality of the plasma reduces the heating rate to a level comparable to the cooling mechanisms. Measurements of these early plasma dynamics on application-relevant time scales have been previously unattainable.

Optical Thomson scattering is a powerful diagnostic that can accurately measure plasma conditions.<sup>20–26</sup> A Thomson-scattering diagnostic can be used to determine localized plasma conditions by calculating the time-resolved spectra from laser light scattered off of plasma waves. The diagnostic requires a spectrometer streak-camera system to provide spectral and temporal resolution of

the scattered spectra. Thomson-scattering diagnostics have not had sufficient temporal resolution to characterize the dynamics of plasma devices. Temporal resolution ( $>50$  ps) for Thomson-scattering systems has been limited by the diagnostic's pulse-front tilt, which is inherent in the angular dispersion of the spectrometer.<sup>27,28</sup> In a conventional system, this pulse-front-tilt-limited resolution is more than an order of magnitude larger than the temporal resolution of present-day streak cameras ( $\sim 1$  ps).

Figure 1 shows measurements of the picosecond evolution of the electron temperature and density in a laser-produced plasma. The measurements were obtained by an ultrafast high-throughput spectrometer<sup>29</sup> that provided unprecedented temporal resolution of the electron plasma waves in the Thomson-scattering spectra.<sup>30</sup> These spectra were used to extract the picosecond evolution of the electron temperature and density. Hydrogen gas was ionized at an intensity near  $10^{14}$  W/cm<sup>2</sup>, where the electron plasma temperature was measured to rise from an initial partially ionized cold ( $\sim 3$ -eV) plasma to a fully ionized plasma at a quasi-steady-state equilibrium temperature over  $\sim 25$  ps. Figure 2 shows that the equilibrium temperatures were found to increase with higher densities and laser intensity. The measured thermodynamics were compared to generalized heat equation calculations of the equilibrium temperature. Measurements agreed with calculated equilibrium temperatures to within 15%, and the plasma condition's dependence on the density and intensity matches the heat equation's predicted scalings  $T_e \propto n_e^{2/5}$  and  $T_e \propto I^{1/5}$ , respectively. The temporal evolution of the temperature measurements was also compared to heat equation calculations (Fig. 1), but the heating rate of the measurements was found to be slower compared to the calculations, suggesting the need to include ionization physics in the model.<sup>31</sup> The time dynamics of the electron plasma waves were compared to calculations of the Raman backscatter dispersion relation of the gain bandwidth. The comparisons show that the picosecond plasma evolution results in a time-dependent resonance detuning in a Raman plasma amplifier. This detuning would significantly limit transfer efficiencies in the linear regime.

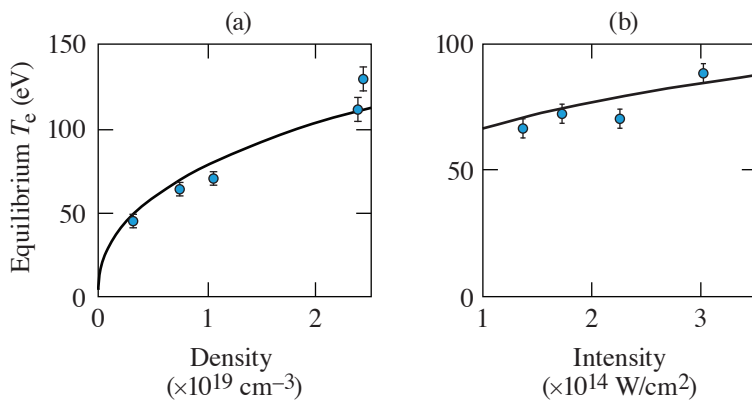
The picosecond thermodynamics presented here are relevant to engineering optimum plasmas for a Raman plasma amplifier. The frequency-matching conditions necessary for laser amplification in the linear regime are dependent on the instantaneous



E28510JR

Figure 1

The measured (red circles, left axis) and calculated (solid black curve) electron temperatures are compared. The measured electron density (blue squares, right axis) is plotted as a function of time. The calculated temperature (dashed purple curve) is plotted as a function of time when the heat conduction and ion-heating terms are dropped from the generalized heat equation.



E28331JR

Figure 2

(a) The measured (circles) and calculated (solid curve) equilibrium temperatures are plotted versus the plasma density for an intensity of  $2.2 \times 10^{14}$  W/cm<sup>2</sup>. (b) The measured (circles) and calculated (solid curve) equilibrium temperatures are plotted versus laser intensity for a density of  $1.0 \times 10^{19}$  cm<sup>-3</sup>.

density and temperature conditions, as indicated by the Langmuir frequency. When accounting for the detuning introduced by the evolving plasma conditions (Fig. 1), the amplification regime is limited to a finite temperature range ( $\sim 60$  eV to  $\sim 120$  eV, when the laser frequencies are chosen to be resonant at the equilibrium temperature). Outside the amplification zone, there will be zero gain due to the temperature detuning. By comparing this amplification zone to the measured temperature evolution shown in Fig. 1, it is apparent that the time dynamics of the electron plasma wave would result in time-dependent resonance detuning in a Raman plasma amplifier. In this example, the amplifier would experience zero gain until after the first 25 ps. If an 8-mm plasma channel was used to match the pump pulse duration, the first 4 mm would be wasted and the maximum possible transfer efficiency would be  $< 50\%$ . This example illustrates the importance of taking the plasma evolution into account when designing a Raman amplification experiment; these results can help guide future endeavors.

This material is based upon work supported by the Department of Energy National Nuclear Security Administration under Award Number DE-NA0003856, the University of Rochester, and the New York State Energy Research and Development Authority.

1. G. Shvets *et al.*, Phys. Rev. Lett. **81**, 4879 (1998).
2. Y. Ping *et al.*, Phys. Rev. Lett. **92**, 175007 (2004).
3. J. Ren *et al.*, Nat. Phys. **3**, 732 (2007).
4. G. Vieux *et al.*, Sci. Rep. **7**, 2399 (2017).
5. J. D. Sadler *et al.*, Phys. Rev. E **95**, 053211 (2017).
6. V. M. Malkin, G. Shvets, and N. J. Fisch, Phys. Rev. Lett. **82**, 4448 (1999).
7. P. Michel *et al.*, Phys. Rev. Lett. **113**, 205001 (2014).
8. D. Turnbull *et al.*, Phys. Rev. Lett. **116**, 205001 (2016).
9. D. J. Stark *et al.*, Phys. Rev. Lett. **115**, 025002 (2015).
10. D. Turnbull *et al.*, Phys. Rev. Lett. **118**, 015001 (2017).
11. K. Qu, Q. Jia, and N. J. Fisch, Phys. Rev. E **96**, 053207 (2017).
12. R. Bingham, Nature **394**, 617 (1998).
13. S. M. Hooker, Nat. Photonics **7**, 775 (2013).
14. S. C. Wilks, J. M. Dawson, and W. M. Mori, Phys. Rev. Lett. **61**, 337 (1988).
15. J. J. Rocca *et al.*, Phys. Rev. Lett. **73**, 2192 (1994); **75**, 1236(E) (1995).
16. A. Butler *et al.*, Phys. Rev. Lett. **91**, 205001 (2003).
17. K. T. Phuoc *et al.*, Nat. Photonics **6**, 308 (2012).
18. N. D. Powers *et al.*, Nat. Photonics **8**, 28 (2014).
19. D. Strickland and G. Mourou, Opt. Commun. **56**, 219 (1985).
20. S. H. Glenzer *et al.*, Phys. Rev. Lett. **82**, 97 (1999).
21. D. S. Montgomery *et al.*, Laser Part. Beams **17**, 349 (1999).
22. J. L. Kline *et al.*, Phys. Rev. Lett. **94**, 175003 (2005).
23. C. Rousseaux *et al.*, Phys. Rev. Lett. **97**, 015001 (2006).
24. D. H. Froula *et al.*, Phys. Rev. Lett. **93**, 035001 (2004).

25. J. S. Ross *et al.*, *Rev. Sci. Instrum.* **81**, 10D523 (2010).
26. R. J. Henchen *et al.*, *Phys. Rev. Lett.* **121**, 125001 (2018).
27. A. Visco *et al.*, *Rev. Sci. Instrum.* **79**, 10F545 (2008).
28. J. Hebling, *Opt. Quantum Electron.* **28**, 1759 (1996).
29. J. Katz *et al.*, *Rev. Sci. Instrum.* **87**, 11E535 (2016).
30. A. S. Davies *et al.*, *Phys. Rev. Lett.* **122**, 155001 (2019).
31. H. P. Le, M. Sherlock, and H. A. Scott, *Phys. Rev. E* **100**, 013202 (2019).

# Measurement and Control of Ionization Waves of Arbitrary Velocity in the Quasi-Far Field

P. Franke,<sup>1,2</sup> D. Turnbull,<sup>1</sup> J. Katz,<sup>1</sup> J. P. Palastro,<sup>1</sup> I. A. Begishev,<sup>1</sup> J. Bromage,<sup>1,3</sup> J. L. Shaw,<sup>1</sup> R. Boni,<sup>1</sup> and D. H. Froula<sup>1,2</sup>

<sup>1</sup>Laboratory for Laser Energetics, University of Rochester

<sup>2</sup>Department of Physics & Astronomy, University of Rochester

<sup>3</sup>Institute of Optics, University of Rochester

Ionization fronts with precisely controlled characteristics could help to overcome fundamental limitations in laser-plasma-based photonics applications by improving phase matching, extending interaction lengths, and facilitating better control of plasma conditions. These capabilities are particularly useful in plasma-based light manipulation processes such as photon acceleration,<sup>1–6</sup> Raman amplification,<sup>7–12</sup> and THz generation<sup>13–15</sup>—processes that could lead to a new generation of exotic, compact, and versatile radiation sources.

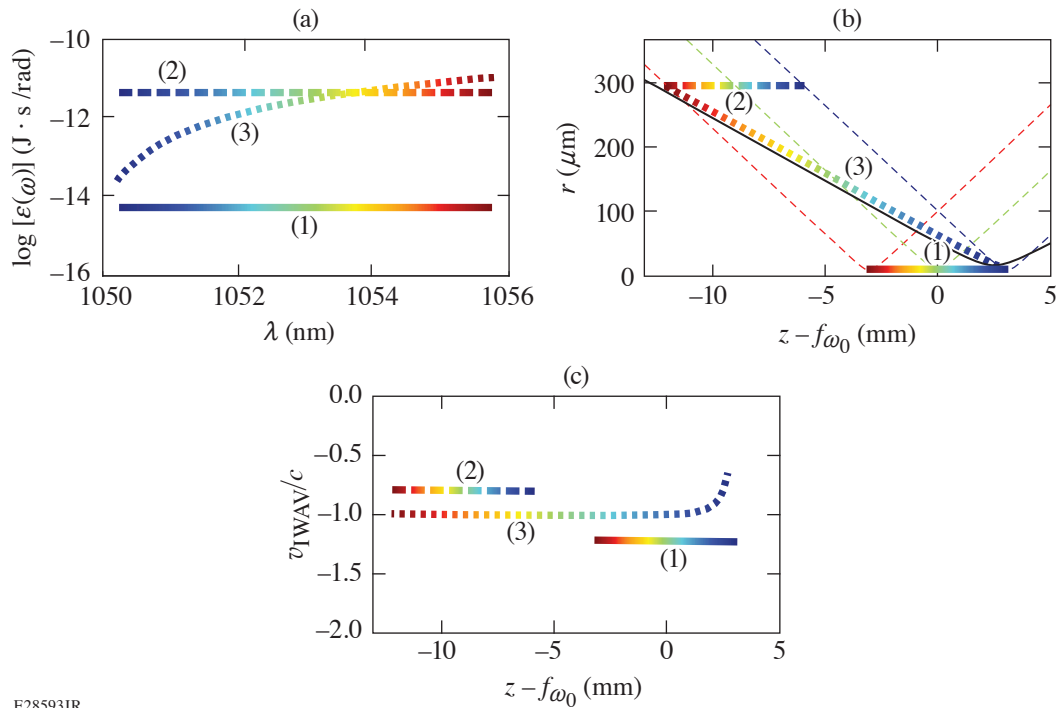
Highly controllable ionization fronts can be driven using a recently developed method called the “flying focus,” in which a chirped laser pulse is focused by a hyperchromatic optic such as a diffractive lens.<sup>16,17</sup> The chromatic aberration causes different frequencies in the laser pulse to come to focus at different positions along the propagation axis. For a fixed focal geometry, the temporal delay between when each frequency reaches its focal position is determined by the chirp, which can be adjusted to cause the point of the maximum laser intensity to move at any velocity over distances that can greatly exceed the Rayleigh length.

When the instantaneous intensity of a flying-focus pulse exceeds the ionization intensity threshold ( $I_i$ ) of a background gas an ionization front is produced that tracks the propagation of an intensity isosurface at  $I_i$  (Ref. 18). These ionization waves of arbitrary velocity (IWAV’s) were experimentally demonstrated to have predictable and easily adjustable velocities equal to the expected flying-focus velocity when driven by a laser pulse with a highly uniform power spectrum in the laser far field.<sup>19</sup>

While modification of the power spectrum was proposed as a means to increase control of IWAV propagation,<sup>18</sup> previous theoretical and experimental investigations were limited to the laser far field and mainly considered flat power spectra, i.e., high-order super-Gaussians. In this parameter regime, all frequencies in the bandwidth have just enough power to ionize near their minimum spot size. Experimental observation of channels formed by IWAV propagation indicated radii  $\sim 10 \mu\text{m}$ , close to the measured far-field laser spot size. Such small-diameter IWAV’s would have limited usefulness in applications because of the difficulty of coupling another beam into the IWAV, the small available cross section for interaction, and strong refraction resulting from the short transverse density scale lengths.

It is possible to increase the diffraction-limited minimum spot size by increasing the  $f$  number so that larger IWAV’s can be driven in the laser far field. It may be experimentally favorable, however, to simply increase the total pulse power so that all wavelengths ionize before they reach their minimum spot size. Operation in this so called quasi-far-field (QFF) regime, where the transverse extent of the laser field is large compared to its diffraction-limited spot size, provides control of the IWAV radius without changing the focusing geometry. Furthermore, it offers the possibility of using nonuniform power spectra to control the dynamic behavior of the IWAV’s. QFF IWAV’s may be the only path forward for applications that require a significant pump intensity to exist behind the ionization front, such as flying-focus-driven plasma Raman amplification.<sup>7,8</sup>

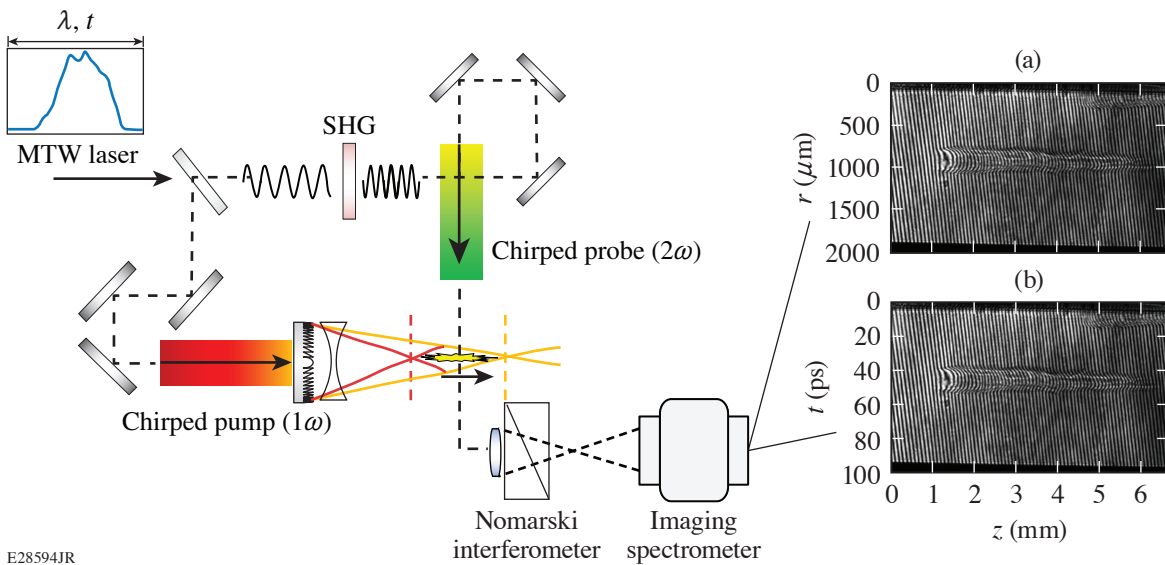
This research presents the first experimental demonstration of IWAV’s in the QFF and develops a new theory to predict their behavior. Figure 1 describes a simple model of IWAV propagation when the flying-focus power spectrum is nonuniform and uses it to develop an intuitive understanding of QFF IWAV’s and demonstrate enhanced control of IWAV characteristics through spectral shaping. Figure 2



E28593JR

Figure 1

(a) Calculations of the IWAV (b) radius and (c) velocity are shown for the spectral energy densities. Cases (1) and (2) show the simple far-field and QFF IWAV propagations, respectively. Case (3) shows that the spectrum can be adjusted to change the IWAV radius and match the  $f$  number of a separate beam [black line in (b)], but still maintain a constant velocity. Case (3) also shows that the IWAV range can be increased beyond the already-extended focal region and that the IWAV can be accelerated through spectral shaping. (b) Single-frequency radii for the edges (blue and red) and center (green) of the bandwidth are shown as single-color dashed lines. (c) Velocities for cases (1) and (2) are shown offset from  $v_{\text{IWAV}} = -c$  by  $\sim 20\%$  for clarity, but all calculations were done for  $v_{\text{IWAV}} = -c$ .



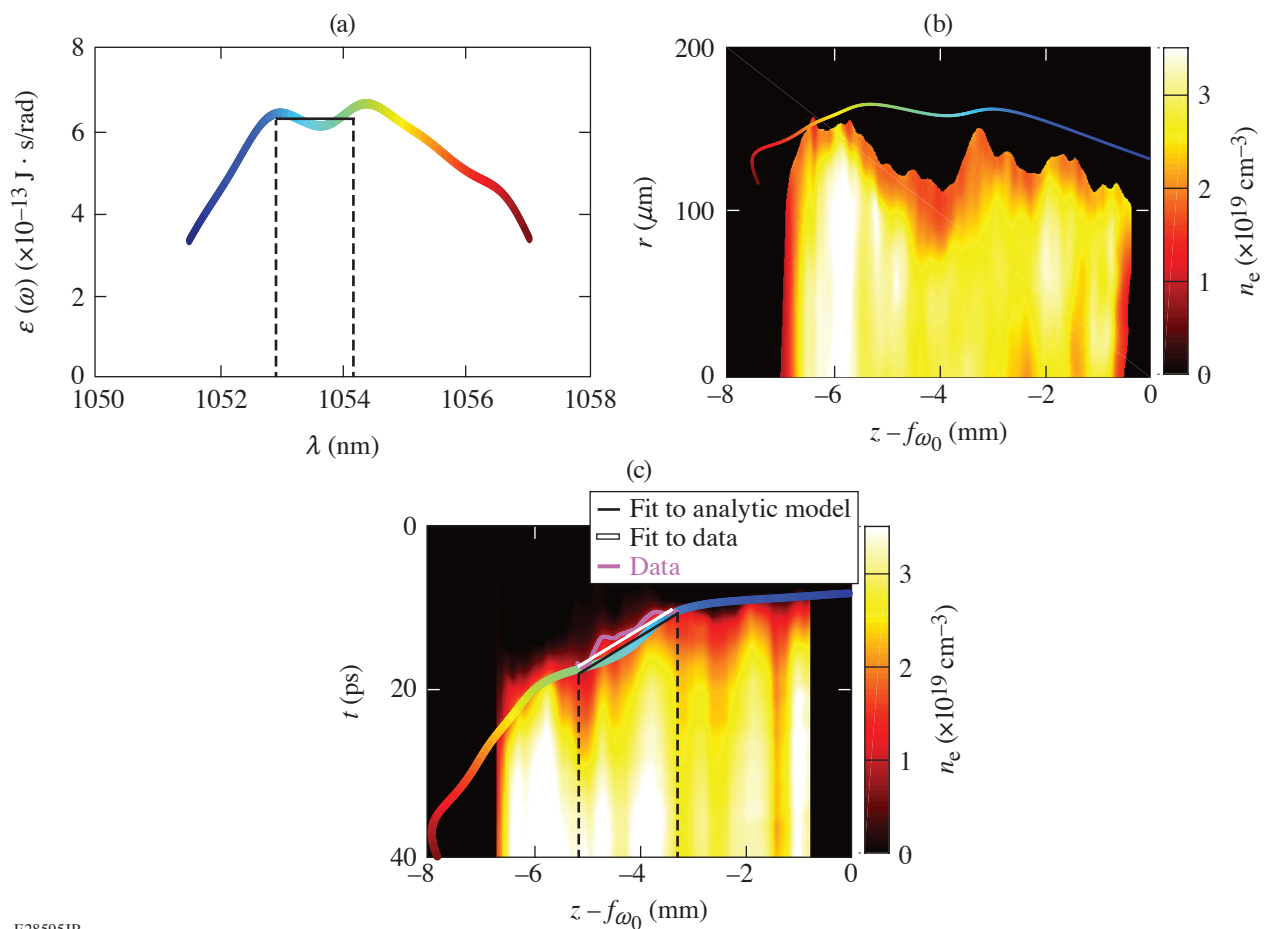
E28594JR

Figure 2

The Multi-Terawatt (MTW) laser was split into a  $1\omega$  pump beam that drove IWAV's in a hydrogen gas jet and a  $2\omega$  probe beam that passed through the interaction region perpendicular to the IWAV propagation with variable timing, allowing (a) conventional 2-D and (b) 1-D spectrally resolved interferograms of the IWAV propagation to be collected. The 2-D data allow for the reconstruction of the electron density as a function of radial and axial distance late in time. The 1-D and 2-D data together allow extraction of the electron density as a function of time and axial distance along the pump beam propagation axis while the IWAV is propagating through the interaction region.

describes an experimental setup that incorporates a novel spectrally resolved interferometry diagnostic that allows for the inference of IWAV characteristics such as velocity, radius, and temporal density scale length. Experimental results are compared to the theory developed in this research (Fig. 3). IWAV's with radii  $\sim 10\times$  larger than previously observed are experimentally demonstrated. The new theory accurately predicts the observed data, even when the direct correspondence to the flying-focus theory is invalid, but obtain consistency between all theories and the data in general. The experimental ionization rates are compared to a computational model described in Ref. 18 and obtain agreement (Fig. 4), which lends experimental validation to recent predictions of the extreme frequency upshifts achievable by co-propagating a witness laser pulse with a flying-focus-driven IWAV.

This material is based upon work supported by the Department of Energy National Nuclear Security Administration under Award Number DE-NA0003856, the Fusion Energy Science under Award Numbers DE-SC0019135, DE-SC0016253, the University of Rochester, and the New York State Energy Research and Development Authority.



E28595JR

Figure 3

(a) The experimental spectral energy density was used to calculate an expected radial profile and trajectory [multicolor curves in (b) and (c), respectively], which are overlaid on the electron density data extracted from 2-D interferometry and spectrally resolved interferometry [color bar in (b) and (c), respectively]. The predicted radial profile and trajectory are in agreement with the data over the entire bandwidth. A “flat” region of the spectrum and the trajectory that corresponds to this part of the spectrum is demarcated by vertical dashed black lines in (a) and (c). In this region, the flying-focus velocity ( $-0.75c$ ), the predicted IWAV velocity ( $-0.73c$ ), and the measured velocity ( $-0.71c$ ) are all in agreement.

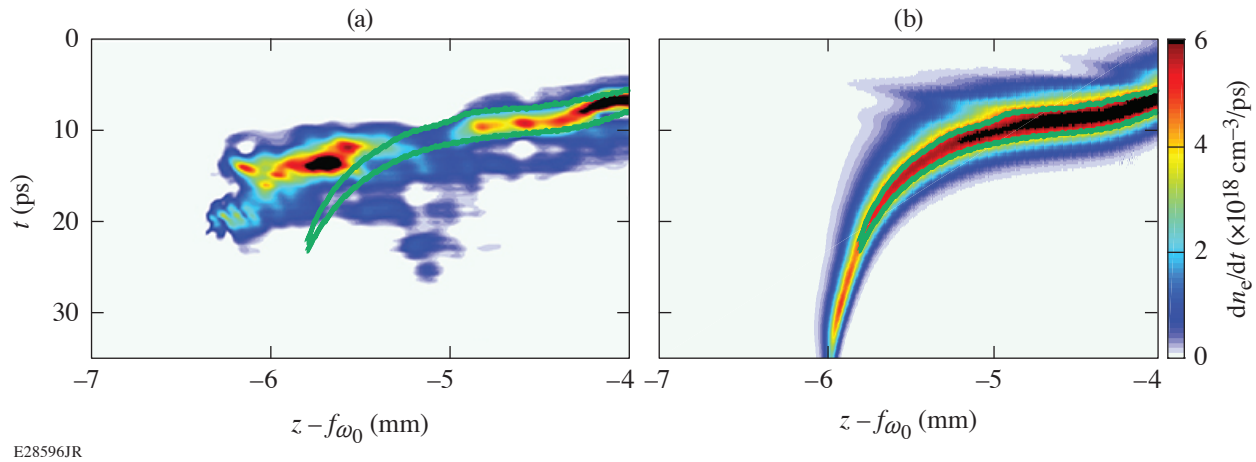


Figure 4

(a) The measured temporal density gradient (ionization rate) has values and a trajectory that are close to those predicted by simulations of ionization as a result of (b) flying-focus pulse propagation. An outline of the simulated data is shown in both (a) and (b) as a green curve.

1. A. Howard *et al.*, "Photon Acceleration in a Flying Focus," to be published in Physical Review Letters.
2. S. C. Wilks *et al.*, Phys. Rev. Lett. **62**, 2600 (1989).
3. J. T. Mendonça, *Theory of Photon Acceleration*, Series in Plasma Physics (Institute of Physics Publishing, Bristol, England, 2001).
4. J. M. Dias *et al.*, Phys. Rev. E **66**, 056406 (2002).
5. N. C. Lopes *et al.*, Europhys. Lett. **66**, 371 (2004).
6. L. Oliveria e Silva and J. T. Mendonca, IEEE Trans. Plasma Sci. **24**, 316 (1996).
7. D. Turnbull *et al.*, Phys. Rev. Lett. **120**, 024801 (2018).
8. D. Turnbull *et al.*, Plasma Phys. Control. Fusion **61**, 014022 (2019).
9. V. M. Malkin, G. Shvets, and N. J. Fisch, Phys. Rev. Lett. **82**, 4448 (1999).
10. V. M. Malkin, G. Shvets, and N. J. Fisch, Phys. Rev. Lett. **84**, 1208 (2000).
11. Y. Ping *et al.*, Phys. Rev. Lett. **92**, 175007 (2004).
12. Y. Ping *et al.*, Phys. Plasmas **16**, 123113 (2009).
13. K. Y. Kim *et al.*, Opt. Express **15**, 4577 (2007).
14. P. Sprangle *et al.*, Phys. Rev. E **69**, 066415 (2004).
15. C. D'Amico *et al.*, Phys. Rev. Lett. **98**, 235002 (2007).
16. D. H. Froula *et al.*, Nat. Photonics **12**, 262 (2018).
17. A. Sainte-Marie, O. Gobert, and F. Quéré, Optica **4**, 1298 (2017).
18. J. P. Palastro *et al.*, Phys. Rev. A **97**, 033835 (2018).
19. D. Turnbull *et al.*, Phys. Rev. Lett. **120**, 225001 (2018).

# Photon Acceleration in a Flying Focus

A. J. Howard, D. Turnbull, A. S. Davies, P. Franke, D. H. Froula, and J. P. Palastro

Laboratory for Laser Energetics, University of Rochester

Theory and simulations demonstrate that the ionization front produced by a flying focus can upshift the frequency of an ultrashort optical pulse to the extreme ultraviolet (XUV) over a centimeter of propagation. An analytic model of the upshift predicts that this scheme could be scaled to a novel tabletop source of spatially coherent x rays.

A growing number of scientific fields rely critically on high-intensity, high-repetition-rate sources of XUV radiation (wavelengths <120 nm). These sources provide high-resolution imaging for high-energy-density physics and nanotechnology; fine-scale material ablation for nanomachining, spectrometry, and photolithography; and ultrafast pump/probe techniques for fundamental studies in atomic and molecular physics. While XUV sources have historically been challenging to produce, methods including nonlinear frequency mixing, high harmonic generation, and XUV lasing or line emission in metal-vapor and noble-gas plasmas have demonstrated promising results. Despite their successes, each of these methods introduces tradeoffs in terms of tunability, spatial coherence, divergence, or efficiency. Photon acceleration offers an alternative method for tunable XUV production that could lessen or even eliminate these tradeoffs.

Photon acceleration refers to the frequency upshift of light in response to a refractive index that decreases in time.<sup>1</sup> In analogy to charged-particle acceleration, the increase in photon energy, i.e., frequency, accompanies an increase in group velocity. In the context of an electromagnetic pulse, the leading phase fronts experience a higher index than adjacent, trailing phase fronts, which manifests as a local phase velocity that increases over the duration of the pulse. The trailing phase front, because of its higher phase velocity, gradually catches up with the leading front, compressing the wave period. In a medium with normal dispersion, the resulting frequency upshift translates to an increase in the local group velocity.

Plasmas, in particular, provide an ideal medium for photon acceleration: the refractive index depends on the density of free electrons, which can be rapidly increased or decreased over time through ionization and recombination or manipulated through electrostatic wave excitation. Specifically, a photon of frequency  $\omega$  in an isotropic plasma experiences a refractive index  $n(\omega = 1 - \omega_p^2 / \omega^2)^{1/2}$ , where  $\omega_p = (e^2 n_e / m \epsilon_0)^{1/2}$  is the plasma frequency,  $n_e$  the free electron density,  $e$  the electron charge,  $m$  the electron mass, and  $\epsilon_0$  the permittivity of free space. An increase in the electron density over time—for example, by ionization—provides a decreasing refractive index that will accelerate the photons of a co-located pulse.

A prototypical scheme for photon acceleration involves propagating a witness pulse in an ionization front triggered by a co-propagating drive pulse. In spite of the impressive frequency shifts (>10 $\times$ ) predicted by theory and simulations,<sup>1</sup> experiments in the optical regime have met with limited success ( $\sim 1.25\times$ ) (Ref. 2) as a result of witness pulse refraction and drive pulse diffraction. While these effects can be remedied by preforming a plasma or pre-shaping a gas to provide a guiding structure, two inherent limitations to the upshift remain. First, the drive pulse, and therefore the ionization front, travels at a subluminal group velocity. As the witness pulse accelerates, it quickly outpaces the ionization front, terminating the interaction. Second, the drive pulse refracts from the plasma it creates, limiting the formation of a continuous ionization front.

Here, we demonstrate, for the first time, a scheme for photon acceleration within a co-propagating ionization front that shifts an optical pulse to the XUV. The scheme utilizes a novel photonic technique known as the flying focus to overcome the aforementioned limitations.<sup>3</sup> An appropriately chirped drive pulse, focused through a chromatic lens, exhibits an intensity peak that counter-propagates at the speed of light in vacuum  $c$  with respect to its group velocity.<sup>4</sup> The peak intensity, in turn, triggers an ionization front traveling at  $c$ , which can continually accelerate the photons of a co-propagating witness pulse. A schematic is displayed in Fig. 1 for the case of a diffractive optic. The peak intensity of the drive pulse travels through the focal region  $z_f = (\Delta\lambda/\lambda_c)f$  at the focal velocity  $v_f = (1 + v_d T/z_f)^{-1} v_d$ , where  $\lambda_c$  is the central wavelength of the drive pulse,  $\Delta\lambda/\lambda_c$  is its fractional bandwidth,  $f$  is the focal length of the diffractive optic at  $\lambda_c$ ,  $v_d$  is the group velocity, and  $T$  is the stretched pulse duration.

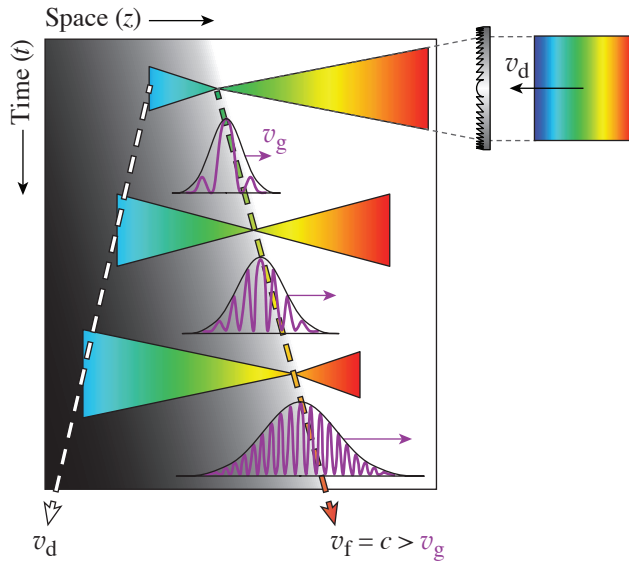


Figure 1

(a) A schematic demonstrating photon acceleration in the ionization front of a flying focus. A negatively chirped drive pulse propagating at its group velocity  $v_d < 0$  forms a focus that counter-propagates at the velocity  $v_f = c$ , triggering an ionization front traveling at  $c$ . The resulting electron density is indicated by the gray shaded area. A witness pulse (purple curves) co-propagates with the ionization front at velocity and continually upshifts in frequency.

TC14718JR

By decoupling the ionization-front velocity from the group velocity of the drive pulse, this scheme removes both of the inherent limitations of the prototypical photon accelerator. Most notably, the interaction distance is no longer limited by outpacing since the accelerated photons can never outpace a luminal (traveling at  $c$ ) ionization front. Second, counter-propagating the drive pulse with respect to the ionization front mitigates ionization refraction since the focus of the drive pulse encounters only the un-ionized medium.

Figure 2 demonstrates that photon acceleration in the ionization front formed by the flying focus can upshift the frequency of an 87-fs witness pulse from the optical ( $\lambda = 400$  nm) to the XUV ( $\lambda = 91$  nm). The figure shows four snapshots from a photon kinetics simulation in the moving frame  $\xi = ct - z$ , where  $t$  is the time elapsed after injecting the witness pulse. The photons of the witness pulse enter the ionization front in Fig. 2(a), each with an initial vacuum wavelength of 400 nm. The photons continually upshift in frequency as they co-propagate with a temporal gradient in electron density as seen in Figs. 2(b) and 2(c). After  $\sim 1$  cm, the photons—now upshifted to a minimum vacuum wavelength of 91 nm—approach the end of the focal region and encounter a decelerating ionization front, terminating their upshift.

Assuming an electron density profile with a constant gradient moving at  $c$ , the vacuum wavelength evolves according to  $\lambda(z) = (1 + \omega_{p0}^2 z / \omega_0^2 L_T)^{-1/2} \lambda_0$ , where  $\lambda_0$  is the initial wavelength of a photon in the witness pulse,  $\omega_0 = 2\pi c/\lambda_0$ , and  $\omega_{p0}$  is the value of the plasma frequency at  $\xi = L_T$ . This analytic model is in good agreement with the simulation and reveals several paths to shorter wavelengths. The interaction length can be extended by increasing the bandwidth of the drive pulse or the focal length; the peak electron density can be increased by propagating within higher-density media, such as solid density targets ( $\sim 10^{22}$  cm<sup>-3</sup>); and the scale length can be decreased by increasing the intensity of the drive pulse or decreasing the effective duration of the

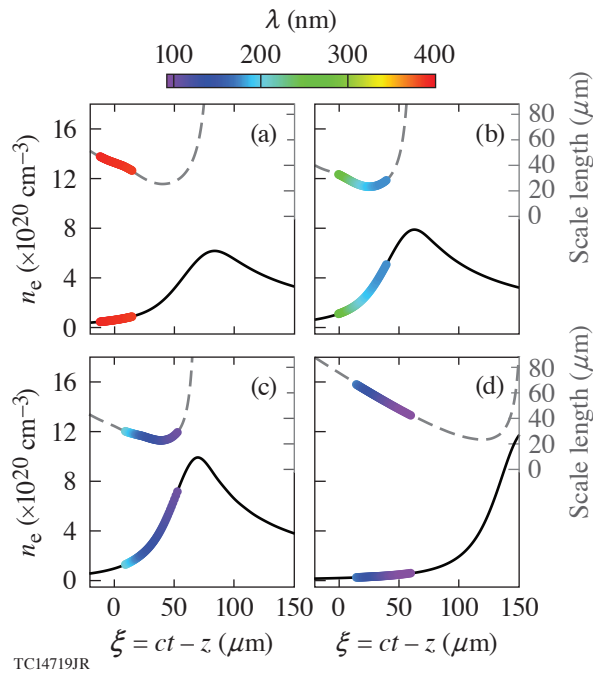


Figure 2

[(a)–(d)] A series of snapshots of an 87-fs witness pulse with an initial wavelength  $\lambda = 400$  nm co-propagating with a temporal gradient in the electron density. The snapshots are taken at propagation distances of (a) 0.10, (b) 0.30, (c) 0.85, and (d) 1.05 cm and plotted in the moving frame  $\xi$ . The pulse is modeled by photons initially spaced evenly in time over 87 fs. Each photon is represented by a circle colored to correspond to its vacuum wavelength (color bar). The electron density and scale length  $L = n_e / \partial_\xi n_e$  are shown as solid black and dashed gray lines, respectively.

flying focus intensity peak such that ionization occurs more rapidly. As a result, this scheme represents a promising method for the production of spatially coherent x rays at the tabletop scale.

This material is based upon the work supported by the U.S. Department of Energy Office of Fusion Energy Sciences under Contract Nos. DE-SC0016253 and DESC0019135, the Department of Energy National Nuclear Security Administration under Award No. DE-NA0003856, the University of Rochester, and the New York State Energy Research and Development Authority.

1. S. C. Wilks *et al.*, Phys. Rev. Lett. **62**, 2600 (1989).
2. J. M. Dias *et al.*, Phys. Rev. Lett. **78**, 4773 (1997).
3. D. H. Froula *et al.*, Nat. Photonics **12**, 262 (2018).
4. J. P. Palastro *et al.*, Phys. Rev. A **97**, 033835 (2018).

# Evolution of the Electron Distribution Function in the Presence of Inverse Bremsstrahlung Heating and Collisional Ionization

A. L. Milder,<sup>1,2</sup> H. P. Le,<sup>3</sup> M. Sherlock,<sup>3</sup> P. Franke,<sup>1,2</sup> J. Katz,<sup>1</sup> S. T. Ivancic,<sup>1</sup> J. L. Shaw,<sup>1</sup> J. P. Palastro,<sup>1</sup> A. M. Hansen,<sup>1,2</sup>  
I. A. Begishev,<sup>1</sup> W. Rozmus,<sup>4</sup> and D. H. Froula<sup>1,2</sup>

<sup>1</sup>Laboratory for Laser Energetics, University of Rochester  
<sup>2</sup>Department of Physics & Astronomy, University of Rochester  
<sup>3</sup>Lawrence Livermore National Laboratory

The picosecond evolution of non-Maxwellian electron distribution functions was measured in plasmas generated by the Multi-Terawatt laser using collective electron plasma wave Thomson scattering. During the laser heating, the distribution was measured to be approximately super-Gaussian due to inverse bremsstrahlung heating. After the heating laser turned off, collisional ionization caused further modification to the distribution function while increasing electron density and decreasing temperature.

Electron velocity distributions govern most fundamental processes in plasma physics. Models of these processes often take the electron distribution function to be Maxwellian or impose small deviations from a Maxwellian. While this assumption can lead to significant errors, any significant deviation from a Maxwellian requires a kinetic understanding, which is often prohibitively challenging. As computational resources improve and experiments begin to isolate kinetic effects an understanding of non-Maxwellian electron distribution functions is becoming more tractable.

In laser-produced plasmas, inverse bremsstrahlung heating,<sup>1–3</sup> thermal transport,<sup>4,5</sup> laser–plasma instabilities,<sup>6</sup> and ionization recombination<sup>7</sup> all provide competing mechanisms that govern the shape of the electron distribution function. A recent computational study has shown the impact of atomic kinetics on inverse bremsstrahlung heating and nonlocal thermal transport, through modifications of the electron distribution function.<sup>7</sup> In a separate study, non-Maxwellian electron distribution functions driven by thermal transport were shown to modify Landau damping of electron plasma waves and enhance their corresponding instabilities.<sup>5</sup> Furthermore, most atomic physics models used to calculate x-ray emission for plasma characterization are built assuming a Maxwellian electron distribution function and deviation from a Maxwellian modifies these calculations.<sup>2</sup>

Although there have been numerous computational studies of kinetic effects in hydrodynamics over the last 40 years,<sup>8</sup> experiments have been challenged to isolate changes to the electron distribution function. In the 1990s, microwaves were used in low-temperature ( $\sim 1$  eV), low-density ( $< 10^{17}$  cm<sup>-3</sup>) plasmas to investigate changes to the electron distribution function introduced by inverse bremsstrahlung heating.<sup>9</sup> Later in the decade, initial studies in laser plasmas suggested the existence of non-Maxwellian electron distribution functions using Thomson scattering.<sup>10</sup> More recently, Thomson-scattering experiments were able to show the effect of nonlocal thermal transport on electron distribution function.<sup>4</sup>

This research presents the first measurements of the interplay between inverse bremsstrahlung heating and ionization kinetics on the electron distribution function.<sup>11</sup> An ultrafast Thomson-scattering system was used to collect the electron plasma wave spectrum, which enabled the picosecond evolution of the non-Maxwellian electron distribution function to be measured in a laser-produced plasma (Fig. 1). The preferential heating of the slow electrons by the laser beam with an intensity of  $2.5 \times 10^{14}$  W/cm<sup>2</sup>, coupled with atomic kinetics, resulted in a non-Maxwellian electron distribution function. The shape of the electron distribution function, 60 ps into the plasma formation, was measured to be approximately a super-Gaussian of the order of 3.4. After the laser turned off, the electron density continued to increase by 15% over the next 40 ps ( $\sim 25$  electron–ion collision times) due to collisional ionization.

Over this time, the electron temperature decreased from 400 eV to 300 eV [Fig. 1(c)], which is consistent with the energy required for ionization to increase the density [Fig. 1(d)]. To determine the electron distribution functions consistent with the measured Thomson-scattered spectra in this rapidly evolving plasma, Vlasov–Fokker–Planck simulations using the code K2 (Ref. 12), which included both laser heating and ionization, were required. Laser heating was found to have the largest effect on the shape of the distribution function, while atomic kinetics provided a smaller effect and allowed matching of the evolution of plasma conditions.

Figures 1(c) and 1(d) show that it is necessary to include ionization in the K2 calculations in order to match the measured plasma conditions. Including ionization also improved agreement with the Thomson-scattering spectra by altering the electron distribution function. While Fig. 1(b) shows the need for non-Maxwellian distributions driven by inverse bremsstrahlung heating to reproduce the spectra, the electron density and temperature [Figs. 1(c) and 1(d)] reveal the need to include an atomic physics model. In simulations without ionization, it is possible to alter the initial plasma conditions to achieve better agreement with the temperature, but this results in distribution functions that generate spectra with poor agreement with the measured Thomson-scattering spectra.

To determine the impact of ionization on the electron distribution function, an atomic physics model was coupled to K2. An inelastic collisional operator, sometimes called a Boltzmann operator, was used to model the changes to the distribution resulting from all atomic processes. The time evolution of the atomic states was determined through a set of coupled rate equations. The collisional rates that enter the rate matrix were obtained from direct integration of the actual distribution. The atomic data (energy levels and cross sections) were constructed based on a screened hydrogenic model using the code Cretin.<sup>13</sup> While the model used for these simulations includes different types of collisional and radiative processes (both bound–bound and bound–free), collisional ionization was identified as the main atomic process affecting the distribution function.<sup>7</sup> The simulations were performed using the experimental laser conditions. Simulations performed without the atomic physics model used a preionized plasma with an electron density of  $2.2 \times 10^{19} \text{ cm}^{-3}$  (corresponding to an average ionization state of 9.1) and an electron temperature of 10 eV. When using the atomic physics model, ionization was self-consistently included and the simulations were initialized with a neutral density of  $2.4 \times 10^{18} \text{ cm}^{-3}$ .

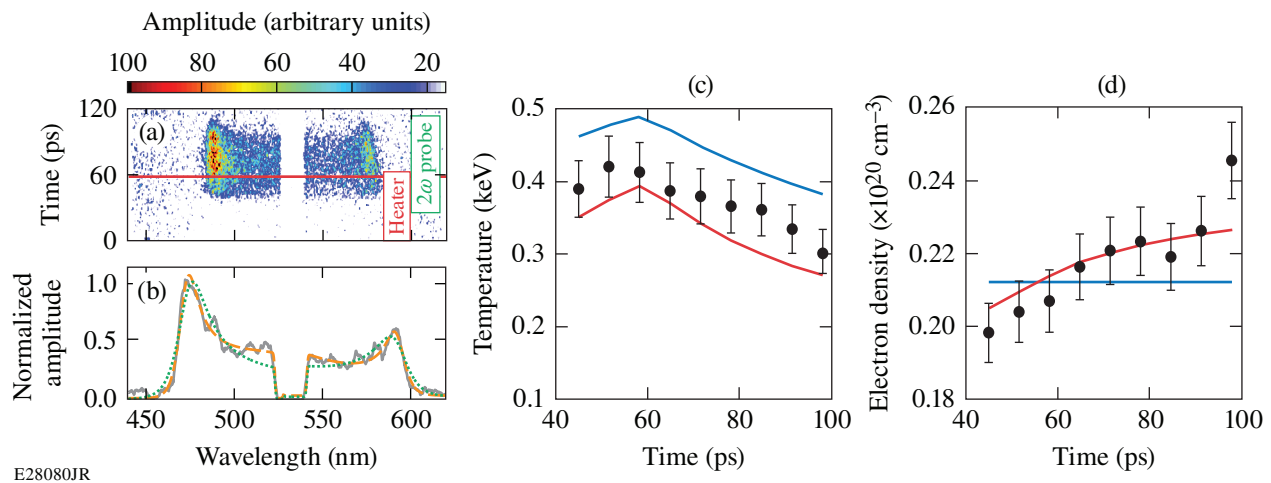


Figure 1

(a) Thomson-scattering spectrum measured from a plasma heated by an intensity of  $2.5 \times 10^{14} \text{ W/cm}^2$ . The heater beam begins at  $t = 0 \text{ ps}$  and the probe beam at  $t = 40 \text{ ps}$  (inset). (b) The measured spectrum at 58 ps (solid gray curve) plotted with a spectrum calculated using Maxwellian (dotted green curve) and non-Maxwellian (dashed orange curve) electron distribution functions. The best-fit spectra determined  $T_e = 428 \text{ eV}$ ,  $n_e = 2.12 \times 10^{19} \text{ cm}^{-3}$ , and  $m = 2$  (Maxwellian); and  $T_e = 412 \text{ eV}$ ,  $n_e = 2.13 \times 10^{19} \text{ cm}^{-3}$ , and  $m = 3.1$  (non-Maxwellian). (c) Temperature and (d) density at nine times through the measurement are shown as solid black circles compared to K2 simulation results. The uncertainty, shown as black error bars, in the measured temperature (c) and density (d) results from repeated fitting within the noise on the spectra. The results of a K2 simulation without atomic kinetics are shown as a solid blue line. The results of a K2 simulation with atomic physics are shown as red curves.

This material is based upon work supported by the Department of Energy National Nuclear Security Administration under Award Number DE-NA0003856, the University of Rochester, and the New York State Energy Research and Development Authority.

1. A. B. Langdon, Phys. Rev. Lett. **44**, 575 (1980).
2. J. P. Matte *et al.*, Plasma Phys. Control. Fusion **30**, 1665 (1988).
3. E. Fourkal *et al.*, Phys. Plasmas **8**, 550 (2001).
4. R. J. Henchen *et al.*, Phys. Rev. Lett. **121**, 125001 (2018).
5. W. Rozmus *et al.*, Phys. Plasma **23**, 012707 (2016).
6. L. Yin *et al.*, Phys. Rev. Lett. **99**, 265004 (2007).
7. H. P. Le, M. Sherlock, and H. A. Scott, Phys. Rev. E **100**, 013202 (2019).
8. H. G. Rinderknecht *et al.*, Plasma Phys. Control. Fusion **60**, 064001 (2018).
9. J. M. Liu *et al.*, Phys. Rev. Lett. **72**, 2717 (1994).
10. S. H. Glenzer *et al.*, Phys. Plasmas **6**, 2117 (1999).
11. A. L. Milder *et al.*, "Evolution of the Electron Distribution in the Presence of Inverse Bremsstrahlung Heating and Collisional Ionization," submitted to Physical Review Letters.
12. M. Sherlock, J. P. Brodrick, and C. P. Ridgers, Phys. Plasmas **24**, 082706 (2017).
13. H. A. Scott, J. Quant. Spectrosc. Radiat. Transf. **71**, 689 (2001).

# Crystalline Phase Transitions and Vibrational Spectra of Silicon up to Multi-TPa Pressures

R. Paul,<sup>1,2</sup> S. X. Hu,<sup>1</sup> and V. V. Karasiev<sup>1</sup>

<sup>1</sup>Laboratory for Laser Energetics, University of Rochester

<sup>2</sup>Department of Mechanical Engineering, University of Rochester

This article presents the *first-principles* construction of a high pressure–temperature ( $P$ – $T$ ) phase diagram of Si up to 4 TPa and 26,000 K, which revealed new stable phases at these multi-TPa conditions. The methodology employed in this work was a combination of different first-principles approaches centered on the use of Mermin’s extension of Kohn–Sham density functional theory (DFT)<sup>1,2</sup> and *ab initio* lattice dynamics of perfect crystals.<sup>3</sup>

The upper bound of the solid-state phase diagram was established using quantum molecular dynamics (QMD) simulations, within the Born–Oppenheimer approximation, with a canonical ensemble to determine the melting points. VASP<sup>4</sup> was used for these calculations, with the temperature being controlled via a Nosé–Hoover thermostat. Instead of using Monkhorst–Pack  $k$  mesh, we resorted to the use of a single special  $k$  point (1/4, 1/4, 1/4) for sampling the Brillouin zone (1BZ). As with all such finite-temperature computations involving electronic structure theory and lattice dynamics, however, the main challenge is the accurate determination of the effects of anharmonicity (AH) beyond the quasiharmonic (QH) approximation of phonon dynamics for the solid state, which is the principal emphasis of this work.

The anharmonic solid-state ionic-thermal contribution  $F_{\text{AH}}$ , for an optimal axial ratio  $\gamma_T$  at a given specific volume and temperature ( $V, T$ ), was evaluated by breaking it up into two separate components and performing thermodynamic integration, with  $T$  being the ionic temperature. The first component tracks the change in Helmholtz free energy, while moving along an isochore, from  $T = 0$  K to some finite temperature keeping the cold-curve axial ratio  $\gamma_0$  constant, which is obtained from statistically averaging internal energy  $U(T)$  from QMD and QH phonon calculations. The second term tracks the free energy change when the axial ratio is changed from  $\gamma_0$  to  $\gamma_T$  at that temperature, from the anisotropic stress tensor of the ensemble. These terms are shown in Eqs. (1) and (2):

$$\left\langle F_{\text{AH}}(V, T; \gamma = \gamma_0) \right\rangle_V = -T \int \frac{\left\langle U(T) \right\rangle_{\text{QMD}} - \left[ U(T)_{\text{QH}} - \frac{3}{2} N_a k_B T \right]}{T^2} \Big|_V dT, \quad (1)$$

$$F_{\text{AH}}(V, T; \gamma_0 \longrightarrow \gamma_T) = - \left( \frac{2V}{3\gamma_T} \right)^2 \frac{\left\langle \sigma_{\text{total}}^{\text{anisotropic}}(T) \right\rangle \left\langle \sigma_{\text{AH}}^{\text{anisotropic}}(T) \right\rangle}{\frac{\partial^2}{\partial \gamma^2} F_{\text{QH}}(T) \Big|_{\gamma_0}}. \quad (2)$$

The phase diagram (Fig. 1) shows the existence of high-pressure body-centered cubic (bcc) and simple cubic (sc) phases beyond 2.8 TPa, as well as a pocket of double hexagonal close-packed (dhcp) in the low-pressure region. The lower-symmetry orthorhombic phases of Cmce and Imma can be accurately determined only when the anharmonicity is included. The compari-

son to experimental results demonstrates the absolute necessity of incorporating the said effects. Similarly, the correct slope of the principal Hugoniot can be determined only when the anharmonic contribution to the Helmholtz free energy is included. The method employed in this summary presents an approach developed for the accurate construction of first-principles equation of state, phase diagrams, or deriving any property that depends on thermodynamic state variables. A remarkable observation is the increasing localization of the electron density in the face-centered cubic (fcc) phase with increasing pressure from  $\sim 100$  GPa to  $\sim 2.8$  TPa, leading to a dip in the electronic density of states and formation of interstitial blobs of electrons; although the dip never develops to a band gap as seen in electrides.

Supplementing the structural calculations, second- and third-order interatomic force constants were evaluated, using a combination of density functional perturbation theory (DFPT)<sup>4</sup> and the power spectrum constructed from phonon eigenvector-projected atomic velocities, to compute the phonon vibration modes and linewidths, respectively. This allowed for an elaborate analysis of the Raman and infrared spectra for all of the structures of silicon identified along the 500-K isotherm.

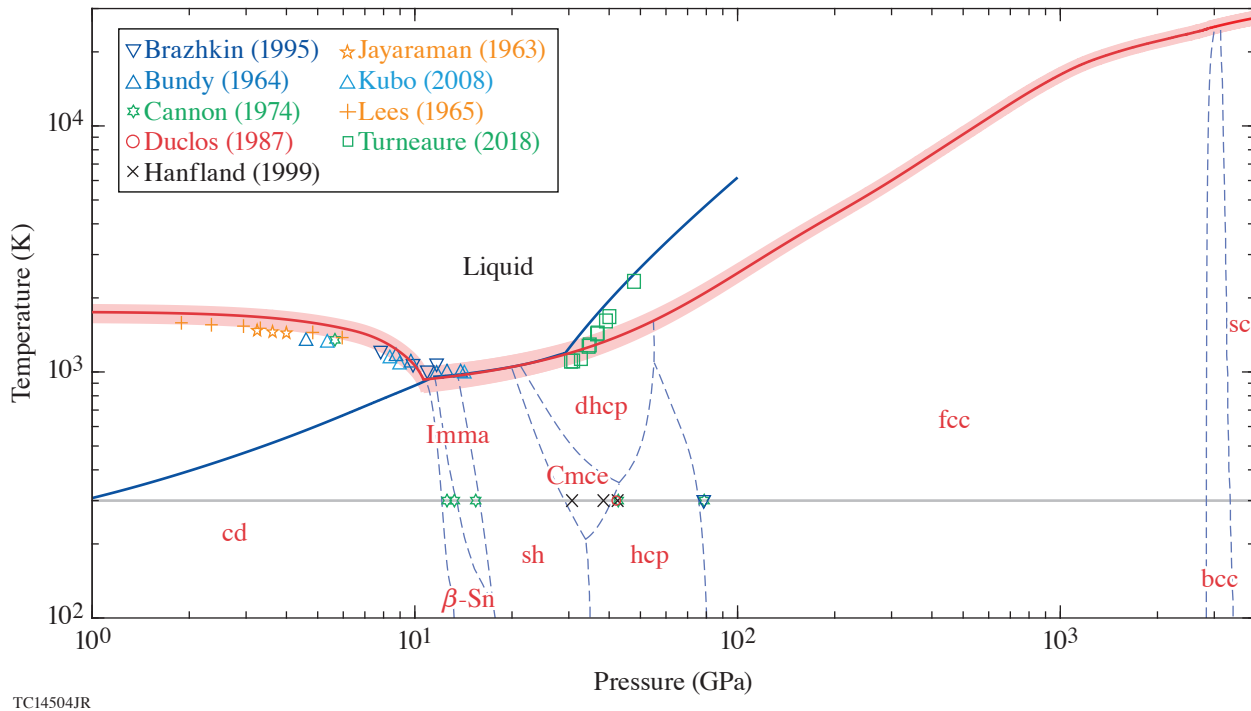


Figure 1

Pressure-temperature ( $P$ - $T$ ) phase diagram of silicon predicted using first-principles methodology. Here, the gray horizontal line represents the 300-K isotherm, whereas the solid blue line represents the principal shock Hugoniot. The discrete data points, which are also labeled in the legend, correspond to experimentally observed phase transition points.

This material is based upon work supported by the Department of Energy National Nuclear Security Administration under Award Number DE-NA0003856, the University of Rochester, and the New York State Energy Research and Development Authority.

1. W. Kohn and L. J. Sham, Phys. Rev. **140**, A1133 (1965).
2. A. Togo, F. Oba, and I. Tanaka, Phys. Rev. B **78**, 134106 (2008).
3. G. Kresse and J. Hafner, Phys. Rev. B **47**, 558 (1993); **49**, 14,251 (1994); G. Kresse and J. Furthmüller, Comput. Mater. Sci. **6**, 15 (1996); Phys. Rev. B **54**, 11,169 (1996).
4. S. Baroni *et al.*, Rev. Mod. Phys. **73**, 515 (2001).

# Inferred UV Fluence Focal-Spot Profiles from Soft X-Ray Pinhole Camera Measurements on OMEGA

W. Theobald, C. Sorce, W. R. Donaldson, R. Epstein, R. L. Keck, C. Kellogg, T. J. Kessler, J. Kwiatkowski, F. J. Marshall, S. Sampat, W. Seka, R. C. Shah, A. Shvydky, C. Stoeckl, L. J. Waxer, and S. P. Regan

Laboratory for Laser Energetics, University of Rochester

Laser-direct-drive inertial confinement fusion (LDD-ICF) implosions with cryogenically layered deuterium–tritium (DT) targets on OMEGA have produced hot-spot pressures  $>50$  Gbar (Refs. 1 and 2), which is about half of the pressure required to achieve ignition conditions. Over the next several years the goal is to demonstrate an ignition-relevant hot-spot pressure of  $\sim 100$  Gbar on OMEGA. The 100-Gbar Project includes improvements to the OMEGA Laser System, diagnostics, targets, and modeling, which will lead to a better understanding of the LDD-ICF physics. This requires a careful monitoring of each beam's intensity at full laser energy at the target plane, which is currently not possible, and is indirectly inferred from measurements outside the target chamber of the beam energy, the laser power, and the spot size. To characterize the focal spot of UV laser beams on target at full energy, a method was developed to image the soft x-ray emission from laser-irradiated Au planar foils. A pinhole camera with a back-thinned charge-coupled-device (CCD) detector and filtration with thin Be and Al foil filters provides images of the x-ray emission at photon energies  $<2$  keV. This method requires a careful measurement of the relation between the applied UV fluence and the x-ray signal, which can be described by a power-law dependence. The measured exponent  $\gamma \sim 2$  provides a dynamic range of  $\sim 30$  for the inferred UV fluence. UV fluence profiles of selected beams were measured for 100-ps and 1-ns laser pulses and compared to directly measured profiles from an UV equivalent-target-plane (UVETP) diagnostic. The inferred spot size and super-Gaussian order from the x-ray technique agree within several percent with the values acquired by direct UV measurements. In an analogy to the UVETP technique, the method is called the x-ray target-plane (XTP) method, which is performed at full laser power inside the target chamber. UV fluence profiles were inferred for up to 11 beams equipped with SG5-850 distributed phase plates (DPP's) and were compared to directly measured UV profiles from the UVETP diagnostic for 4 of the 11 beams. Good agreement between the XTP and UVETP measurements was obtained, indicating that nonlinear optical effects from the transport in air and in the optics at the target chamber wall are likely negligible.

The experimental setup is depicted in Fig. 1(a). An OMEGA UV beam propagates from the left to the right side, passes through a distributed polarization rotator and reaches a fused-silica wedge—uncoated on the front and AR coated on the back—that picks up a 4% reflection of the full beam, which is then sent to the UVETP diagnostic. The main beam is then directed over a distance of about 18 m in air and passes through a DPP and a lens that focuses the beam onto a flat foil inside the target chamber. A similar DPP is placed in the UVETP diagnostic directly in front of an OMEGA focusing lens, mimicking the target/beam configuration. The beam is brought through focus in a vacuum tube, which is not shown in the simplified schematic; outside the tube, the expanding beam is picked up by another lens. The beam is down-collimated and attenuated, and a magnified image of the focus is produced on a CCD camera. The flat-foil target was a  $20\text{-}\mu\text{m}$ -thick Si wafer with an area of  $6 \times 6 \text{ mm}^2$  that was coated with a 500-nm layer of Au. The target normal was aligned along the axis of an opposing port with a ten-inch manipulator (TIM). Up to five beams were focused simultaneously onto the target such that the laser spots were well separated. A pinhole camera loaded into the TIM imaged the x-ray emission with a magnification of 5.16 onto a back-thinned CCD camera.

Figure 1(b) shows example data of the laser spot of Beam 56 from XTP and compares it to Fig. 1(c), the directly measured spot from UVETP. For a quantitative comparison of the fluence profiles, both images were fitted with an elliptical 2-D super-Gaussian function given by

$$F(x, y) = F_0 \exp \left\{ - \left[ \left( \frac{x - x_0}{a} \right)^2 + \left( \frac{y - y_0}{b} \right)^2 \right]^{n_{SG}/2} \right\} + \text{back}, \quad (1)$$

where  $x_0, y_0$  are the coordinates of the beam center,  $n_{SG}$  is the order of the super-Gaussian function, “back” is a constant background, and  $a$  and  $b$  are the minor and major axes of the ellipse, respectively. The fitting is performed over an area of  $\sim 1.6 \times 1.6 \text{ mm}^2$  for both the UVETP and the XTP methods. The minimum signal included in the fit is  $\sim 0.2\%$  of the peak signal for UVETP and  $\sim 2\%$  of the peak signal for XTP. The spot radius is defined as the arithmetic mean of  $a$  and  $b$ :

$$R_{1/e} = \sqrt{a \cdot b}, \quad (2)$$

which describes the average radius where the fluence is at the  $1/e$  value of the peak fluence  $F_0$ . The two main parameters that are used to compare the fluence profiles are  $R_{1/e}$  and  $n_{SG}$ . Figure 1(d) shows the result of the fitting process to the XTP image, while the residual (data minus fit) is shown in Fig. 1(e). The fit parameters were  $R_{1/e} = 353.5 \pm 0.1 \text{ } \mu\text{m}$  and  $n_{SG} = 4.86 \pm 0.01$ , where the errors indicate the 95% confidence band from the fitting. The ellipticity was inferred with 0.8%, which means that the beam profile is close to circular. The fitting process of the UVETP data yielded  $R_{1/e} = 358.4 \pm 0.0 \text{ } \mu\text{m}$ ,  $n_{SG} = 5.03 \pm 0.00$ , and an ellipticity of 1.4%. The fitting values from XTP are slightly lower than those from UVETP; however, this is not significant. The statistical errors for  $R_{1/e}$  and  $n_{SG}$  were estimated by repeating the same measurement for the same beam over multiple shots and several campaigns. The errors for the XTP method are 1.0% and 3.4% for  $R_{1/e}$  and  $n_{SG}$ , respectively, and 0.1% and 1.9% for the UVETP method, respectively. Systematic errors in the XTP method include magnification errors, calibration errors, and the limitation in dynamic range, which are estimated with  $\sim 2.7\%$  and  $\sim 4.5\%$  for  $R_{1/e}$  and  $n_{SG}$ , respectively. With respect to the estimated error budget, the UV profiles from the XTP and UVETP diagnostics are in agreement.

The XTP data from 11 beams show some spread in spot size with Beam 52 having the largest spot ( $R_{1/e} = 365.0 \text{ } \mu\text{m}$ ) and Beam 61 the smallest spot ( $R_{1/e} = 345.9 \text{ } \mu\text{m}$ ). The difference in spot size between the largest and the smallest beams is  $19 \text{ } \mu\text{m}$

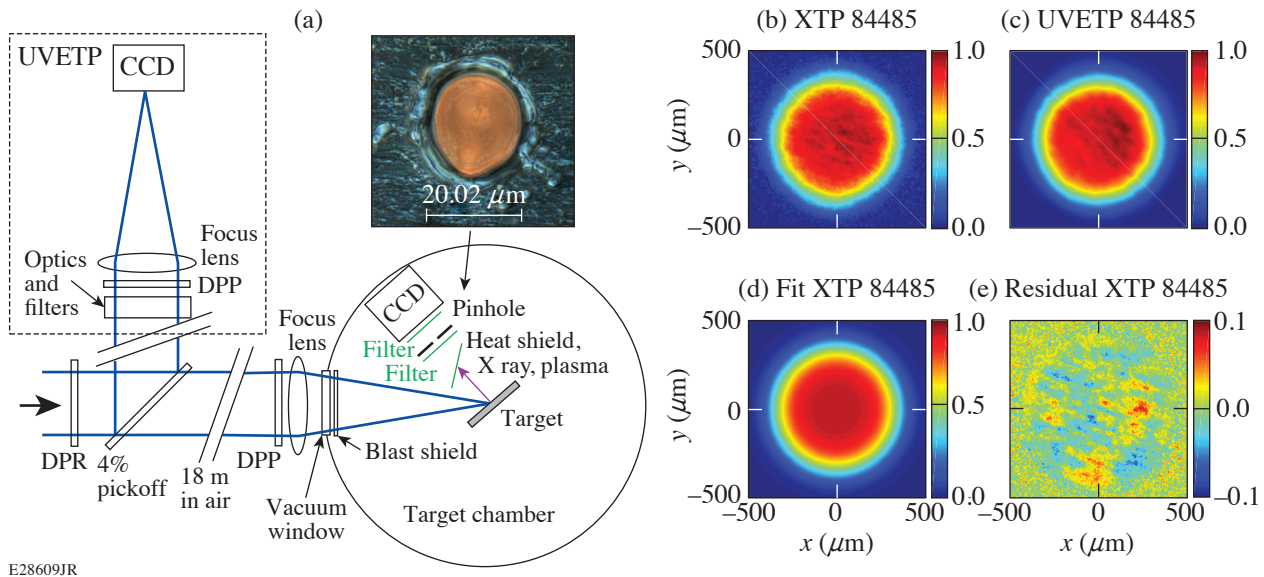


Figure 1

(a) Schematic of the experimental setup of the XTP and UVETP measurements including an optical image of a pinhole that measured the laser spots when using a 100-ps pulse. DPR: distributed polarization rotator. [(b)–(e)] UV laser-spot profiles from (b) XTP and (c) the UVETP diagnostic of Beam 56 for shot 84485. A 100-ps pulse was used. (d) The fitted 2-D super-Gaussian profile to the XTP image and (e) the residual of XTP (data minus fit).

( $\sim 5\%$ ), which is larger than the measurement error; therefore, it is likely real. The peak fluence difference on target between Beams 52 and 61 is estimated with  $\sim 11\%$ . The average XTP values over the 11 beams resulted in  $R_{1/e} = 356.6 \mu\text{m}$  and  $n_{\text{SG}} = 4.92$ . The average XTP values over those four beams that were covered by UVETP resulted in  $R_{1/e} = 358.9 \mu\text{m}$  and  $n_{\text{SG}} = 5.03$ , which agree with the averaged UVETP data within the errors.

Figure 2 shows the beam-to-beam variation of the peak fluence normalized to the average value for (a) the 100-ps and (b) the 1-ns pulse measurements. The same energy was assumed on all beams. The red squares refer to the XTP diagnostic and the blue diamonds refer to the UVETP diagnostic. The yellow band indicates the acceptable rms variation ( $\sigma_{\text{rms}}$ ) in peak fluence based on variation in beam shape, which is  $\sigma_{\text{rms}} \approx 2\%$ . The XTP data from the 11 beams indicate  $\sigma_{\text{rms}} \approx 3\%$  for both the 100-ps and 1-ns pulse measurements, which is slightly larger than the acceptable variation. The UVETP data from the four beams result in  $\sigma_{\text{rms}} \approx 1.5\%$ , which is below the limit.

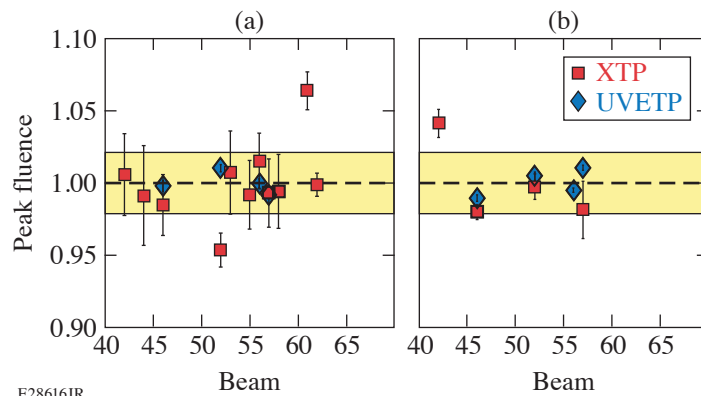


Figure 2

Beam-to-beam variation of the peak fluence normalized to the average value for (a) the 100-ps and (b) the 1-ns pulse measurements. The red squares refer to the XTP diagnostic and the blue diamonds refer to the UVETP diagnostic.

This material is based upon work supported by the Department of Energy National Nuclear Security Administration under Award Number DE-NA0003856, the University of Rochester, and the New York State Energy Research and Development Authority.

1. S. P. Regan *et al.*, Phys. Rev. Lett. **117**, 025001 (2016); **117**, 059903(E) (2016).
2. A. Bose *et al.*, Phys. Rev. E **94**, 011201(R) (2016).

# Magnetically and Optically Tunable Terahertz Radiation from Ta/NiFe/Pt Spintronic Nanolayers Generated by Femtosecond Laser Pulses

R. Adam,<sup>1</sup> G. Chen,<sup>2</sup> D. E. Bürgler,<sup>1</sup> T. Shou,<sup>3</sup> I. Komissarov,<sup>3</sup> S. Heidtfeld,<sup>1</sup> H. Hardtdegen,<sup>4</sup> M. Mikulics,<sup>1</sup> C. M. Schneider,<sup>1,5</sup> and R. Sobolewski<sup>2,3</sup>

<sup>1</sup>Research Centre Jülich, Peter Grünberg Institute

<sup>2</sup>Materials Science Graduate Program and Laboratory for Laser Energetics, University of Rochester

<sup>3</sup>Department of Electrical and Computer Engineering and Laboratory for Laser Energetics, University of Rochester

<sup>4</sup>Research Centre Jülich, Ernst Ruska Centre for Microscopy and Spectroscopy with Electrons

<sup>5</sup>Department of Physics, University of California, Davis

Terahertz (THz) radiation covers the electromagnetic spectrum range between radiofrequency millimeter waves and optical far-infrared radiation, approximately 0.3 to 30 THz, and has been applied in astronomy, medical imaging, security, communication, and manufacturing<sup>1,2</sup> as well as a scientific tool in materials testing<sup>3</sup> and bio imaging,<sup>4</sup> or in the study of electron wakefield acceleration.<sup>5</sup> Among different THz sources, current extensive research focuses on emitters of ultrafast electromagnetic transients with a broad THz-range spectrum in order to control and capture spin,<sup>6</sup> charge,<sup>7</sup> or phase-transition-related processes on subpicosecond time scales. Recent observation of THz emissions from optically excited ferromagnet/metal (F/M) nanolayers<sup>8–11</sup> establishes a very elegant link between laser optics, spintronics, and THz radiation, merging these three very active scientific fields and having a tremendous potential for future applications. The uncomplicated fabrication of spintronic THz emitters can lead to widespread applications.

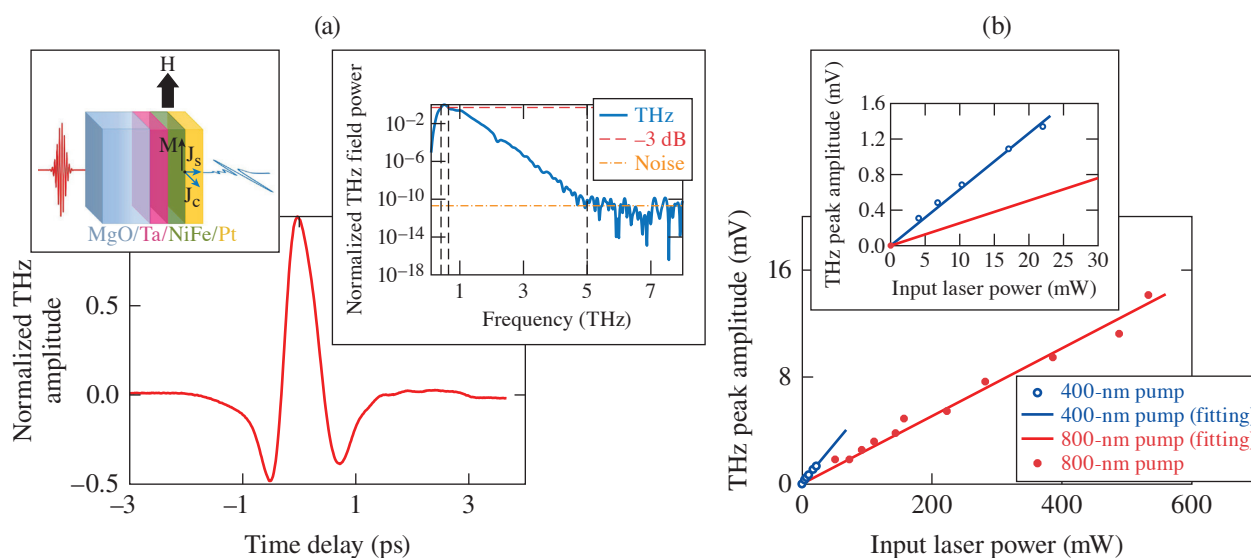
Superdiffusive spin currents generated in laser-driven demagnetization experiments have been theoretically predicted<sup>12</sup> and, subsequently, quickly confirmed in a number of experiments,<sup>13–17</sup> demonstrating their crucial role in ultrafast magnetization dynamics in a range of magnetic materials and structures. The central role of the superdiffusive currents in THz generation<sup>9</sup> has further strengthened their importance in laser-driven spin transient dynamics and has led to applications that are currently emerging at the border of laser physics and spin-based electronics. A simple physical mechanism has been proposed to explain the generation of THz transients from femtosecond laser-driven F/M bilayers and multilayers. THz emission is explained by the photon-driven spin current flowing from an F film to a neighboring M material. This spin current is, subsequently, converted by the inverse spin Hall effect (ISHE) into a transient charge current flowing along the M surface, thereby generating a laser-helicity independent subpicosecond electromagnetic signal.<sup>10,18</sup>

We have generated bursts of strong THz radiation (transient, single-picosecond-in-duration electromagnetic signals) by placing Ta/NiFe/Pt (equivalently, Ta/Py/Pt, where Py stands for permalloy: Ni<sub>80</sub>Fe<sub>20</sub>) trilayers in a static magnetic field and illuminating them with a train of 100-fs-wide laser pulses from a commercial Ti:sapphire laser (800-nm wavelength and 76-MHz repetition rate). The train of laser pulses was split into two beams with a 90:10 intensity ratio. The high-intensity branch, after bouncing from a retroreflector mounted at the delay stage, was focused at our F/M sample, while the low-intensity beam was used to excite a photoconductive low-temperature-grown GaAs (LT-GaAs) switch acting as a THz transient detector.<sup>19</sup> The linear motion of the delay stage in the pump beam, with a 2.5- $\mu$ m-step size, allowed an optical path control with a 16.6-fs time resolution. Ta/Py/Pt samples were optically excited either by illumination of the metallic surface (direct geometry) or by laser pulses passing through the MgO substrate (reverse geometry). In addition, we used a Teflon (polytetrafluoroethylene) lens with a 5-mm diameter and 10-mm focal length to focus the THz radiation at the LT-GaAs detector operated in a photoconductive-sampling mode. The latter allowed us to reconstruct the THz transient in time domain. The external **H** field was generated either by electromagnet

coils wrapped around iron yokes and supplying a variable field of up to 70 kA/m or by a pair of permanent magnets generating a fixed,  $\sim 40$ -kA/m field.

Our spintronic samples consisted of Ta (2-nm)/Py (2-nm)/Pt (2-nm) nanotrayers and were deposited sequentially at room temperature by magnetron sputtering on top of optically polished  $10 \times 10$ -mm<sup>2</sup> MgO substrates with (100) surface orientation. The deposition thickness for each layer was monitored by a quartz crystal microbalance. The thin, 2-nm Ta buffer layer was deposited first, directly onto the MgO substrate to achieve a good adhesion and smoothness of the consecutive layers. We have chosen Pt as a top material for its relatively high spin-orbit coupling: the material-dependent parameter that, according to literature, is responsible for THz generation in magnetic nanolayers.<sup>20</sup>

Figure 1(a) presents a typical time-domain, subpicosecond (0.9-ps FWHM of the main peak) electromagnetic transient generated by our spintronic nanolayer emitter and detected by the LT-GaAs detector. The zero time on the time axis was chosen arbitrarily, but it was kept the same for all measurements. The measurement was done in the reverse geometry, illustrated in the left inset in Fig. 1(a) with the  $\mathbf{H}$  field fixed at 55 kA/m and applied in the sample plane. The laser fluence was  $7.25 \mu\text{J}/\text{cm}^2$ . In this geometry, we have also observed (not shown here) a secondary, significantly weaker THz transient, delayed by  $\sim 10$  ps with respect to the main signal. The latter signal was identified as a THz transient generated at the Py/Pt bilayer and propagating in the opposite direction with respect to the main one and, subsequently, reflected at the MgO/air interface. A fast Fourier transform (FFT) of the time-domain waveform is shown in the right inset in Fig. 1(a) as the normalized THz transient power spectrum. We note that the signal frequency content extends up to 5 THz with a 3-dB cutoff at 0.85 THz. A small dip visible in the power spectrum at about 2 THz corresponds to resonant absorption of a Teflon lens used to focus the THz beam. When we flipped the trilayer by  $180^\circ$  and illuminated it in the direct geometry, keeping the laser beam and  $\mathbf{H}$  orientation unchanged, we recorded essentially the same time-domain transient as shown in the main panel of Fig. 1(a), but with the polarity reversed. As we discuss below, the latter indicates a reversed direction of the charge current density  $\mathbf{J}_C$ . Compared to the reverse geometry, the signal in direct geometry had a slightly lower amplitude (apparently caused by THz absorption by Ta and MgO) and no secondary reflected signal was



E28275JR

Figure 1

(a) A normalized THz transient generated by a 100-fs-wide laser pulse impinging at a Ta/Py/Pt nanotrayer through the MgO substrate (reverse illumination geometry). The left inset shows the trilayer stacking and the schematics of the THz-generation mechanism. The right inset presents a normalized THz power spectrum that corresponds to the pulse shown in the main panel. The spectrum exhibits a 3-dB cutoff at 0.85 THz and extends to 5 THz with exponentially decreasing intensity. (b) A THz transient amplitude as a function of the incident laser beam power for both fundamental ( $\lambda = 800$  nm; solid red circles) and frequency-doubled light ( $\lambda = 400$  nm; open blue circles). The inset shows the available power range for the 400-nm light and demonstrates a strongly increased efficiency of THz generation at the 400-nm wavelength.

observed. Finally, we optically illuminated the Pt/Py/Ta trilayer from the Pt side at a  $45^\circ$  incidence angle and collected a THz transient with the detector positioned at  $90^\circ$  with respect to the laser beam. As expected for superdiffusive current flowing in all directions, the recorded time-domain waveform had a shape identical to the pulse shown in the main panel of Fig. 1(a). The power spectra for the direct, reverse, and  $45^\circ$  illumination geometries were identical to that presented in Fig. 1(a), right inset. The above observations indicate that optically triggered THz transients originate near or at the Py/Pt interface.

We have also studied the impact of varying external optical excitation on the THz signal emitted by our spintronic Ta/Py/Pt emitter. Figure 1(b) shows the maximum THz-signal amplitude  $A^{\text{THz}}$  dependence on the incident, average laser power at both the fundamental ( $\lambda = 800$  nm; solid red circles) and frequency-doubled ( $\lambda = 400$  nm; open blue circles) wavelengths at a constant magnetic field  $H = 55$  kA/m. In both cases, the dependence is linear, as indicated by the corresponding linear fits. Although the range of available incident powers for the 400-nm light was quite small, limited by the efficiency of the frequency-doubling barium borate (BBO) crystal, our data clearly demonstrate that for the same laser power, 400-nm photons generate approximately  $3\times$  larger subpicosecond transients, as compared to the 800-nm photons. At the same time, the corresponding normalized time-domain waveforms (not shown) were practically the same as the one shown in Fig. 1(a), main panel, resulting in the identical THz power spectra. Although our studies seem to contradict recent results of Herapath *et al.*,<sup>21</sup> where no pump wavelength dependence on THz generation was reported, we stress that the measurements presented in Ref. 21 were performed not only on a different material system, but, first of all, exclusively at infrared wavelengths (900 to 1500 nm). High-energy green photons used in our studies are certainly more efficiently absorbed by metallic nanolayers and generate a significantly larger concentration of hot electrons that couple to the spins. As a result, we observe the THz amplitude enhancement as it was discussed above and presented in Fig. 1(b).

An external electromagnet in our THz setup allowed us to tune the  $\mathbf{H}$  field in a range up to  $\pm 70$  kA/m. For a constant laser light ( $\lambda = 800$  nm) with an average laser power of 550 mW, we stepped  $\mathbf{H}$  from  $-70$  kA/m to  $+70$  kA/m and back to  $-70$  kA/m, and by this sequence we recorded the  $A^{\text{THz}}$  dependence on the magnitude of the in-plane  $\mathbf{H}$  field applied to our Ta/Py/Pt trilayer. We observed that the  $A^{\text{THz}}(\mathbf{H})$  hysteresis overlaid perfectly on the shape of the static hysteresis of the magnetic moment  $\mu(\mathbf{H})$  of the Py nanolayer, recorded using a commercial physical property measurement system (PPMS). Most interestingly, the measured  $A^{\text{THz}}(\mathbf{H})$  curve exhibited hysteresis that was significantly narrower than that of the pure Py layer.

The main question is why  $A^{\text{THz}}(\mathbf{H})$  for our samples follows the shape of the static hysteresis of the Py film. Our optical beam is linearly polarized, so we are in the laser-helicity independent case and the THz transient is directly proportional to  $\mathbf{J}_C$  produced by the ISHE mechanism that in turn depends on the spin current density  $\mathbf{J}_S$  and spin polarization  $\boldsymbol{\sigma}$ . According to, e.g., Saitoh *et al.*<sup>22</sup>  $\mathbf{J}_C = D_{\text{ISHE}} (\mathbf{J}_S \times \boldsymbol{\sigma})$ , where  $D_{\text{ISHE}}$  is a coefficient representing the ISHE efficiency in a material. Therefore, we can control the ultrafast time-domain signal amplitude and polarity by controlling the  $\mathbf{J}_C$  amplitude and its direction. The  $\mathbf{J}_C$  amplitude is controlled in our case through  $\boldsymbol{\sigma} \sim \mu(\mathbf{H})$ , while the  $\mathbf{J}_C$  direction is controlled by the illumination geometry (direct or reverse). We note that in both geometries the superdiffusive current flows in all directions as confirmed by the experiment with laser illumination under  $45^\circ$  mentioned above; nevertheless, only the  $\mathbf{J}_C$  component pointing from Py to Pt matters for THz generation. For fixed directions of  $\mathbf{H}$  and  $\mathbf{J}_S$ , and because  $\mathbf{J}_C \sim \mu(\mathbf{H})$ , one should expect that  $A^{\text{THz}}(\mathbf{H})$  behaves similar/identical to the  $\mu(\mathbf{H})$  dependence, as, indeed, is observed in our studies. The observed significantly narrower width of the  $A^{\text{THz}}(\mathbf{H})$  hysteresis in the Ta/Py/Pt trilayer as compared to the  $\mu(\mathbf{H})$  hysteretic dependence may arise from the fact that the static  $\mu(\mathbf{H})$ , measured in PPMS, represents a signal averaged over the whole sample volume. Therefore, for instance, pinning at the sample edges may contribute to the signal, while THz generation is local, defined by a laser beam spot ( $\sim 50$   $\mu\text{m}$  in diameter). Finally, we note that in order to generate THz transients in our soft, magnetic Py-based samples with vanishing remanence, an external  $\mathbf{H}$  field was always necessary. On the other hand, our preliminary measurements performed on magnetically harder materials show that after the initial magnetization, no external  $\mathbf{H}$  is required to generate high-intensity THz transients. (Studies of transient THz emission from magnetically harder nanobilayers will be published separately.)

In conclusion, we have generated subpicosecond electromagnetic transients from Ta (2-nm)/Py (2-nm)/Pt (2-nm) spintronic nanotrayers using a train of 100-fs-wide laser pulses and a static magnetic field (up to  $\pm 70$  A/m) applied in the plane of a sample. Resulting power spectra of the transients extend up to 5 THz with a 3-dB cutoff at 0.85 THz. The amplitude of the transients depends linearly on the average laser power; however, for the same laser power, blue photons (400-nm wavelength) generate THz

transients with amplitudes approximately  $3\times$  larger than transients resulting from excitation by infrared (800-nm-wavelength) photons. The THz amplitude of emitted signals is tunable by the **H**-field intensity and follows the hysteretic behavior of the magnetization versus **H**-field dependence of the pure Py layer, albeit  $A^{\text{THz}}(\mathbf{H})$  is, in practice, nonhysteretic. Finally, we note that our simple, robust, and tunable THz emitters can lead to widespread applications in compact, hand-held THz diagnostic devices, in local device-to-device communication with enormous data transfer capacity, or as sources for material and circuit testing at THz frequencies.

The work at the Research Center Jülich was performed within *JuSPARC* (Jülich Short-pulse Particle Acceleration and Radiation Center), a strategy project funded by the BMBF. Research at Rochester has been supported in part by the grant from the HYPRES Co., and by the New York State Advanced Technology Centers for Innovative and Enabling Technologies (University of Rochester) and Advanced Sensor Technologies (Stony Brook University).

1. M. Tonouchi, *Nat. Photonics* **1**, 97 (2007); E. A. Williams, *National Association of Broadcasters Engineering Handbook*, 10th ed. (Elsevier, Burlington, MA, 2007).
2. R. A. Lewis, *J. Phys. D: Appl. Phys.* **47**, 374001 (2014).
3. A. Koroliov *et al.*, *Appl. Sci.* **9**, 391 (2019).
4. K. Ajito and Y. Ueno, *IEEE Trans. Terahertz Sci. Technol.* **1**, 293 (2011).
5. E. A. Nanni *et al.*, *Nat. Commun.* **6**, 8486 (2015).
6. S. Baierl *et al.*, *Nat. Photonics* **10**, 715 (2016).
7. R. L. Milot *et al.*, *Nano Lett.* **16**, 7001 (2016).
8. G. Torosyan *et al.*, *Sci. Rep.* **8**, 1311 (2018).
9. T. Seifert *et al.*, *Appl. Phys. Lett.* **110**, 252402 (2017).
10. T. Kampfrath *et al.*, *Nature Nanotechnol.* **8**, 256 (2013).
11. Y. Wu *et al.*, *Adv. Mater.* **29**, 1603031 (2017).
12. M. Battiato, K. Carva, and P. M. Oppeneer, *Phys. Rev. B* **86**, 024404 (2012).
13. D. Rudolf *et al.*, *Nat. Commun.* **3**, 1037 (2012).
14. E. Turgut *et al.*, *Phys. Rev. Lett.* **110**, 197201 (2013).
15. S. Mathias *et al.*, *Proc. Nat. Acad. Sci.* **109**, 4792 (2012).
16. A. Eschenlohr *et al.*, *Nat. Mater.* **12**, 332 (2013).
17. J. Sinova *et al.*, *Rev. Mod. Phys.* **87**, 1213 (2015).
18. G. Li *et al.*, *J. Phys. D: Appl. Phys.* **51**, 134001 (2018).
19. A. Geizütis *et al.*, *Opt. Mater.* **30**, 786 (2008).
20. T. Seifert *et al.*, *Nat. Photonics* **10**, 483 (2016).
21. R. I. Herapath *et al.*, *Appl. Phys. Lett.* **114**, 041107 (2019).
22. E. Saitoh *et al.*, *Appl. Phys. Lett.* **88**, 182509 (2006).

# Investigation of Mechanisms of Laser-Induced Secondary Contamination from Metal Particles Attached on the Input Surface of Optical Components

S. G. Demos,<sup>1</sup> J. C. Lambropoulos,<sup>1</sup> R. A. Negres,<sup>2</sup> M. J. Matthews,<sup>2</sup> and S. R. Qiu<sup>2</sup>

<sup>1</sup>Laboratory for Laser Energetics, University of Rochester

<sup>2</sup>Lawrence Livermore National Laboratory

Laser-induced damage on large-aperture optical components exposed to high-average-power or peak-intensity laser pulses is a well-recognized issue that affects the operational parameters as well as the cost of such systems. The origin of this issue is associated with the presence of absorbing defects incorporated into the optical material during the manufacturing process or resulting from contaminant species incorporated from handling or within the operational environment. Metallic particles are commonly found contaminants on surfaces of optical components in high-energy laser systems such as at the National Ignition Facility. Researchers have made great efforts to understand the impact of these contaminants on their laser performance.<sup>1–21</sup> The knowledge attained from this previous work is directly applicable to the present study, which examines the dynamics of the interaction of microscale, nominally spherical metal particles attached on the input (front) surface of optics. As the momentum attained by the particle thrusts the particle against the surface, the resulting response of the particle is nontrivial. Previous work has provided only the phenomenology of the final modifications, while the intermediate steps were speculative and qualitatively described. To address this issue, the present work involves time-resolved microscopic shadowgraphy with adequate spatial and temporal resolution to resolve details of the dynamics of plasma formation, shock-wave expansion, particle ejection, and secondary contamination by small molten droplets that separated from the original particle.

The basic experimental system used in this work includes a pump laser operating at 355 nm, producing  $\approx 8$ -ns (FWHM) pulses, or 1064 nm, producing  $\approx 10$ -ns pulses. A different excitation geometry and substrate were used with each excitation wavelength. Specifically, excitation at 355 nm was used in combination with stainless-steel particles (316L alloy) dispersed on the input surface of a 5-cm-round, 0.5-mm-thick commercially available silica substrate. In addition, titanium particles dispersed on the surface of an  $\sim 7$ - $\mu\text{m}$ -thick multilayer dielectric high reflector at  $45^\circ$  and  $p$  polarization were studied under excitation at 1064 nm, where the  $\text{SiO}_2/\text{HfO}_2$  multilayer dielectric coatings were deposited on a 5-cm-round, 10-mm-thick commercially available BK7 and optimized to provide reflectivity of  $>99.5\%$  at 1053 nm. In both cases, particles that were similar in diameter were selected to be exposed to the pump pulses having a diameter of the order of  $20 \mu\text{m}$ . The beam profile of the pump laser impinging on the surface of the substrate was nearly flattop (with  $\sim 25\%$  local intensity variations) and had an elliptical shape (because of the angle of incidence of the laser beam) with a minor axis of about  $315 \mu\text{m}$ . The pump laser fluence was about  $12.5 \pm 2 \text{ J/cm}^2$  under 355-nm excitation and about  $17.5 \pm 2 \text{ J/cm}^2$  under 1064-nm excitation, both of which are relevant to the operational fluences used in large-aperture laser systems.

Two identical microscope systems providing  $25\times$  or  $50\times$  optical magnification were positioned orthogonally to each other and used to image the area containing the particle along the surface of the sample, referred to as a transmission-view (TV) microscope, and normal to the surface, referred to as a side-view (SV) microscope. Time-resolved images (Fig. 1) were acquired using pulsed illumination obtained from the probe laser operating at 532 nm, producing 180-ps (FWHM) pulses. The output of the probe beam was split to illuminate the particle parallel and orthogonally to the substrate surface, making it possible to acquire dynamic images of the particle's response to the laser pulse at predetermined delay times with respect to the time of peak intensity of the pump pulse. The probe laser fluence was of the order of  $1 \text{ mJ/cm}^2$  and had no impact on the behavior of the particles under exposure to probe pulses alone.

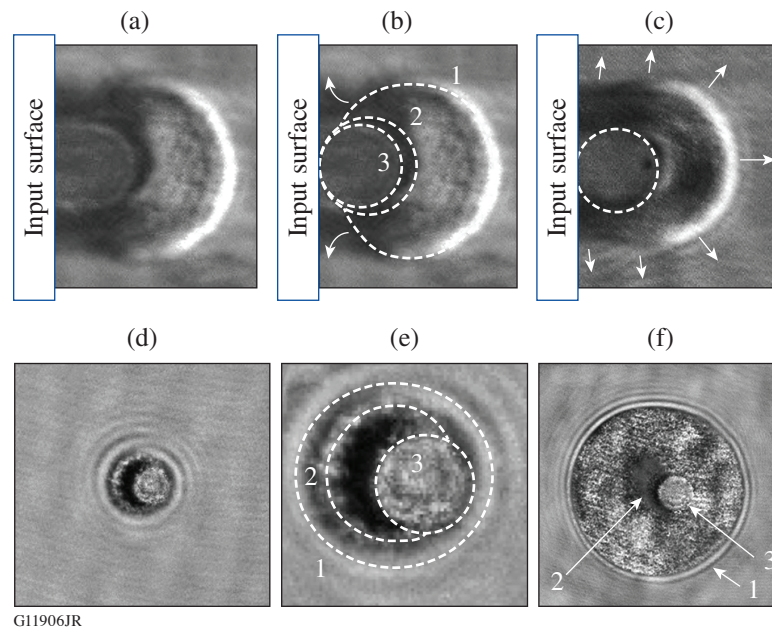


Figure 1

[(a)–(c)] Side-view images of the location of the stainless-steel particle (18- $\mu\text{m}$  diameter) acquired at an  $\approx -3\text{-ns}$  delay under a 355-nm laser exposure of  $\approx 12\text{ J/cm}^2$ , capturing the position of the shock wave (1) at different stages of its expansion along with (2) the plume and (3) the particle. (a) and (c) are different events; (b) is the same as (a) with the features of interest outlined by dashed lines. The laser illuminates the particle from the right-hand side. [(d)–(f)] Transmission-view images of the location of the stainless-steel particle (17- $\mu\text{m}$  diameter), acquired at about a  $-4\text{-ns}$  delay, capturing the asymmetric expansion of (1) the shock wave and (2) the plume along the substrate surface, as well as (3) the particle. (d) and (f) are different events; and (e) is a digital magnification of (d) with the features of interest outlined by dashed lines. The laser illuminates the particle from the left-hand side.

The results suggest that there are three contamination mechanisms following the interaction of laser pulses with metallic particles attached to the input surface of optics. The first mechanism is related to the initial plume expansion toward the surface, which would leave a layer of contamination around the particle. The second mechanism is related to the liquid material formed on the particle that separates during the ejection of the particle from the surface. This material is subsequently deposited around the initial particle location and mostly on the side of the particle along the direction of laser irradiation. The third mechanism is related to droplets of liquid material that separate from the particle after its ejection. As a result, these droplets can be deposited at significant distances from the initial location of the particle.

The trail of the droplets deposited on the surface via the third mechanism allows one to appreciate the direction of propagation of the particles after their ejection from the surface. For nearly spherical particles, it was observed that the particles are ejected along (or close to) the plane defined by the direction of laser beam propagation and the orthogonal direction to the surface (along the  $x$ - $z$  plane). This is exemplified by the images shown in Fig. 2. Because the expansion of the plume is vertical to the surface, the attained momentum and direction of particle ejection depend strongly on its shape. This can be particularly important for irregularly shaped contamination particles, especially those with extended, nearly flat surfaces. The effects described here can lead to thrusting of the particle closer to the surface and subsequently an extended (spatially) contamination by liquid droplets.

The results obtained using the Ti particles dispersed on the multilayer dielectric coating surface suggest a more-severe secondary contamination compared to the contamination induced by stainless-steel particles on bare silica. This is assigned to the excitation geometry, namely the fact that laser light reflected on the coating illuminated the particle from the side, thereby increasing the total exposure fluence on the particle and creating liquified material over a larger part of its surface, including near its point of attachment on the coating surface.

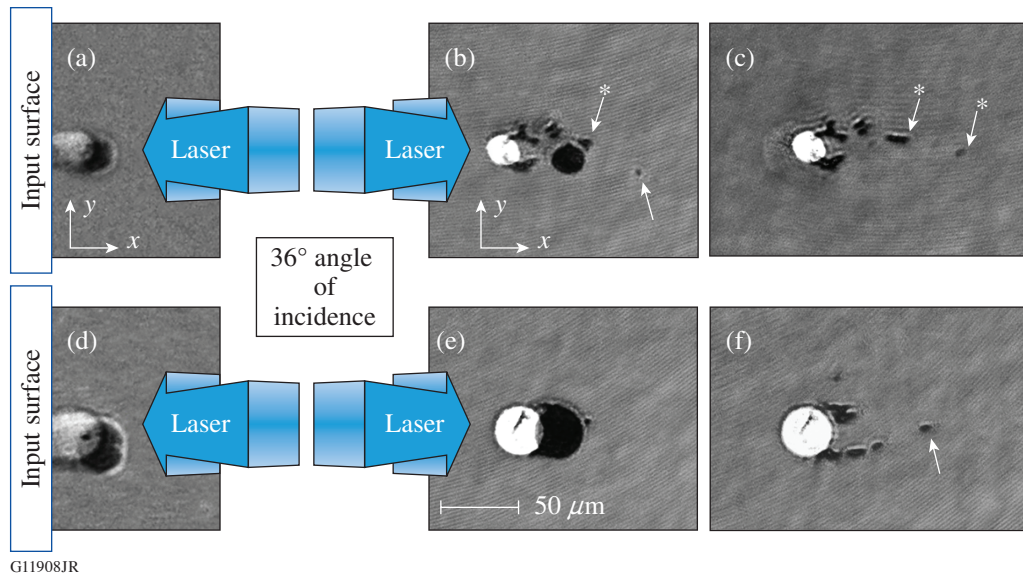


Figure 2

Two examples of the motion of stainless-steel particles at a 1025-ns delay as captured by (a) and (d) the SV microscope and (b) and (e) the TV microscope along with (c) and (f) the final TV images. [(a)–(c)] The particle is about  $21\ \mu\text{m}$  in diameter and exhibits motion of about  $13\ \mu\text{m}$  along the  $z$  axis and about  $42\ \mu\text{m}$  along the  $x$  axis. This means that the particle has been ejected from the surface at an angle of about  $73^\circ$  with respect to the  $z$  axis at a speed of about  $43\ \text{m/s}$ . Similarly, the particle in (d)–(f) was ejected at a speed of  $\approx 32\ \text{m/s}$ . (c) and (f) show the final images acquired at the end of the process, where only the contamination by liquid droplets that have separated from the particle is visible on the substrate surface. Comparison of the transient and final images allows one to better understand this secondary contamination process.

The behaviors observed in this work are expected to be analogous to those occurring under a wide range of excitation conditions when the interaction of the laser pulse with the particle supports an ablation event. For example, the morphology of secondary contamination under ultrashort pulsed excitation<sup>22</sup> is similar to that observed with the nanosecond pulses used in this work and can be fully explained using the dynamic processes described here.

This material is based upon work supported by the Department of Energy National Nuclear Security Administration under Award Number DE-NA0003856, the University of Rochester, and the New York State Energy Research and Development Authority. This work was performed in part under the auspices of the U.S. Department of Energy by Lawrence Livermore National Laboratory under Contract No. DE-AC52-07NA27344.

1. M. D. Feit *et al.*, Proc. SPIE **2966**, 417 (1997).
2. F. Y. Génin, M. R. Kozlowski, and R. Brusasco, Proc. SPIE **3047**, 978 (1997).
3. F. Y. Génin *et al.*, Proc. SPIE **2966**, 126 (1997).
4. D. M. Kane and D. R. Halfpenny, J. Appl. Phys. **87**, 4548 (2000).
5. S. Palmier *et al.*, Proc. SPIE **5991**, 59910R (2006).
6. M. A. Norton *et al.*, Proc. SPIE **5991**, 59910O (2006).
7. S. Palmier *et al.*, Appl. Opt. **47**, 1164 (2008).
8. Y. Ye *et al.*, Optik **123**, 1056 (2012).
9. T. Jitsuno *et al.*, Proc. SPIE **8786**, 87860B (2013).
10. X. Ling *et al.*, Appl. Surf. Sci. **270**, 346 (2013).

11. K. E. Gushwa and C. I. Torrie, Proc. SPIE **9237**, 923702 (2014).
12. M. J. Matthews *et al.*, J. Opt. Soc. Am. B **30**, 3233 (2013).
13. F. Y. Génin *et al.*, Appl. Opt. **39**, 3654 (2000).
14. E. Feigenbaum, S. Elhadj, and M. J. Matthews, Opt. Express **23**, 10589 (2015).
15. C. J. Stolz *et al.*, Proc. SPIE **10691**, 106910W (2018).
16. S. R. Qiu *et al.*, Appl. Opt. **54**, 8607 (2015).
17. S. R. Qiu *et al.*, Opt. Eng. **56**, 011108 (2016).
18. S. G. Demos *et al.*, Opt. Express **24**, 7792 (2016).
19. C. D. Harris *et al.*, Opt. Lett. **40**, 5212 (2015).
20. R. N. Raman *et al.*, Opt. Express **24**, 2634 (2016).
21. R. N. Raman, R. A. Negres, and S. G. Demos, Opt. Eng. **50**, 013602 (2011).
22. K. R. P. Kafka and S. G. Demos, Opt. Lett. **44**, 1844 (2019).

## The 11th Omega Laser Facility Users Group Workshop

M. Koepke,<sup>1</sup> J. A. Frenje,<sup>2</sup> S. Ali,<sup>3</sup> A. Casner,<sup>4</sup> M. Gatu Johnson,<sup>2</sup> E. Merritt,<sup>5</sup> P. Tzeferacos,<sup>6</sup> M. S. Wei,<sup>7</sup> and J. P. Knauer<sup>7</sup>

<sup>1</sup>West Virginia University

<sup>2</sup>Massachusetts Institute of Technology

<sup>3</sup>Lawrence Livermore National Laboratory

<sup>4</sup>University of Bordeaux

<sup>5</sup>Los Alamos National Laboratory

<sup>6</sup>University of Chicago

<sup>7</sup>Laboratory for Laser Energetics, University of Rochester

The purpose of the Omega Laser Facility Users Group (OLUG) is to facilitate communication and exchanges among the users: from the users as a group to the facility and from the users to the broader scientific community. As a major part of OLUG's responsibility, it organizes an annual 2.5-day workshop at the end of April. The 11th OLUG Workshop was held at the Laboratory for Laser Energetics (LLE) on 24–26 April 2019. It was attended by 110 researchers, including scientists, postdoctoral fellows, and students (Fig. 1). The attendees represented institutions from four countries, including the U.S., Canada, the U.K., and



U2480JR

---

Figure 1  
Group photo of the 11th Omega Laser Facility Users Group Workshop attendees.

---

France. Postdocs and students received travel support to attend the workshop from the Department of Energy's National Nuclear Security Administration. The program included talks, posters, an evening tutorial, student and post-doc sessions, and a discussion of Findings and Recommendations.

### **The Workshop Program**

The OLUG program included the following five science talks from newly funded National Nuclear Security Administration (NNSA) Centers: "Multi-University Center for Pulsed-Power-Driven HED Science" (Cornell University), "Center for Astrophysical Plasma Properties" (University of Texas, Austin), "Center for Matters under Extreme Conditions" (University of California, San Diego), "Center for Advanced Nuclear Diagnostics and Platforms for ICF and HED Physics at Omega, NIF, and Z" [Massachusetts Institute of Technology (MIT)], and "Center for Laboratory Astrophysics" (University Michigan). The Department of Energy's (DOE's) NNSA perspective was presented by Sarah Wilk, Deputy Director of NNSA's Office of Experimental Sciences (NA-113). Other highlights included an evening tutorial session, "Non-standard Targets," offered by Chuck Sorce (LLE) and the LLE engineering team; a facility talk, "Omega Facility Update and Progress on OLUG Recommendations," by Sam Morse (LLE); a summary of the OLUG ExCom election results by Johan Frenje (MIT); summaries of the EP-OPAL Proposal Workshop (Hans Rinderknecht, LLE) and MTW-OPAL (Jake Bromage, LLE); an update on the American Physical Society's Division of Plasma Physics (APS-DPP's) Community Planning Process by Carolyn Kuranz (University of Michigan); the student and postdoc discussion panel [Michelle Marshall, Lawrence Livermore National Laboratory (LLNL)]; and a discussion of OLUG's Findings and Recommendations with LLE management, led by Maria Gatu Johnson (MIT) and Liz Merritt [Los Alamos National Laboratory (LANL)]. In addition, LLE staff organized tours of the Omega Laser Facility.

Student, postdoc, scientist, and facility posters comprised a total of 68 poster presentations that were organized in three sessions. Of the total number, 44 posters were presented by graduate students, postdocs, and undergraduate students. Two additional posters were presented by high school students who had participated in LLE's 2018 Summer High School Research Program. Although OLUG was established in 2009, the Omega Laser Facility has been building a community of science users for more than 35 years. For example, since 1979 the Omega Laser Facility has had a vigorous National Laser User Facility (NLUF) program, funded through DOE, which permits access to external users through a proposal and review process. NLUF is the oldest, continuously running DOE program to support high-energy-density (HED) science research in universities and small businesses.

### **Nominations and Election**

In November 2018, a nominating committee formed to request January nominations for the February election of one new executive committee (EC) member. Johan Frenje (Chair, MIT), Patrick Knapp (Sandia National Laboratories), and Ryan Rygg (LLE) formed the committee. Elected from the three-candidate ballot were Sean Finnegan (LANL) to a three-year term to replace Mingsheng Wei [formerly of General Atomics (GA)] and Mario Manuel (GA) to a special one-year term to replace Channing Huntington (LLNL) who withdrew from the OLUG ExCom after the election process began. The May 2019–May 2020 EC membership of OLUG includes (a) four from U.S. university/small business: Mark Koepke (West Virginia University, Chair), Maria Gatu Johnson (MIT), Johan Frenje (MIT, Vice Chair), and Petros Tzeferacos (University of Chicago); (b) three from national laboratory/major business: Liz Merritt (LANL), Sean Finnegan (LANL), and Mario Manuel (GA); (c) one non-U.S. researcher: Alexis Casner (University of Bordeaux); (d) one from the junior researcher list: Suzanne Ali (LLNL); and (e) LLE, ex-officio: Jim Knauer. The OLUG EC is very grateful to Mingsheng Wei and Channing Huntington for their service in the EC and their contributions to the success of OLUG.

### **Summary of Findings and Recommendations**

An important outcome of OLUG's annual workshop is the list of Findings and Recommendations that OLUG submits for consideration to LLE's management every year. The 2019 Findings and Recommendations are summarized below.

1. Implement a Shot Request Form that "auto-saves" the entered text.
2. Add diagnostic and beam information documentation to the PI (Principal Investigator) Portal.
3. Provide tools for estimating diagnostic signal levels.
4. Extend image-plate calibrations at <10 keV and 200 keV to 1 MeV.

5. Provide calibrations for spectrometer crystals.
6. Increase Dante filter and part availability.
7. Implement  $\gamma$ -ray spectroscopy for nuclear science.
8. Allow velocity interferometer system for any reflector (VISAR)/streaked optical pyrometer (SOP) capability on ten-inch manipulator TIM-14 (OMEGA EP).
9. Upgrade/improve VISAR/SOP.
10. Implement hardware mitigation for early-time radiation artifact on x-ray framing cameras.
11. Add CR-39 processing capability.
12. Ensure that Shot Request Form selectable setups for the streaked x-ray imager match the actual inventory.
13. Add charged-particle signal mitigation to multiple diagnostics.
14. Modify the electron–positron–proton spectrometer to measure higher-energy electrons ( $E_{\max} \sim \text{GeV}$ ).
15. Add a single line of sight for multiframe single-pinhole imaging.
16. Improve framing-camera pointing procedures for x-ray imaging.
17. Make Thomson scattering on DT shots compatible with the DT<sup>3</sup>He backlighter.
18. Provide a second and/or third Thomson parabola ion energy (TPIE) analyzer.
19. Implement a more-sensitive neutron time-of-flight detector for secondary DT-n measurements.
20. Investigate upgrades to fixed x-ray pinhole cameras.
21. Provide Thomson-scattering capability on OMEGA EP.
22. Add tritium gas-fill capability into a warm spherical capsule.
23. Provide special gas fills using a variable fuel mixture, with or without tritium.
24. Install a planar cryogenics system on OMEGA EP.

The impact within the HED field of the Omega Laser Facility is broad and deep and is encountered early in one's researcher career. Omega offers tremendous opportunities for programmatic-science and basic-science research. NNSA's NLUF and Laboratory Basic Science Programs play a key student and postdoc training role at Omega. Students and postdocs publish in peer-reviewed, high-impact journals on subjects including OMEGA research on laboratory astrophysics, hydrodynamics and atomic physics, hydrodynamic instabilities, radiation hydrodynamics, materials physics and behavior of the equation of state under extreme conditions, relativistic laser–plasma interactions, magnetized plasmas, advanced/alternative inertial fusion concepts, nuclear physics, atomic physics and spectroscopy, and new diagnostics and instrumentation.

The next OLUG Workshop will be held at LLE from 29 April–1 May 2020.

This OLUG Workshop was made possible in part by the generous support of the National Nuclear Security Administration of the U.S. Department of Energy for travel expenses of students and postdocs; by MIT; and by the Laboratory for Laser Energetics at the University of Rochester for the use and availability of critical resources and support. In addition, OLUG thanks the LLE management for their responsiveness to our Findings and Recommendations. For capturing through his lens the workshop ambiance, OLUG thanks Eugene Kowaluk.

# The Optics Suitcase: An Educational Outreach Tool for Inspiring Careers in Light

J. DeGroot Nelson,<sup>1,2</sup> T. Z. Kosc,<sup>2,3</sup> and P. C. Nelson<sup>4</sup>

<sup>1</sup>Optimax Systems, Inc.

<sup>2</sup>The Optical Society, Rochester Section

<sup>3</sup>Laboratory for Laser Energetics, University of Rochester

<sup>4</sup>Masline Electronics

Developed by the Optical Society Rochester Section (OSA-RS), the Optics Suitcase is an innovative, interactive presentation package designed to introduce middle school students to the dynamic and exciting range of concepts within the study of light. The Optics Suitcase (see Fig. 1) is an educational outreach tool developed by Dr. Stephen D. Jacobs and the OSA-RS with the busy professional in mind. It is designed to make it easy to enter a middle school classroom and excite young people about careers in technology using experiments that can be customized to highlight the presenter's interests, job, and work environment.



G12818JR

Figure 1  
Photograph of the Optics Suitcase and its contents.

The Optics Suitcase contains reusable supplies and giveaway theme packets for in-class presentations that explore color in white light (see Table I). The goal is to help promote technology careers to middle school students. A detailed presentation guide is included with the suitcase to help give presenters techniques for engaging students during the presentation and making the demonstrations more interactive.

Three experiments explore the colors constituting white light in the form of diffraction (The Rainbow Peephole), polarization (Magic Stripes), and selective reflection (Magic Patch). These three experiments use giveaway theme packets that are designed to help reinforce the study of light concepts at home as students present the information they learned to their family and friends. The objective of the Optics Suitcase is to convey a sense of excitement about technology in a short period of time. To achieve this goal, the initial demonstrations serve as “ice breakers” and are intended to quickly capture the students’ attention. Next, three hands-on activities use the theme packets and illustrate the overall theme of “colors in white light.” They are presented at

a pace best suited (as determined by the presenter) to retain the students’ interest; children often enjoy taking the theme packets home and sharing with others. The presenter can customize the template take-home flyer with a name, the date, and the location of the presentation to help reinforce the message with the students. A quick review of the presentation guide and an enthusiastic attitude will result in a fun, interactive, and educational outreach activity.

Table I: List of Optics Suitcase reusable and giveaway supplies.

Quantity	Item—Reusable Supplies
1	Durable suitcase with room for other items that can be added to customize presentation
1	Instruction guide on laminated sheets
1	USB-stick with supplemental Optics Suitcase materials
1	Hot Snapz heat pad
1	Set of Arbor Scientific “Happy and Unhappy” balls
1	Slinky
1	50-mm silicon wafer, one side polished to a “mirror” finish
1	Silica glass lens
1	5-in. × 5-in. pieces of high-quality sheet polarizer
1	Transparent plastic cups
1	Set of transparent plastic tableware: knife, fork, and spoon
1	6-in. × 6-in. sheet of temperature-sensitive microencapsulated liquid crystal
Quantity	Item—Giveaway Supplies (can be restocked)
50	Rainbow Peephole: Color by Diffraction
50	Magic Stripes: Color by Polarized Transmission
50	Magic Patch: Color by Selective Reflection
50	Periodic Table of Elements

This material is based upon work supported by the Department of Energy National Nuclear Security Administration under Award Number DE-NA0003856, the University of Rochester, and the New York State Energy Research and Development Authority.

# Measurement for Palladium Hydride and Palladium Deuteride Isotherms Between 130 K and 393 K

M. Sharpe,<sup>1</sup> W. T. Shmayda,<sup>1</sup> and K. Glance<sup>2</sup>

<sup>1</sup>Laboratory for Laser Energetics, University of Rochester

<sup>2</sup>Pittsford Sutherland High School

Palladium is a unique hydride-forming metal that finds applications in next-generation target-filling systems and isotope separation systems. The uniqueness of palladium among hydride-forming metals stems from the ability to generate significantly higher hydrogen pressures than other hydriding metals.<sup>1</sup> In a next-generation target-filling design, a single palladium bed could replace the existing diaphragm compressor and condensation cell. Replacing these components with a single palladium bed allows for a smaller, simpler system with fewer moving parts. The high pressures achieved using the compressor can be achieved with a palladium bed by loading the bed at low temperature and subsequently raising the temperature to release the absorbed gas. In addition to next-generation target-filling systems, palladium is currently used in the isotope separator, which is deployed in the tritium laboratory. It has been extensively demonstrated that palladium has an affinity for lower mass hydrogen isotopes. The isotope separation system at LLE exploits this affinity to separate protium (H), deuterium (D), and tritium (T) in the fuel supply, allowing for specific DT mixtures to be made.

Currently in the literature, the pressure–composition–temperature (PCT) phase diagrams for the palladium hydride system extend only to 273 K. Measurement of the PCT diagram to cryogenic temperatures is necessary for the development of next-generation systems, which intend to employ palladium as a hydriding material. The focus of the current work is to measure the PCT curves at low temperatures for both protium and deuterium.

To measure the PCT curves for palladium hydride, a small getter bed containing 2.5 g of palladium powder was utilized. This bed is connected to a manifold of calibrated volumes, which can be charged with H<sub>2</sub> or D<sub>2</sub>. Absorption isotherms were measured by sequentially adding gas onto the bed from the charge volume. Hydrogen absorption onto palladium is rapid for all temperatures investigated. The data show that 99% of the gas is absorbed within 6 min.

To achieve temperatures between 130 and 240 K, a cryogenic cooler (“Q-Drive”) was purchased from Chart Industries. The Q-Drive operates using an acoustically driven Stirling cycle to remove heat from a cold head. The cold head of the Q-Drive was indirectly coupled to the exterior of the Pd bed through a multilam. This multilam was in contact with a stainless-steel rod that was in direct contact with the bottom of the Pd bed. Such a design protects the cold head during high-temperature excursions, while still maintaining the capability of subambient temperatures. Temperatures greater than ambient were set by using a heater that was wrapped around the exterior of the Pd bed.

Using the above procedure and experimental setup, the PCT curves were measured for protium and deuterium from 130 to 393 K. High-temperature ( $\geq 20^\circ\text{C}$ ) data were measured to compare with previously reported PCT curves, while low-temperature data have not been previously reported in the literature. The measured PCT curves are shown in Fig. 1 for (a) protium and (b) deuterium. In each panel, the equilibrium pressure of each isotope is plotted against the hydrogen-to-metal (HM) ratio for an array of temperatures. The measured PCT curves display the expected three-region trend with increasing hydrogen content: the pressure initially increases rapidly ( $\alpha$  phase), followed by a region of relatively little change in pressure (mixed  $\alpha$ – $\beta$  phase), and a second region of rapid pressure increases ( $\beta$  phase). The  $\alpha$  and the  $\beta$  phases correspond to hydrogen diffusion into either palladium or

palladium hydride, respectively. In between the  $\alpha$  and  $\beta$  phases, the mixed phase exists. Here, an increasing quantity of palladium hydride is formed with an increasing hydrogen-to-palladium ratio. In general, the maximum hydrogen-to-metal ratio increases as the temperature decreases. For temperatures  $\leq 20^\circ\text{C}$ , this maximum ratio is  $\sim 0.75$ . The onset of the mixed  $\alpha$ - $\beta$  phase begins at  $\text{HM} \sim 0.08$  for high-temperature isotherms and decreases to  $\sim 0.03$  at ambient temperatures before increasing again at very low temperatures to ratios between 0.1 and 0.2.

A van't Hoff plot for the current data set was constructed by using the equilibrium pressures and temperatures from the measured PCT curves shown in Fig. 1. The resulting van't Hoff plot is shown in Fig. 2, which includes the protium and deuterium results from this study, along with several data sets reported in the literature.<sup>2-4</sup> Finally, straight-line fits to each of the data

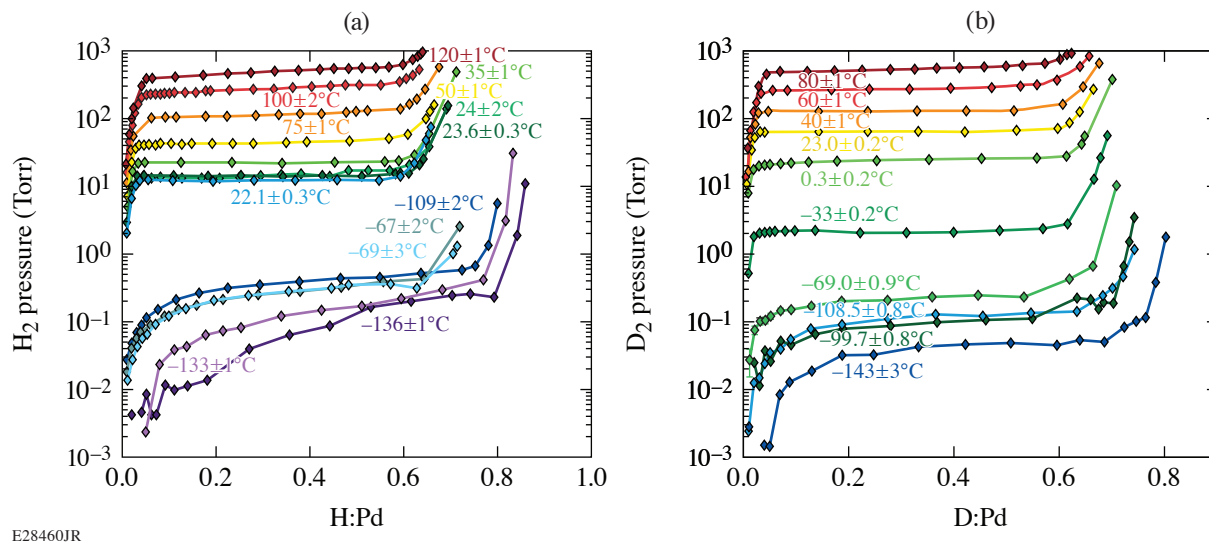


Figure 1 Pressure–composition–temperature isotherms measured using (a) hydrogen at temperatures between 296 K and 393 K and (b) deuterium at temperatures between 130 K and 353 K.

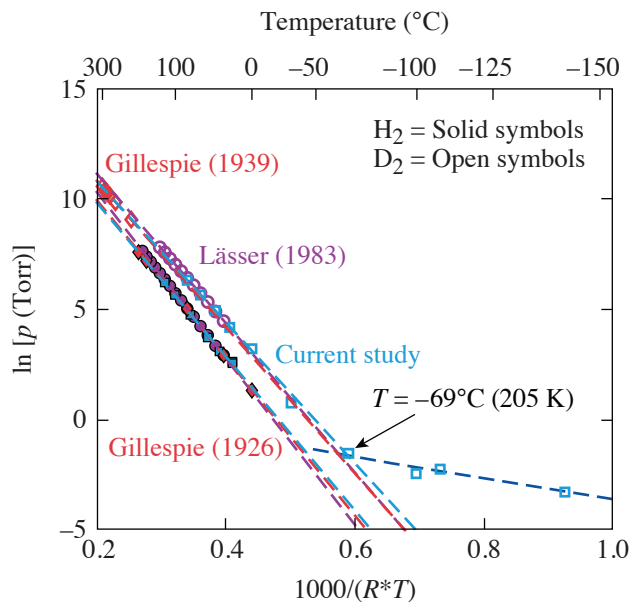


Figure 2 A van't Hoff diagram generated using equilibrium hydrogen (solid symbols) and deuterium (open symbols) pressures in the mixed region.

sets are shown as the dashed lines. The low-temperature data collected from the current work show a deviation from the high-temperature data; therefore, separate lines were fit to the low- and high-temperature data.

At low temperatures, palladium may absorb hydrogen by a mixed mechanism of hydride formation and physical adsorption. From the van't Hoff diagram (Fig. 2), a hydride forms until  $\sim 205$  K. Assuming no further hydride formation occurs with lower temperature, additional pressure reductions may be due to physical adsorption of hydrogen onto palladium. The expected hydride formation and physical adsorption regions are illustrated in Fig. 3. Here, the van't Hoff diagram is reproduced with data from the present work. The shaded areas show the expectation of where a hydride forms and where physical adsorption occurs.

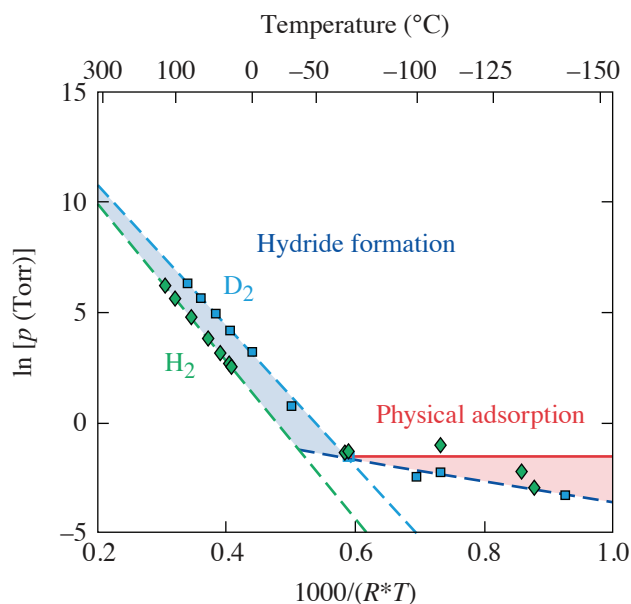


Figure 3

This van't Hoff diagram shows the different mechanisms for hydrogen absorption by palladium. The upper blue region corresponds to the pressures and temperatures at which palladium will form a hydride. The lower red region corresponds to the pressures and temperatures where hydrogen will physically adsorb onto the palladium surface.

This combination of mechanism and lower temperatures is justified by two observations: First, hydrogen and deuterium show similar equilibrium pressures at low temperatures. Similar pressures are not a result of the formation of a hydride since palladium has a greater affinity for less-massive isotopes. However, similar pressures may be a result of physical adsorption since the quantity of adsorbed gas depends primarily on the adsorbate and substrate sizes. Second, we estimate that all hydrogen loaded onto the palladium at low temperatures can be physically adsorbed into approximately six monolayers. For this estimation, it was assumed that a hydride is formed until 205 K. Below 205 K, any observed pressure reduction below the equilibrium pressure at 205 K represents hydrogen adsorbing onto the palladium's surface. Taking the "worst" case scenario, the difference between the equilibrium pressures at 205 K and 130 K is 0.174 Torr, which corresponds to  $1.9 \times 10^{-7}$  mol of H<sub>2</sub> or D<sub>2</sub>. Assuming the specific surface area is 2 m<sup>2</sup>/g, the total surface area is 5 m<sup>2</sup>. The number of H<sub>2</sub> molecules per monolayer is given by

$$\frac{1 \text{ H}_2}{\pi r^2} = 3.4 \times 10^{-5} \frac{\text{mol H}_2}{\text{m}^2 * \text{ML}}, \quad (1)$$

where  $r$  is the radius of a hydrogen molecule. Using the results of Eq. (1), the total surface area, and the total number of moles of adsorbed hydrogen, the number of monolayers is estimated to be  $10^{-3}$ . Such a small number of monolayers is reasonable at these low temperatures.

In summary, the palladium hydride and palladium deuteride isotherms have been measured from 130 K to 393 K. The data collected for temperatures below 273 K are the first to be reported in the literature. The measured isotherms show that an increasing quantity of palladium hydride is formed with decreasing temperatures, with a maximum hydrogen-to-metal ratio of 0.75.

These data are consistent with the literature, where the temperatures overlap. The van't Hoff diagram shows a deviation from high-temperature behavior for temperatures of less than 205 K. The data suggest that palladium can form a hydride until 205 K. Below this critical temperature, any further reduction in equilibrium pressure occurs due to physical adsorption onto the surface.

This material is based upon work supported by the Department of Energy National Nuclear Security Administration under Award Number DE-NA0003856, the University of Rochester, and the New York State Energy Research and Development Authority.

1. R. D. Penzhorn, M. Devillers, and M. Sirch, *J. Nucl. Mater.* **170**, 217 (1990).
2. L. J. Gillespie and F. P. Hall, *J. Am. Chem. Soc.* **48**, 1207 (1926).
3. L. J. Gillespie and W. R. Downs, *J. Am. Chem. Soc.* **61**, 2496 (1939).
4. R. Lässer and K.-H. Klatt, *Phys. Rev. B* **28**, 748 (1983).

# A Thin-Alumina Film as a Tritium Adsorption Inhibitor for Stainless-Steel 316

C. Fagan,<sup>1,2</sup> M. Sharpe,<sup>1</sup> W. T. Shmayda,<sup>1</sup> and W. U. Schröder<sup>1,2</sup>

<sup>1</sup>Laboratory for Laser Energetics, University of Rochester

<sup>2</sup>Department of Chemistry and Physics, University of Rochester

Thin coatings of Al<sub>2</sub>O<sub>3</sub> on stainless steel have been reported to suppress tritium permeation compared to uncoated steel.<sup>1–3</sup> However, these films are not dense; they contain microcracks, and have the potential for embedded water molecules in the film. Reducing the cracks in the alumina film may prove to further reduce permeation, and for surfaces with highly dense and uniform coatings, the permeation reduction may be improved substantially. Atomic layer deposition (ALD) is a vehicle to produce conformal, high-integrity films on hydroxylated surfaces with complex topographical features. Depositing alumina using trimethylaluminum and water is one of the most widely studied ALD reactions because of its viability as a high- $\kappa$  dielectric thin-film coating. ALD of Al<sub>2</sub>O<sub>3</sub> has been shown to produce conformal films with little to no surface defects as a result of the self-limiting reaction and monolayer growth mode. Atomic-layer-deposited alumina was used in this work to understand its effect on tritium absorption and to measure the tritium distribution in stainless-steel 316 (SS316) under the coating.

Samples of unmodified SS316 stock had approximately 0.86 mm of the surface machined away to remove any surface imperfections that can arise during manufacturing. These samples had an average surface roughness of 300±50 nm and are referred to from this point as 300-nm SS316. A subset of the 300-nm SS316 samples was mechanically polished to a high-mirror finish, where the average surface roughness was 5±1 nm, and is referred to as 5-nm SS316. Several polished samples were further treated by depositing 38.5±1 nm of Al<sub>2</sub>O<sub>3</sub> using the ALD process and an ozone pretreatment to enhance the reactivity of the native surface oxide to the ALD reactants. These samples are referred to as ALD and have the same surface roughness as the underlying polished samples (5±1 nm). All samples were exposed to 0.5 atm of tritium gas for 24 h at room temperature. Subsequently, the samples were removed and stored in an airtight storage pod under dry helium until retrieved for the experiment.

Temperature-programmed desorption was used to determine the total quantity of tritium retained by the stainless-steel samples. The tritiated sample is placed in an oven where dry argon is purged over the sample into one of two bubblers containing water. The sample is heated to 900±1° for several hours during which the desorbed tritium is transported by the dry argon into the bubblers. The primary tritium species (HTO) is captured in the first bubbler (capture efficiency >99%), and any carryover resulting from evaporation is captured in the second bubbler. After 3 h at room temperature, the sample is allowed to cool, and the quantity of desorbed tritium is determined using liquid scintillation counting (LSC) techniques. Tritium-concentration profiles in the deposited film and metal substrate were also measured using a combination of surface washes and acid etching of stainless steel. The surface wash and acid etching procedure are reported elsewhere.<sup>4,5</sup> The etching procedure for the samples coated with Al<sub>2</sub>O<sub>3</sub> was modified by using a selective NaOH etch that does not etch the steel substrate. The resulting solutions were neutralized to a pH = 0, mixed with an Ultima Gold<sup>TM</sup> liquid scintillation cocktail, and counted by LSC techniques using a low pH calibration curve.

The total quantity of adsorbed tritium indicates that the surface modification had influenced the total tritium adsorbed by the sample. The results of the TPD experiments are shown in Fig. 1. The data indicate that reducing the surface roughness by a factor of ~150 leads to a reduction in the total quantity of absorbed tritium, relative to the 300-nm SS316 samples. Similarly, the ALD-coated steel samples also see a decrease of ~27%. These data indicate that the ALD coating on the polished SS316 does not inhibit the absorption of tritium any further than the underlying polishing. This is likely caused by the large fraction

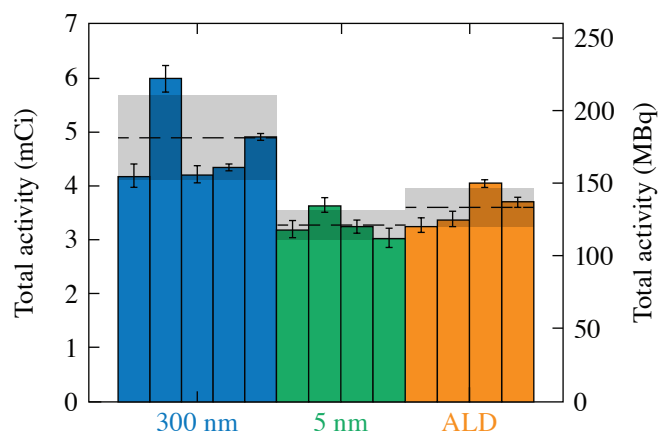


Figure 1  
TPD results for the unmodified (blue bars) and modified surfaces, 5-nm SS316 (green bars) and ALD (orange bars). Each bar represents an individual sample, with the mean as dashed lines and  $\pm 1\sigma$  indicated by the shaded region for each sample finish.

E28467JR

of  $\text{Al}(\text{OH})_2$  species present in the deposited film, which increases the total number of hydrogen binding sites relative to a pure  $\text{Al}_2\text{O}_3$  surface film. The increase in the hydroxyl density in the deposited film increases the apparent solubility of hydrogen in the film as a result of isotope exchange with hydrogen in the hydroxides. The TPD data give an insight into the total quantity of tritium in the samples; however, the data do not speak to the distribution of tritium in the metal.

The results of the selective etching for the ALD-coated steel are shown in Fig. 2. The data suggest that high concentrations of tritium exist in the  $\text{Al}_2\text{O}_3$  layers and that the concentration drops significantly at the steel interface. In the near-surface region ( $x < 1 \mu\text{m}$ ), the SS316 concentration is constant until a sharp drop is observed around 600 nm. To compare the concentration profiles of the ALD samples to the uncoated SS316 samples, the profiles for the uncoated steel (5 nm and 300 nm) are shifted by the alumina layer thickness (38 nm) in the concentration profile. The results show two large differences between the ALD and SS316 results. First, the ALD film contains less surface tritium compared to the uncoated samples. The second difference occurs in the near surface of the steel ( $\sim 700 \text{ nm}$ ). Here, the tritium concentration is  $200\times$  less in the ALD-coated sample relative to the uncoated SS316 sample. This suggests that tritium diffusion into the metal bulk is lowered by coating steel with alumina. Even though the 5 nm and ALD samples retained the same total quantity of tritium, the distribution of the tritium in the samples is quite different. Future work will focus on making the alumina layers more ideal to determine if these films can be used as a tritium diffusion barrier on SS316.

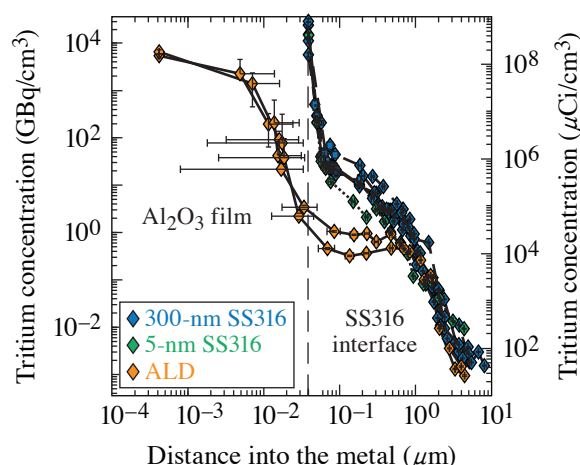


Figure 2  
Tritium concentration profiles for 300-nm SS316 (blue), 5-nm SS316 (green), and ALD  $\text{Al}_2\text{O}_3$  (orange) (Ref. 4). The uncoated samples are shifted to account for the deposited film on the ALD samples. The SS316 interface begins at the 38 nm and is indicated by the vertical dashed line.

E28467JR2

The authors acknowledge M. Koch, S. Scarantino, and B. Ruth (University of Rochester LLE Cryogenic Tritium Facility) for their work exposing the test samples to tritium gas. This material is based upon work supported by the Department of Energy National Nuclear Security Administration under Award Number DE-NA0003856, the University of Rochester, and the New York State Energy Research and Development Authority.

1. F. Yang *et al.*, *J. Nucl. Mater.* **478**, 144 (2016).
2. G. K. Zhang *et al.*, *Fusion Eng. Des.* **87**, 1370 (2012).
3. T. Wang *et al.*, *Fusion Eng. Des.* **85**, 1068 (2010).
4. M. Sharpe, C. Fagan, and W. T. Shmayda, "Distribution of Tritium in the Near Surface of 316 Stainless Steel," to be published in *Fusion Science and Technology*.
5. M. D. Sharpe *et al.*, *Fusion Eng. Des.* **130**, 76 (2018).

# FY19 Q3 Laser Facility Report

J. Puth, M. Labuzeta, and D. Canning

Laboratory for Laser Energetics, University of Rochester

During the third quarter (Q3) of FY19, the Omega Laser Facility conducted 357 target shots on OMEGA and 230 target shots on OMEGA EP for a total of 587 target shots (see Tables I and II). OMEGA averaged 11.6 target shots per operating day, averaging 91.7% Availability and 97.5% Experimental Effectiveness.

OMEGA EP was operated extensively in Q3 FY19 for a variety of user experiments. OMEGA EP averaged 7.9 target shots per operating day, averaging 96.7% Availability and 93.3% Experimental Effectiveness.

Additional neutron shielding is being added below the OMEGA target chamber to further limit background signal and noise on diagnostic measurements. The shielding will effectively minimize the size of the floor penetration required for cryogenic cart operations and reduce neutron scattering effects on diagnostics in the LaCave area. The shielding is being added in three phases to characterize the effectiveness and validate modeling (which will enhance calculations for future shielding design efforts). The final layer will be added in Q1 of FY20.

Table I: OMEGA Laser System target shot summary for Q3 FY19.

Program	Laboratory	Planned Number of Target Shots	Actual Number of Target Shots
ICF	LLE	82.5	99
ICF subtotal		82.5	99
HED	LLE	22	23
	LANL	44	52
	LLNL	38.5	47
	SNL	22	24
HED subtotal		126.5	146
CEA	CEA	11	13
RAL	RAL	11	9
LBS	LANL	11	10
	LLNL	33	38
	SLAC	11	13
LLE calibration	LLE	0	29
Grand total		286	357

Table II: OMEGA EP Laser System target shot summary for Q3 FY19.

Program	Laboratory	Planned Number of Target Shots	Actual Number of Target Shots
ICF	LLE	49	69
	LLNL	21	30
	NRL	7	6
ICF subtotal		77	105
HED	LLE	14	17
	LANL	7	7
	LLNL	21	25
HED subtotal		42	49
LBS	LLE	14	19
	LLNL	14	25
	SLAC	7	7
LLE calibration	LLE	0	12
Grand total		161	230



## Publications and Conference Presentations

### Publications

- R. Adam, G. Chen, D. E. Bürgler, T. Shou., I. Komissarov, S. Heidtfield, H. Hardtdegen, M. Mikulics, C. M. Schneider, and R. Sobolewski, “Magnetically and Optically Tunable Terahertz Radiation from Ta/NiFe/Pt Spintronic Nanolayers Generated by Femtosecond Laser Pulses,” *Appl. Phys. Lett.* **114**, 212405 (2019).
- X. Bian and H. Aluie, “Decoupled Cascades of Kinetic and Magnetic Energy in Magnetohydrodynamic Turbulence,” *Phys. Rev. Lett.* **122**, 135101 (2019).
- D. Broege and J. Bromage, “Measurements of Heat Flow from Surface Defects in Lithium Triborate,” *Opt. Express* **27**, 10,067 (2019).
- D. Broege, S. Fochs, G. Brent, J. Bromage, C. Dorrer, R. F. Earley, M. J. Guardalben, J. A. Marozas, R. G. Roides, D. Weiner, J. Sethian, X. Wang, D. Weiner, J. Zweiback, and J. D. Zuegel, “The Dynamic Compression Sector Laser: A 100-J UV Laser for Dynamic Compression Research,” *Rev. Sci. Instrum.* **90**, 053001 (2019).
- A. Chien, L. Gao, H. Ji, X. Yuan, E. G. Blackman, H. Chen, P. C. Efthimion, G. Fiksel, D. H. Froula, K. W. Hill, K. Huang, Q. Lu, J. D. Moody, and P. M. Nilson, “Study of Magnetically Driven Reconnection Platform Using Ultrafast Proton Radiography,” *Phys. Plasmas* **26**, 062113 (2019).
- D. T. Cliche and R. C. Mancini, “Impact of 3D Effects on the Characteristics of a Multi-Monochromatic X-Ray Imager,” *Appl. Opt.* **58**, 4753 (2019).
- A. L. Coleman, M. G. Gorman, R. Briggs, R. S. McWilliams, D. McGonegle, C. A. Bolme, A. E. Gleason, D. E. Fratanduono, R. F. Smith, E. Galtier, H. J. Lee, B. Nagler, E. Granados, G. W. Collins, J. H. Eggert, J. S. Wark, and M. I. McMahon, “Identification of Phase Transitions and Metastability in Dynamically Compressed Antimony Using Ultrafast X-Ray Diffraction,” *Phys. Rev. Lett.* **122**, 255704 (2019).
- A. S. Davies, D. Haberberger, J. Katz, S. Bucht, J. P. Palastro, W. Rozmus, and D. H. Froula, “Picosecond Thermodynamics in Underdense Plasmas Measured with Thomson Scattering,” *Phys. Rev. Lett.* **122**, 155001 (2019).
- J. A. Delettrez, T. J. B. Collins, and C. Ye, “Determining Acceptable Limits of Fast-Electron Preheat in Direct-Drive-Ignition-Scale Target Designs,” *Phys. Plasmas* **26**, 062705 (2019).
- S. G. Demos, B. N. Hoffman, C. W. Carr, D. A. Cross, R. A. Negres, and J. D. Bude, “Mechanisms of Laser-Induced Damage in Absorbing Glasses with Nanosecond Pulses,” *Opt. Express* **27**, 9975 (2019).
- C. A. Di Stefano, F. W. Doss, A. M. Rasmus, K. A. Flippo, and B. M. Haines, “The Modeling of Delayed-Onset Rayleigh–Taylor and Transition to Mixing in Laser-Driven HED Experiments,” *Phys. Plasmas* **26**, 052708 (2019).
- L. Divol, D. P. Turnbull, T. Chapman, C. Goyon, and P. Michel, “An Analytical Study of Non-Resonant Transient Cross-Beam Power Transfer Relevant to Recent Progress in Plasma Photonics,” *Phys. Plasmas* **26**, 043101 (2019).
- A. Fernandez-Pañella, M. Millot, D. E. Fratanduono, M. P. Desjarlais, S. Hamel, M. C. Marshall, D. J. Erskine, P. A. Sterne, S. Haan, T. R. Boehly, G. W. Collins, J. H. Eggert, and P. M. Celliers, “Shock Compression of Liquid Deuterium up to 1 TPa,” *Phys. Rev. Lett.* **122**, 255702 (2019).
- R. K. Follett, J. G. Shaw, J. F. Myatt, C. Dorrer, D. H. Froula, and J. P. Palastro, “Thresholds of Absolute Instabilities Driven by a Broadband Laser,” *Phys. Plasmas* **26**, 062111 (2019).
- C. G. R. Geddes and J. L. Shaw, “Summary of Working Group 1: Laser-Plasma Wakefield Acceleration,” in *2018 IEEE Advanced Accelerator Concepts Workshop (AAC 2018)* (IEEE, New York, 2018), pp. 1–5.

- R. Ghosh, O. Swart, S. Westgate, B. L. Miller, and M. Z. Yates, "Antibacterial Copper–Hydroxyapatite Composite Coatings via Electrochemical Synthesis," *Langmuir* **35**, 5957 (2019).
- M. R. Gomez, S. A. Slutz, P. F. Knapp, K. D. Hahn, M. R. Weis, E. C. Harding, M. Geissel, J. R. Fein, M. E. Glinsky, S. B. Hansen, A. J. Harvey-Thompson, C. A. Jennings, I. C. Smith, D. Woodbury, D. J. Ampleford, T. J. Awe, G. A. Chandler, M. H. Hess, D. C. Lamppa, C. E. Myers, C. L. Ruiz, A. B. Sefkow, J. Schwarz, D. A. Yager-Elorriaga, B. Jones, J. L. Porter, K. J. Peterson, R. D. McBride, G. A. Rochau, and D. B. Sinars, "Assessing Stagnation Conditions and Identifying Trends in Magnetized Liner Inertial Fusion," *IEEE Trans. Plasma Sci.* **47**, 2081 (2019).
- P.-A. Gourdain, M. B. Adams, M. Evans, H. R. Hasson, R. V. Shapovalov, J. R. Young, and I. West-Abdallah, "Enhancing Cylindrical Compression by Reducing Plasma Ablation in Pulsed-Power Drivers," *Phys. Plasmas* **26**, 042706 (2019).
- H. Habara, T. Iwawaki, T. Gong, M. S. Wei, S. T. Ivancic, W. Theobald, C. M. Krauland, S. Zhang, G. Fiksel, and K. A. Tanaka, "A Ten-Inch Manipulator (TIM) Based Fast-Electron Spectrometer with Multiple Viewing Angles (OU-ESM)," *Rev. Sci. Instrum.* **90**, 063501 (2019).
- V. V. Ivanov, A. V. Maximov, R. Betti, L. S. Leal, R. C. Mancini, K. J. Swanson, I. E. Golovkin, C. J. Fontes, H. Sawada, A. B. Sefkow, and N. L. Wong, "Study of Laser Produced Plasma in a Longitudinal Magnetic Field," *Phys. Plasmas* **26**, 062707 (2019).
- T. R. Joshi, S. C. Hsu, P. Hakel, N. M. Hoffman, H. Sio, and R. C. Mancini, "Progress on Observations of Interspecies Ion Separation in Inertial-Confinement-Fusion Implosions via Imaging X-Ray Spectroscopy," *Phys. Plasmas* **26**, 062702 (2019).
- K. R. P. Kafka and S. G. Demos, "Interaction of Short Laser Pulses with Model Contamination Microparticles on a High Reflector," *Opt. Lett.* **44**, 1844 (2019).
- V. V. Karasiev, S. X. Hu, M. Zaghoo, and T. R. Boehly, "Exchange-Correlation Thermal Effects in Shocked Deuterium: Softening the Principal Hugoniot and Thermophysical Properties," *Phys. Rev. B* **99**, 214110 (2019).
- V. V. Karasiev, S. B. Trickey, and J. W. Dufty, "Status of Free-Energy Representations for the Homogeneous Electron Gas," *Phys. Rev. B* **99**, 195134 (2019).
- A. Lees and H. Aluie, "Baropycnal Work: A Mechanism for Energy Transfer Across Scales," *Fluids* **4**, 92 (2019).
- S. LePape, L. Divol, A. MacPhee, J. McNaney, M. Hohenberger, D. Froula, V. Glebov, O. L. Landen, C. Stoeckl, E. Dewald, S. Khan, C. Yeamans, P. Michel, M. Schneider, J. Knauer, J. Kilkenny, and A. J. Mackinnon, "Optimization of High Energy X-Ray Production Through Laser Plasma Interaction," *High Energy Density Phys.* **31**, 13 (2019).
- M. J.-E. Manuel, A. B. Sefkow, C. C. Kuranz, A. M. Rasmus, S. R. Klein, M. J. MacDonald, M. R. Trantham, J. R. Fein, P. X. Belancourt, R. P. Young, P. A. Keiter, B. B. Pollock, J. Park, A. U. Hazi, G. J. Williams, H. Chen, and R. P. Drake, "Magnetized Disruption of Inertially Confined Plasma Flows," *Phys. Rev. Lett.* **122**, 225001 (2019).
- P.-E. Masson-Laborde, S. Laffite, C. K. Li, S. C. Wilks, R. Riquier, R. D. Petrasso, G. Kluth, and V. Tassin, "Interpretation of Proton Radiography Experiments of Hohlräume with Three-Dimensional Simulations," *Phys. Rev. E* **99**, 053207 (2019).
- M. Millot, F. Coppari, J. R. Rygg, A. Correa Barrios, S. Hamel, D. C. Swift, and J. H. Eggert, "Nanosecond X-Ray Diffraction of Shock-Compressed Superionic Water Ice," *Nature* **569**, 251 (2019).
- S. Papernov, "Spectroscopic Setup for Submicrometer-Resolution Mapping of Low-Signal Absorption and Luminescence Using Photothermal Heterodyne Imaging and Photon-Counting Techniques," *Appl. Optics* **58**, 3908 (2019).
- J. L. Peebles, S. X. Hu, W. Theobald, V. N. Goncharov, N. Whiting, P. M. Celliers, S. J. Ali, G. Duchateau, E. M. Campbell, T. R. Boehly, and S. P. Regan, "Direct-Drive Measurements of Laser-Imprint-Induced Shock Velocity Nonuniformities," *Phys. Rev. E* **99**, 063208 (2019).
- A. M. Rasmus, C. A. Di Stefano, K. A. Flippo, F. W. Doss, C. F. Kawaguchi, J. L. Kline, E. C. Merritt, T. R. Desjardins, T. Cardenas, D. W. Schmidt, P. M. Donovan, F. Fierro, L. A. Goodwin, J. I. Martinez, T. E. Quintana, J. S. Zingale, and C. C. Kuranz, "Shock-Driven Hydrodynamic Instability of a Sinusoidally Perturbed, High-Atwood Number, Oblique Interface," *Phys. Plasmas* **26**, 062103 (2019).
- S. Sampat, T. Z. Kosc, K. A. Bauer, R. D. Dean, W. R. Donaldson, J. Kwiatkowski, R. Moshier, A. L. Rigatti, M. H.

Romanofsky, L. J. Waxer, and J. H. Kelly, “Power Balancing a Multibeam Laser,” *Proc. SPIE* **10898**, 108980A (2019).

J. P. Sauppe, B. M. Haines, S. Palaniyappan, P. A. Bradley, S. H. Batha, E. N. Loomis, and J. L. Kline, “Modeling of Direct-Drive Cylindrical Implosion Experiments with an Eulerian Radiation-Hydrodynamics Code,” *Phys. Plasmas* **26**, 042701 (2019).

D. B. Schaeffer, W. Fox, R. K. Follett, G. Fiksel, C. K. Li, J. Matteucci, A. Bhattacharjee, and K. Germaschewski, “Direct

Observations of Particle Dynamics in Magnetized Collisionless Shock Precursors in Laser-Produced Plasmas,” *Phys. Rev. Lett.* **122**, 245001 (2019).

S. Zhang, A. Lazicki, B. Militzer, L. H. Yang, K. Caspersen, J. A. Gaffney, M. W. Däne, J. E. Pask, W. R. Johnson, A. Sharma, P. Suryanarayana, D. D. Johnson, A. V. Smirnov, P. A. Sterne, D. Erskine, R. A. London, F. Coppari, D. Swift, J. Nilsen, A. J. Nelson, and H. D. Whitley, “Equation of State of Boron Nitride Combining Computation, Modeling, and Experiment,” *Phys. Rev. B* **99**, 165103 (2019).

### Forthcoming Publications

S. Bucht, D. Haberberger, J. Bromage, and D. H. Froula, “A Methodology for Designing Grism Stretchers for Idler-Based Optical Parametric Chirped-Pulse-Amplification Systems,” to be published in the *Journal of the Optical Society of America B*.

D. Cao, R. C. Shah, S. P. Regan, R. Epstein, I. V. Igumenshchev, V. Gopalaswamy, A. R. Christopherson, W. Theobald, P. B. Radha, and V. N. Goncharov, “Interpreting the Electron Temperature Inferred from X-Ray Continuum Emission for Direct-Drive Inertial Confinement Fusion Implosions on OMEGA,” to be published in *Physics of Plasmas*.

A. Colaïtis, R. K. Follett, J. P. Palastro, I. Igumenshchev, and V. Goncharov, “Adaptive Inverse Ray-Tracing for Accurate and Efficient Modeling of Cross Beam Energy Transfer in Hydrodynamics Simulations,” to be published in *Physics of Plasmas*.

S. G. Demos, J. C. Lambropoulos, R. A. Negres, M. J. Matthews, and S. R. Qiu, “Dynamics of Secondary Contamination from the Interaction of High-Power Laser Pulses with Metal Particles Attached on the Input Surface of Optical Components,” to be published in *Optics Express*.

C. Dorrer, “Spatiotemporal Metrology of Broadband Optical Pulses,” to be published in *IEEE Journal on Selected Topics in Quantum Electronics*.

G. Duchateau, S. X. Hu, A. Pineau, A. Kar, B. Chimier, A. Casner, V. Tikhonchuk, V. N. Goncharov, P. B. Radha, and E. M. Campbell, “Modeling the Solid-to-Plasma Transition for Laser Imprinting in Direct-Drive Inertial Confinement Fusion,” to be published in *Physical Review E*.

C. Fagan, M. Sharpe, W. T. Shmayda, and W. U. Schröder, “Tritium Retention in Hexavalent Chromate-Conversion-Coated Aluminum Alloy,” to be published in *Fusion Science and Technology*.

C. J. Forrest, A. Deltuva, W. U. Schröder, A. Voinov, J. P. Knauer, E. M. Campbell, G. W. Collins, V. Yu. Glebov, O. M. Mannion, Z. Mohamed, P. B. Radha, S. P. Regan, T. C. Sangster, and C. Stoeckl, “Deuteron Breakup Induced by 14-MeV Neutrons from Inertial Confinement Fusion,” to be published in *Physical Review C*.

L. Guazzotto and R. Betti, “Two-Fluid Burning-Plasma Analysis for Magnetic Confinement Fusion Devices,” to be published in *Plasma Physics and Controlled Fusion*.

I. V. Igumenshchev, A. L. Velikovich, V. N. Goncharov, R. Betti, E. M. Campbell, J. P. Knauer, S. P. Regan, A. J. Schmitt, R. C. Shah, and A. Shvydky, “Rarefaction Flows and Mitigation of Imprint in Direct-Drive Implosions,” to be published in *Physical Review Letters*.

C. K. Li, V. T. Tikhonchuk, Q. Moreno, H. Sio, E. D’Humières, X. Ribeyre, Ph. Korneev, S. Atzeni, R. Betti, A. Birkel, E. M. Campbell, R. K. Follett, J. A. Frenje, S. X. Hu, M. Koenig, Y. Sakawa, T. C. Sangster, F. H. Séguin, H. Takabe, S. Zhang, and R. D. Petrasso, “Collisionless Shocks Driven by Supersonic Plasma Flows with Self-Generated Magnetic Fields,” to be published in *Physical Review Letters*.

C. A. McCoy, M. C. Marshall, D. N. Polsin, D. E. Fratanduono, P. M. Celliers, D. D. Meyerhofer, and T. R. Boehly, “Hugoniot, Sound Velocity, and Shock Temperature of MgO to 2300 GPa,” to be published in *Physical Review B*.

S. C. Miller, J. P. Knauer, C. J. Forrest, V. Yu. Glebov, P. B. Radha, and V. N. Goncharov, "Fuel–Shell Interface Instability Growth Effects on the Performance of Room Temperature Direct-Drive Implosions," to be published in *Physics of Plasmas*.

B. W. Plansinis, W. R. Donaldson, and G. P. Agrawal, "A Time-to-Frequency Converter for Measuring the Shape of Short Optical Pulses," to be published in *Review of Scientific Instruments*.

B. Rice, J. Ulreich, and M. J. Shoup III, "Prediction of Deuterium–Tritium Ice Layer Uniformity in Direct-Drive Confinement Fusion Target Capsules," to be published in the *Proceedings of NAFEMS World Congress 2019*.

E. Ruskov, V. Yu. Glebov, T. W. Darling, F. J. Wessel, F. Conti, J. C. Valenzuela, H. U. Rahman, and F. N. Beg, "Gated Liquid Scintillator Detector for Neutron Time of Flight Measurements in a Gas-Puff Z-Pinch Experiment," to be published in *Review of Scientific Instruments*.

B. Scheiner, M. J. Schmitt, S. C. Hsu, D. Schmidt, J. Mance, C. Wilde, D. N. Polsin, T. R. Boehly, F. J. Marshall, N. Krasheninnikova, K. Molvig, and H. Huang, "First Experiments on *Revolver* Shell Collisions at the OMEGA Laser," to be published in *Physics of Plasmas*.

R. V. Shapovalov, G. Brent, R. Moshier, M. J. Shoup III, R. B. Spielman, and P.-A. Gourdain, "The Design of 30-T Pulsed

Magnetic Field Generator for Magnetized High-Energy-Density Plasma Experiments," to be published in *Physical Review Accelerators and Beams*.

M. Sharpe and C. Fagan, W. T. Shmayda, "Distribution of Tritium in the Near Surface of 316 Stainless Steel," to be published in *Fusion Science and Technology*.

H. Sio, O. Larroche, S. Atzeni, N. V. Kabadi, J. A. Frenje, M. Gatun Johnson, C. Stoeckl, C. Li, C. J. Forrest, V. Glebov, P. J. Adrian, A. Bose, A. Birkel, S. P. Regan, F. H. Séguin, and R. D. Petrasso, "Probing Ion Species Separation and Ion Thermal Decoupling in Shock-Driven Implosions Using Multiple Nuclear Reaction Histories," to be published in *Physics of Plasmas*.

R. Sobolewski, "Optical Sensors," to be published in the *Handbook of Superconducting Materials*.

C. Stoeckl, C. J. Forrest, V. Yu. Glebov, S. P. Regan, T. C. Sangster, W. U. Schröder, A. Schwemmlin, and W. Theobald, "A Platform for Nuclear Physics Experiments with Laser-Accelerated Light Ions," to be published in *Nuclear Instruments and Methods in Physics Research B*.

M. Stoeckl and A. A. Solodov, "Refining Instrument Response Functions with 3-D Monte Carlo Simulations of Differential Hard X-Ray Spectrometers," to be published in *Nuclear Instruments and Methods in Physics Research A*.

---

### Conference Presentations

---

J. Bromage, A. Agliata, S.-W. Bahk, M. Bedzyk, I. A. Begishev, W. A. Bittle, T. Buczek, J. Bunkenburg, D. Canning, A. Consentino, D. Coppenbarger, R. Cuffney, C. Dorrer, C. Feng, D. H. Froula, G. Gates, M. J. Guardalben, D. Haberberger, S. Hadrich, C. Hall, B. N. Hoffman, R. K. Jungquist, T. J. Kessler, E. Kowaluk, B. E. Kruschwitz, T. Lewis, J. Magoon, D. D. Meyerhofer, C. Mileham, M. Millecchia, S. F. B. Morse, P. M. Nilson, J. B. Oliver, R. G. Peck, A. L. Rigatti, H. Rinderknecht, R. G. Roides, M. H. Romanofsky, J. Rothhardt, E. M. Schiesser, K. Shaughnessy, M. J. Shoup III, C. Smith, M. Spilatro, C. Stoeckl, R. Taylor, B. Wager, L. J. Waxer, B. Webb, D. Weiner, and J. D. Zuegel, "Laser Technology Development for Ultra-Intense Optical Parametric Chirped-Pulse Amplification," presented at *Optics and Optoelectronics 2019*, Prague, Czech Republic, 1–4 April 2019.

G. W. Collins, J. R. Rygg, T. R. Boehly, M. Zaghou, D. N. Polsin, B. J. Henderson, X. Gong, L. Crandall, R. Saha, J. J. Ruby, G. Tabak, M. Huff, Z. K. Sprowal, D. A. Chin, M. K. Ginnane, P. M. Celliers, J. H. Eggert, A. Lazicki, R. F. Smith, R. Hemley, F. Coppari, B. Bachmann, J. Gaffney, D. E. Fratanduono, D. G. Hicks, Y. Ping, D. Swift, D. G. Braun, S. Hamel, M. Millot, M. Gorman, R. Briggs, S. Ali, R. Kraus, M. McMahon, P. Loubeyre, S. Brygoo, R. Jeanloz, R. Falcone, F. N. Beg, C. Bolme, A. Gleason, S. H. Glenzer, H. Lee, T. Duffy, J. Wang, J. Wark, and G. Gregori, "Extreme Matters: Pressure to Explore New Worlds and Exotic Solids," presented at the 2019 Mach Conference, Annapolis, MD, 3–5 April 2019.

---

The following presentations were made at CEIS 2019, Rochester, NY, 4 April 2019:

W. R. Donaldson and Y. Zhao, “Picosecond UV Photodiodes.”

A. Stenson, G. Chen, Y. Akbas, I. Komissarov, R. Sobolewski, A. Jafari-Salim, and O. Mukhanov, “Superconducting Single-Photon Detectors as Smart Sensors.”

E. M. Campbell, “Laser-Direct-Drive Status and Future Plans,” presented at MIT, Cambridge, MA, 5 April 2019.

The following presentations were made at the 15th Direct-Drive and Fast-Ignition Workshop, Rome, Italy, 8–10 April 2019:

R. Betti, V. Gopalaswamy, J. P. Knauer, N. Luciani, D. Patel, K. M. Woo, A. Bose, I. V. Igumenshchev, E. M. Campbell, K. S. Anderson, K. A. Bauer, M. J. Bonino, D. Cao, A. R. Christopherson, G. W. Collins, T. J. B. Collins, J. R. Davies, J. A. Delettrez, D. H. Edgell, R. Epstein, C. J. Forrest, D. H. Froula, V. Yu. Glebov, V. N. Goncharov, D. R. Harding, S. X. Hu, D. W. Jacobs-Perkins, R. T. Janezic, J. H. Kelly, O. M. Mannion, A. V. Maximov, F. J. Marshall, D. T. Michel, S. Miller, S. F. B. Morse, J. P. Palastro, J. L. Peebles, P. B. Radha, S. P. Regan, S. Sampat, T. C. Sangster, A. B. Sefkow, W. Seka, R. C. Shah, W. T. Shmayda, A. Shvydky, C. Stoeckl, A. A. Solodov, W. Theobald, and J. D. Zuegel, “Progress Toward Demonstrating Hydro-Equivalent Ignition with Direct-Drive Inertial Confinement Fusion.”

V. N. Goncharov, “Acoustic Trapping and Perturbation Amplification in Nested Rarefaction Waves.”

J. P. Palastro, R. K. Follett, D. Turnbull, C. Dorrer, E. M. Hill, L. Nguyen, A. S. Davies, A. M. Hansen, R. J. Henchen, A. Milder, A. A. Solodov, A. Shvydky, J. Bromage, V. N. Goncharov, D. H. Froula, J. Bates, J. L. Weaver, S. Obenschain, and A. Colaitis, “Expanding the Inertial Confinement Fusion Design Space with Broadband Mitigation of Laser–Plasma Instabilities.”

S. P. Regan, V. N. Goncharov, T. C. Sangster, R. Betti, E. M. Campbell, K. A. Bauer, T. R. Boehly, M. J. Bonino, D. Cao, A. R. Christopherson, G. W. Collins, T. J. B. Collins, R. S. Craxton, D. H. Edgell, R. Epstein, C. J. Forrest, R. K. Follett, J. A. Frenje, D. H. Froula, V. Yu. Glebov, V. Gopalaswamy, D. R. Harding, S. X. Hu, I. V. Igumenshchev, S. T. Ivancic, D. W. Jacobs-Perkins, R. T. Janezic, J. H. Kelly, M. Karasik, T. J. Kessler, J. P. Knauer, T. Z. Kosc, O. M. Mannion, J. A. Marozas, F. J. Marshall, P. W. McKenty, Z. Mohamed, S. F. B. Morse, P. M. Nilson, J. P.

Palastro, R. D. Petrasso, D. Patel, J. L. Peebles, P. B. Radha, H. G. Rinderknecht, M. J. Rosenberg, S. Sampat, W. Seka, R. C. Shah, J. R. Rygg, J. G. Shaw, W. T. Shmayda, M. J. Shoup III, A. Shvydky, A. A. Solodov, C. Sorce, C. Stoeckl, W. Theobald, D. Turnbull, J. Ulreich, M. D. Wittman, K. M. Woo, J. D. Zuegel, J. A. Frenje, M. Gatu Johnson, R. D. Petrasso, M. Karasik, S. P. Obenschain, and A. J. Schmitt, “Multidimensional Effects on Hot-Spot Formation in OMEGA DT Cryogenic Implosions.”

E. M. Campbell, “Fusion: Making a Star on Earth and the Quest for the Ultimate Energy Source to Power the Planet,” presented at Torch Club, Rochester, NY, 9 April 2019.

E. M. Campbell, “Laser-Direct-Drive Status and Future Plans,” presented at Washington State University, Pullman, WA, 11 April 2019.

The following presentations were made at the APS April Meeting 2019, Denver, CO, 13–16 April 2019:

C. J. Forrest, J. P. Knauer, E. M. Campbell, G. W. Collins, V. Yu. Glebov, O. M. Mannion, Z. Mohamed, P. B. Radha, S. P. Regan, T. C. Sangster, C. Stoeckl, A. Deltuva, and W. U. Schröder, “Neutron-Induced Breakup of Deuterium at 14 MeV.”

A. Schwemmlin, W. U. Schröder, C. Stoeckl, C. J. Forrest, V. Yu. Glebov, S. P. Regan, T. C. Sangster, W. Theobald, “Using the OMEGA EP Laser for Nuclear Experiments at LLE.”

G. W. Collins, “Extreme Matters: Pressure to Explore New Worlds and Exotic Solids,” presented at the Materials Science and Engineering Colloquium, New York, NY, 19 April 2019.

The following presentations were made at the 12th International Conference on Tritium Science and Technology, Busan, Korea, 22–26 April 2019:

C. Fagan, M. Sharpe, W. T. Shmayda, and W. U. Schröder, “Thin-Alumina Film as a Tritium Adsorption Inhibitor for Stainless-Steel 316.”

M. D. Sharpe, K. Glance, and W. T. Shmayda, "Measurement of Palladium Hydride and Palladium Deuteride Isotherms Between 130 and 393 K."

W. T. Shmayda, M. D. Sharpe, C. Fagan, M. D. Wittman, R. F. Earley, and N. P. Redden, "Tritium Activities at the University of Rochester's Laboratory for Laser Energetics."

---

The following presentations were made at the Target Fabrication Meeting 2019, Annapolis, MD, 23–26 April 2019:

M. J. Bonino, D. R. Harding, W. Sweet, M. Schoff, A. Greenwood, N. Satoh, M. Takagi, and A. Nikroo, "Properties of Vapor-Deposited and Solution-Processed Targets for Laser-Driven Inertial Confinement Fusion Experiments."

T. Cracium, M. J. Bonino, L. Crandall, B. J. Henderson, J. J. Ruby, J. R. Rygg, J. L. Peebles, M. Huff, X. Gong, D. N. Polsin, D. A. Chin, and M. K. Ginnane, "High-Energy-Density Target Production at LLE."

A. Lighty and D. R. Harding, "Using a Liquid–Liquid Extraction Technique to Reduce the Number and Size of Vacuoles in Polystyrene Films."

J. L. Shaw, D. Wasilewski, D. R. Harding, Z. Barfield, D. Haberberger, A. M. Hansen, J. Katz, D. Mastro Simone, D. H. Froula, P. Fan, Y. Lu, J. Campbell, J. P. Sauppe, and K. A. Flippo, "Targets for Underdense Plasma Studies at the Laboratory for Laser Energetics."

D. W. Turner, M. J. Bonino, T. Cracium, J. L. Peebles, J. Streit, and J. Hund, "Manufacture of Targets for Magnetized Liner Inertial Fusion Campaigns on the OMEGA-60 Laser System."

D. Wasilewski, D. R. Harding, J. L. Shaw, Y. Lu, P. Fan, and J. Campbell, "Methods for Removing Fragile Printed-Foam Structures from Their Substrates."

M. D. Wittman, D. R. Harding, N. P. Redden, J. Ulreich, R. Chapman, and L. Carlson, "Progress on Filling and Layering DT-Filled Fill-Tube Capsules for OMEGA Experiments."

---

S.-W. Bahk, "Programmable Beam-Shaping System for High Power Laser Systems," presented at the RIT Center for Imaging Science Seminar, Rochester, NY, 24 April 2019.

---

The following presentations were made at the Omega Laser Facility Users Group Workshop, Rochester, NY, 24–26 April 2019:

M. Barczys, R. Brown, D. Canning, A. Consentino, D. Coppenbarger, M. J. Guardalben, E. M. Hill, T. Z. Kosc, B. E. Kruschwitz, R. Russo, M. Spilatro, A. Szydlowski, and L. J. Waxer, "Advancements in Pulse Shaping on OMEGA EP."

K. A. Bauer, L. J. Waxer, M. Heimbueger, J. H. Kelly, J. Kwiatkowski, S. F. B. Morse, D. Nelson, S. Sampat, and D. Weiner, "Comparison of On-Shot, In-Tank, and Equivalent-Target-Plane Measurements of the OMEGA Laser System Focal Spot."

J. Bromage, "Capabilities and Future Prospects for the Multi-Terawatt (MTW) Laser Facility at LLE."

K. M. Glance, W. T. Shmayda, and M. D. Sharpe, "Using Palladium Hydride to Fill Inertial Confinement Fusion Targets."

Z. L. Mohamed, J. P. Knauer, C. J. Forrest, and M. Gatun Johnson, "Wave-Function Amplitude Analysis of the <sup>5</sup>He Resonance in the TT Neutron Spectrum."

S. F. B. Morse, "Omega Facility OLUG 2019 Update: Progress on Recommendations and Items of General Interest."

H. G. Rinderknecht, "Summary of the EP OPAL Workshop."

A. Sharma and R. S. Craxton, "Optimization of Cone-In-Shell Targets for an X-Ray Backlighter at the National Ignition Facility."

A. Sorce, J. Kendrick, D. Weiner, T. R. Boehly, J. R. Rygg, M. K. Ginnane, J. Zou, A. Liu, and M. Couch, "Recent Upgrades to the Omega Laser Facility's VISAR and SOP Diagnostics."

C. Sorce, "Gas-Jet System on OMEGA and OMEGA EP."

---

A. J. Howard, D. Turnbull, A. S. Davies, P. Franke, D. H. Froula, and J. P. Palastro, “Photon Acceleration in a Flying Focus,” presented at Design Day, Rochester, NY, 2 May 2019.

V. V. Karasiev and S. X. Hu, “Development of Finite-T Exchange-Correlation Functionals: Improving Reliability for WDM Applications,” presented at the 10th International Workshop on Warm Dense Matter, Travemünde, Germany, 5–9 May 2019 (invited).

The following presentations were made at CLEO 2019, San Jose, CA, 5–10 May 2019:

S. Bucht, D. Haberberger, J. Bromage, and D. H. Froula, “Designing Grism Stretcher for Idler-Based Optical Parametric Chirped-Pulse–Amplification Systems.”

Y. Zhao and W. R. Donaldson, “Ultrafast AlGa<sub>N</sub> UV Photodetectors with Picoseconds Response.”

J. L. Shaw, J. P. Palastro, D. Turnbull, T. J. Kessler, A. Davies, P. Franke, A. Howard, L. Nguyen, D. Ramsey, G. W. Jenkins, S.-W. Bahk, I. A. Begishev, R. Boni, J. Bromage, S. Bucht, R. K. Follett, D. Haberberger, J. Katz, F. A. Hegmann, D. Purshchke, N. Vafaei-Najafabadi, J. Vieira, and F. Quere, “Flying Focus and Its Application to Laser-Plasma Accelerators,” presented at the Laser-Plasma Accelerator Workshop, Split, Croatia, 5–10 May 2019 (invited).

The following presentations were made at the UBUR Superconductivity Workshop, Buffalo, 10 May 2019:

W. R. Donaldson, “Measuring Optically Activated Transient Superconductivity Events at LLE.”

J. R. Rygg, “Tutorial: High Pressure Physics.”

M. Zaghoo, “Capabilities and Techniques for Diamond Anvil Cells.”

H. G. Rinderknecht, “Frontiers in Ultrahigh Intensity and Relativistic Physics Enabled by an Optical Parametric Amplifier Laser (EP OPAL) Facility,” presented at Plasma Physics Town Hall Meeting, Rochester, NY, 16 May 2019.

R. Epstein, “Laser Fusion at the University of Rochester’s Laboratory for Laser Energetics,” presented at Science Exploration Day, Rochester, NY, 17 May 2019.

M. S. Wei, “National Laser Users’ Facility and Basic Science Programs at the Omega Laser Facility,” presented at Workshop on Opportunities, Challenges, and Best Practices for Basic Plasma Science User Facilities, College Park, MD, 20–21 May 2019.

The following presentations were made at CEA–NNSA Joint Diagnostic Meeting, Washington, DC, 21–22 May 2019:

R. Boni, “Update on Streak Tube Simulations.”

S. T. Ivancic, W. Theobald, C. Sorce, M. Bedzyck, F. J. Marshall, C. Stoeckl, R. C. Shah, M. Lawrie, S. P. Regan, T. C. Sangster, E. M. Campbell, T. J. Hilsabeck, K. Englehorn, J. D. Kilkenny, T. M. Chung, J. D. Hares, A. K. L. Dymoke-Bradshaw, P. Bell, J. Celeste, A. C. Carpenter, M. Dayton, D. K. Bradley, M. C. Jackson, E. Hurd, L. Pickworth, S. R. Nagel, G. Rochau, J. Porter, M. Sanchez, L. Claus, G. Robertson, and Q. Looker, “The Single Line-of-Sight Time-Resolved X-Ray Imager on OMEGA.”

S. P. Regan, “Neutron Imaging Systems on OMEGA.”

The following presentations were made at the Laser Imprint Workshop, Rochester, NY, 22–24 May 2019:

T. J. B. Collins, C. Stoeckl, R. Epstein, S. Miller, O. M. Mannion, R. Betti, J. A. Delettrez, W. A. Bittle, C. J. Forrest, V. Yu. Glebov, V. N. Goncharov, D. R. Harding, I. V. Igumenshev, D. W. Jacobs-Perkins, R. J. Janezic, J. H. Kelly,

T. Z. Kosc, C. Milehamn, D. T. Michel, R. L. McCrory, P. W. McKenty, F. J. Marshall, S. F. B. Morse, P. B. Radha, S. P. Regan, B. Rice, T. C. Sangster, M. J. Shoup III, W. T. Shmayda, C. Sorce, W. Theobald, J. Ulreich, M. D. Wittman, J. A. Frenje, M. Gatu Johnson, and R. D. Petrasso, “Mixing at the Fuel–Ablator Interface in Backlit OMEGA Cryogenic Implosions.”

C. Dorrer, “The FLUX Project.”

S. X. Hu, J. L. Peebles, W. Theobald, S. P. Regan, P. B. Radha, A. Shvydky, V. N. Goncharov, M. Karasik, J. Oh, A. Velikovich, S. Obenschain, A. Casner, G. Duchateau, B. Chimier, H. Huang, M. Farrell, A. Nikroo, M. Hohenberger, V. A. Smalyuk, M. J. Bonino, D. R. Harding, T. R. Boehly, D. T. Michel, T. J. Kessler, J. P. Knauer, R. Epstein, I. V. Igumenshchev, M. J. Rosenberg, V. T. Tikhonchuk, A. Kar, C. Cao, C. Stoeckl, T. J. B. Collins, J. A. Marozas, K. S. Anderson, T. C. Sangster, R. Betti, D. H. Froula, J. P. Palastro, D. Turnbull, F. J. Marshall, M. Wei, T. Mehlhorn, and E. M. Campbell, “Review of Imprint Effects on Direct-Drive Inertial Confinement Fusion.”

J. P. Knauer, “The Effect of Imprint on OMEGA Cryogenic Target Implosions.”

J. L. Peebles, “OHRV Measurements in Direct-Drive Experiments.”

A. Shvydky, P. B. Radha, M. J. Rosenberg, K. S. Anderson, V. N. Goncharov, J. A. Marozas, F. J. Marshall, P. W. McKenty, S. P. Regan, T. C. Sangster, M. Hohenberger, J. M. Di Nicola, J. M. Koning, M. M. Marinak, L. Masse, and M. Karasik, “Hydrodynamic Instability Growth and Imprint Experiments at the National Ignition Facility.”

G. Chen, R. Adam, D. E. Burgler, I. Komissarov, S. Heidtfeld, H. Hardtdegen, M. Mikulics, C. M. Schneider, and R. Sobolewski, “Ultrabroadband THz Radiation Transients Emitted from Ta/NiFe/Pt Nanolayers upon Excitation by Femtosecond Laser Pulses,” presented at Frontiers in Materials Science for the 21st Century Symposium, Rochester, NY, 23 May 2019.

C. Thomas, “Laser-Direct-Drive Status and Future Plans,” presented at the 28th IEEE Symposium on Fusion Engineering, Ponte Vedra Beach, FL, 2–6 June 2019.

The following presentations were made at Optical Interference Coatings, Santa Ana Pueblo, NM, 2–7 June 2019:

S. MacNally, C. Smith, J. Spaulding, J. Foster, and J. B. Oliver, “Glancing-Angle-Deposited Silica Films for Ultraviolet Wave Plates.”

J. B. Oliver, “Precision Coatings for Large Optics.”

J. B. Oliver, A. L. Rigatti, T. Noll, J. Spaulding, J. Hettrick, V. Gruschow, G. Mitchell, D. Sadowski, C. Smith, and B. Charles, “Large-Aperture Coatings for Fusion-Class Laser Systems.”

J. B. Oliver, J. Spaulding, and B. Charles, “Stress Compensation by Deposition of a Nonuniform Corrective Coating.”

C. Smith, S. MacNally, and J. B. Oliver, “Ellipsometric Modeling of Serially Bi-Deposited Glancing-Angle-Deposition Coatings.”

The following presentations were made at the 49th Anomalous Absorption Conference, Telluride, CO, 9–14 June 2019:

D. H. Edgell, R. Bahr, J. Katz, and D. H. Froula, “Anomalous Asymmetry of Unabsorbed Light in OMEGA Implosions.”

R. K. Follett, J. G. Shaw, D. H. Edgell, D. H. Froula, C. Dorrer, J. Bromage, E. M. Hill, T. J. Kessler, A. V. Maximov, A. A. Solodov, E. M. Campbell, J. P. Palastro, J. F. Myatt, J. W. Bates, and J. L. Weaver, “Mitigation of Laser–Plasma Instabilities Using Bandwidth,” (invited).

P. Franke, D. Turnbull, J. P. Palastro, J. Katz, I. A. Begishev, R. Boni, J. Bromage, J. L. Shaw, A. Howard, A. L. Milder, A. Davies, S. Bucht, D. Haberberger, A. M. Hansen, and D. H. Froula, “Measurement and Control of Ionization Waves of Arbitrary Velocity” (invited).

A. M. Hansen, D. Turnbull, J. Katz, A. L. Milder, J. P. Palastro, D. Mastrosimone, and D. H. Froula, “Phase Plates in Thomson-Scattering Experiments.”

A. Howard, D. Turnbull, A. S. Davies, P. Franke, D. H. Froula, and J. P. Palastro, “Photon Acceleration in a Flying Focus.”

A. Kar, S. X. Hu, P. B. Radha, and G. Duchateau, “A Micro-physics Model to Understand the Solid-to-Plasma Transition of Dielectric Ablator Materials for Direct-Drive Implosions.”

A. V. Maximov, J. G. Shaw, and J. P. Palastro, “Modeling Stimulated Raman Scattering and Cross-Beam Energy Transfer in Direct-Drive National Ignition Facility Plasmas.”

A. L. Milder, R. Boni, J. Katz, P. Franke, S. T. Ivancic, J. L. Shaw, J. P. Palastro, A. Davies, A. M. Hansen, D. Turnbull, I. A. Begishev, D. H. Froula, M. Sherlock, H. Le, and W. Rozmus, “Measuring Electron Distribution Functions Driven by Inverse Bremsstrahlung Heating with Collective Thomson Scattering” (invited).

J. P. Palastro, T. M. Antonsen Jr., L. Nguyen, A. Howard, D. W. Ramsey, T. T. Simpson, R. K. Follett, D. Turnbull, J. Vieira, and D. H. Froula, “Cherenkov Radiation from a Plasma.”

H. G. Rinderknecht, H. S. Park, J. S. Ross, P. A. Amendt, D. P. Higginson, S. C. Wilks, R. K. Follett, D. Haberberger, J. Katz, D. H. Froula, N. M. Hoffman, G. Kagan, B. Keenan, A. Simakov, L. Chacon, and E. Vold, “Ion-Velocity Structure in Strong Collisional Plasma Shocks” (invited).

M. J. Rosenberg, A. A. Solodov, W. Seka, R. K. Follett, S. P. Regan, C. Ren, R. Epstein, A. R. Christopherson, R. Betti, A. V. Maximov, T. J. B. Collins, V. N. Goncharov, R. W. Short, D. H. Froula, P. B. Radha, J. F. Myatt, P. Michel, M. Hohenberger, L. Masse, G. Swadling, J. S. Ross, T. Chapman, J. D. Moody, J. W. Bates, and A. J. Schmitt, “Planar Laser-Plasma Interaction Experiments at Direct-Drive Ignition-Relevant Scale Lengths at the National Ignition Facility.”

A. Ruocco, A. V. Maximov, J. P. Palastro, R. K. Follett, W. Theobald, A. Casner, D. Batani, J. Trela, A. Colaïtis, G. Duchateau, and V. T. Tikhonchuk, “Modeling of Laser-Plasma Interaction in the Shock-Ignition Regime with *LPSE*: Comparison with Particle-in-Cell Simulations and Experiments.”

A. A. Solodov, M. J. Rosenberg, A. R. Christopherson, R. Betti, M. Stoeckl, W. Seka, R. Epstein, R. K. Follett, P. B. Radha, S. P. Regan, D. H. Froula, V. N. Goncharov, J. F. Myatt, M. Hohenberger, B. Bachmann, and P. Michel, “Hot-Electron Preheat and Energy Deposition in Direct-Drive Implosion Experiments at the National Ignition Facility.”

D. Turnbull, C. Dorrer, D. Edgell, R. K. Follett, D. H. Froula, A. M. Hansen, J. Katz, B. Kruschwitz, A. L. Milder, J. P. Palastro, A. Colaïtis, T. Chapman, L. Divol, C. Goyon, G. E. Kemp, D. Mariscal, P. Michel, J. D. Moody, B. B. Pollock, J. S. Ross, D. J. Strozzi, E. R. Tubman, and N. C. Woolsey, “Crossed-Beam Energy Transfer Model Validation

for Increased Confidence in Proposed Laser Upgrades and Implosion Scaling.”

C. J. Forrest, V. Yu. Glebov, J. P. Knauer, P. B. Radha, J. R. Rygg, U. Schroeder, O. M. Mannion, Z. L. Mohamed, S. P. Regan, T. C. Sangster, A. Schwemmlin, C. Stoeckl, J. A. Frenje, M. Gatu Johnson, F. H. Seguin, R. D. Petrasso, D. T. Casey, C. Cerjan, D. Dearborn, M. J. Edwards, R. Hatarik, O. S. Jones, O. L. Landen, A. J. Mackinnon, S. Quaglioni, S. Sepke, P. Springer, I. Thomson, R. E. Tipton, A. B. Zylstra, G. Grim, C. Brune, A. Voinov, J. D. Kilkenny, B. Appelbe, A. Crilly, G. Hale, H. W. Herrmann, Y. H. Kim, M. Paris, W. Martin, and B. Augierre, “Nuclear Science at the University of Rochester’s Omega Laser Facility,” presented at Texas A & M University, College Station, TX, 13 June 2019.

The following presentations were made at the 21st Biennial Conference of the APS Topical Group on Shock Compression of Condensed Matter, Portland OR, 16–21 June 2019:

D. A. Chin, P. M. Nilson, J. J. Ruby, X. Gong, D. N. Polsin, T. R. Boehly, D. Mastro Simone, D. Guy, J. R. Rygg, G. W. Collins, I. Szumila, J. Buettner, D. Trail, M. Harmand, Y. Ping, F. Coppari, U. Feldman, and J. Seely, “An Extended X-Ray Absorption Fine Structure Spectroscopy Study of Iron Oxides.”

L. Crandall, G. Tabak, Z. K. Sprowal, D. N. Polsin, J. R. Rygg, G. W. Collins, D. E. Fratanduono, R. F. Smith, and J. H. Eggert, “Dynamic Precompression: Secondary Hugoniot of MgO.”

M. Ghosh and S. X. Hu, “Diamond Formation From Hydrocarbons in Planetary Conditions: An *ab initio* Study.”

M. K. Ginnane, D. N. Polsin, X. Gong, T. R. Boehly, J. R. Rygg, G. W. Collins, A. Lazicki, R. Kraus, J. H. Eggert, M. Marshall, D. E. Fratanduono, J. P. Davis, C. A. McCoy, and C. Seagle, “X-Ray Diffraction of Shock-Ramped and Shock-Released Platinum.”

X. Gong, D. N. Polsin, R. Paul, R. Saha, J. R. Rygg, and G. W. Collins, “Structure and Optical Properties of Ramp Compressed Silicon Up to 550 GPa.”

B. J. Henderson, T. R. Boehly, M. Zaghoo, J. R. Rygg, D. N. Polsin, X. Gong, L. Crandall, M. F. Huff, M. K. Ginnane,

G. W. Collins, S. Ali, P. M. Celliers, R. Briggs, M. Gorman, M. Marshall, and J. H. Eggert, "A Broadband Reflectance Diagnostic for Matter at Extreme Conditions."

M. Huff, J. R. Rygg, G. W. Collins, T. R. Boehly, M. Zaghoo, D. N. Polsin, B. J. Henderson, L. Crandall, D. E. Fratanduono, M. Millot, R. F. Smith, J. H. Eggert, P. M. Celliers, M. C. Gregor, and C. A. McCoy, "Sound Velocity in Shocked Iron and Beryllium to ~1500 GPa."

D. N. Polsin, X. Gong, M. F. Huff, L. E. Crandall, G. W. Collins, T. R. Boehly, J. R. Rygg, A. Lazicki, M. Millot, P. M. Celliers, J. H. Eggert, and M. I. McMahon, "High-Pressure Structural and Electronic Properties of Ramp-Compressed Sodium."

J. J. Ruby, J. R. Rygg, C. J. Forrest, V. Yu. Glebov, D. A. Chin, G. W. Collins, B. Bachmann, J. A. Gaffney, Y. Ping, H. Sio, and N. V. Kabadi, "Measurement of Spherically Converging Shock Waves on OMEGA."

J. R. Rygg, A. B. Zylstra, P. Grabowski, M. Millot, M. Gatu Johnson, B. Lahmann, R. D. Petrasso, F. H. Seguin, H. Sio, Y. H. Ding, and S. X. Hu, "Precision Measurements of Stopping Power in Shock-Compressed Carbon."

R. Saha, J. Topp-Muggleston, G. Gregori, T. R. Boehly, G. W. Collins, S. P. Regan, T. G. White, and J. R. Rygg, "Atomic and Electronic Structure of Warm Dense Silicon."

Z. K. Sprowal, D. N. Polsin, T. R. Boehly, D. G. Hicks, J. R. Rygg, G. W. Collins, and M. F. Huff, "Double Shock in Polystyrene."

G. Tabak, M. A. Millot, S. Hamel, T. Ogawa, P. M. Celliers, D. E. Fratanduono, A. Lazicki, D. C. Swift, S. Brygoo, P. Loubeyre, T. R. Boehly, L. Crandall, B. J. Henderson, M. Zaghoo, S. Ali, R. Kodama, K. Miyanishi, N. Ozaki, T. Sano, R. Jeanloz, D. G. Hicks, G. W. Collins, J. H. Eggert, and J. R. Rygg, "Equation of State and Metallization of Methane Shock-Compressed to 400 GPa."

The following presentations were made at the 12th International Laser Operations Workshop 2019, Aldermaston, UK, 17–20 June 2019:

K. A. Bauer, M. Heimbueger, S. Sampat, L. J. Waxer, E. C. Cost, J. H. Kelly, V. Kobilansky, J. Kwiatkowski, S. F. B. Morse, D. Nelson, D. Weiner, G. Weselak, and J. Zou, "On-Shot, In-Tank Measurements of the OMEGA Laser System Focal Spot."

D. Canning, "Formalized Incident Investigation, Reporting, and Recurrence Mitigation."

S. Householder, G. Brent, J. Coon, M. Labuzeta, M. Barczys, J. H. Kelly, B. Kruschwitz, T. Smith, and S. F. B. Morse, "Improvements to Omega Disk Amplifier Performance Through Analysis of High-Resolution Flash-Lamp Waveforms."

J. Kwiatkowski, S. Sampat, K. A. Bauer, B. Ehrich, V. Guiliano, J. H. Kelly, T. Z. Kosci, R. G. Peck, and L. J. Waxer, "Characterization of Mid-Chain Transmission and Losses on OMEGA."

M. Labuzetta, J. Armstrong, M. Bonino, D. Canning, A. Consentino, S. Householder, M. Krieger, G. Pien, and C. Sorce, "Qualification Process for Experimental Users at the Omega Laser Facility."

L. J. Waxer, "Omega Facility Overview."

---

B. Rice, J. Ulreich, and M. J. Shoup III, "Prediction of Deuterium–Tritium Ice Layer Uniformity in Direct-Drive Confinement Fusion Target Capsules," presented NAFEMS World Congress 2019, Quebec City, Canada, 17–20 June 2019.

---

S.-W. Bahk, "Phase Retrieval Using Gaussian Basis Functions," presented at Computational Optical Sensing and Imaging, Munich, Germany, 24–27 June 2019.



